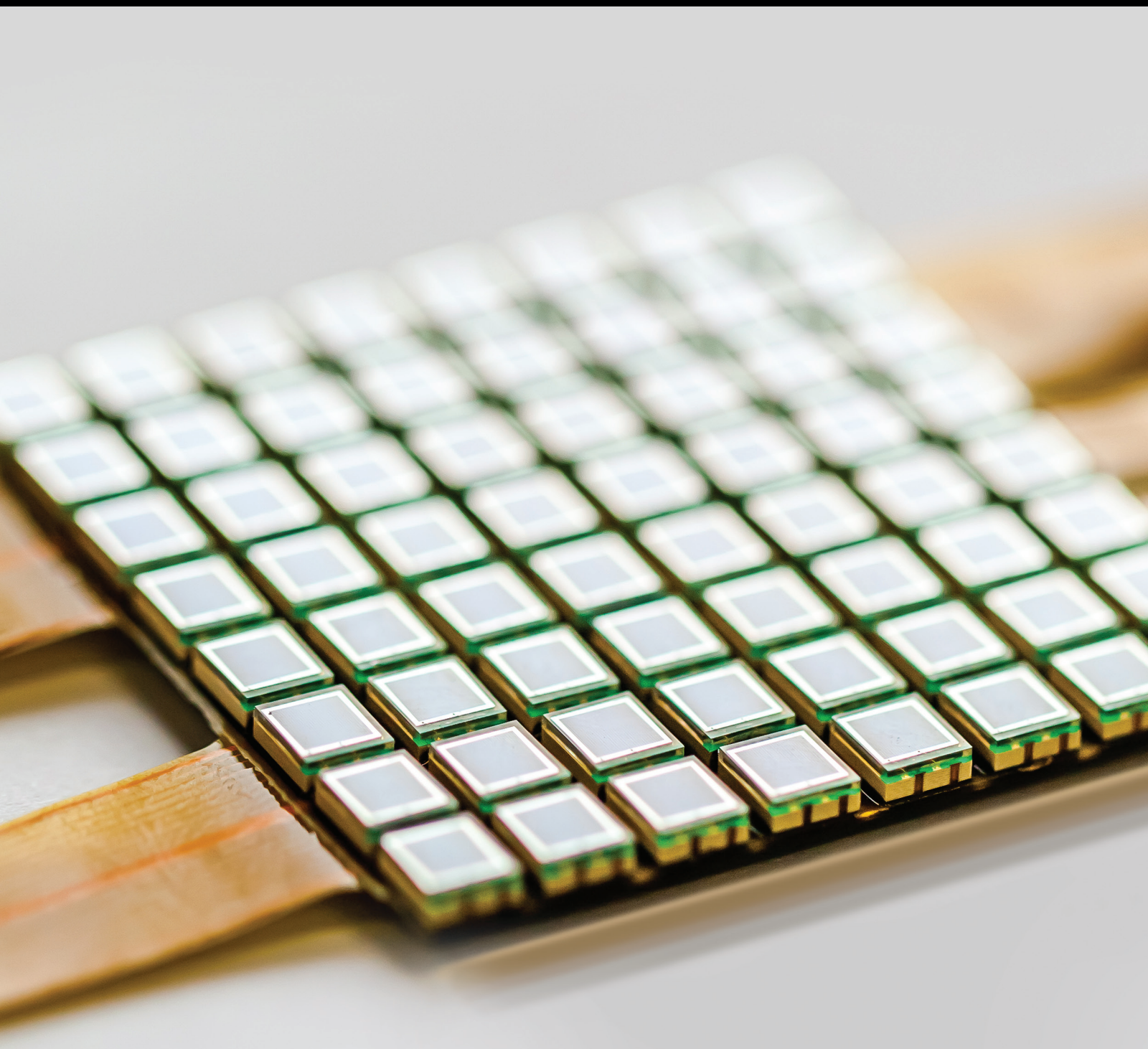


Applications of Polarimetric SAR

Guest Editors: Jian Yang, Yoshio Yamaguchi, Jong-Sen Lee, Ridha Touzi, and Wolfgang-Martin Boerner





Applications of Polarimetric SAR

Applications of Polarimetric SAR

Guest Editors: Jian Yang, Yoshio Yamaguchi, Jong-Sen Lee,
Ridha Touzi, and Wolfgang-Martin Boerner



Copyright © 2015 Hindawi Publishing Corporation. All rights reserved.

This is a special issue published in "Journal of Sensors." All articles are open access articles distributed under the Creative Commons Attribution License, which permits unrestricted use, distribution, and reproduction in any medium, provided the original work is properly cited.

Editorial Board

Harith Ahmad, Malaysia
Sheikh Akbar, USA
Francisco J. Arregui, Spain
Francesco Baldini, Italy
Romeo Bernini, Italy
Shekhar Bhansali, USA
Wojtek J. Bock, Canada
Hubert Brändle, Switzerland
Stefania Campopiano, Italy
Jian-Nong Cao, Hong Kong
Chi Chiu Chan, Singapore
Nick Chaniotakis, Greece
Nicola Cioffi, Italy
Elisabetta Comini, Italy
Marco Consales, Italy
Jesus Corres, Spain
Andrea Cusano, Italy
Dzung V. Dao, Japan
Manel del Valle, Spain
Ignacio Del Villar, Spain
Utkan Demirci, USA
Junhang Dong, USA
Omar Elmazria, France
Abdelhamid Errachid, France
Stephane Evoy, Canada
Xiao-Miao Feng, China
Vittorio Ferrari, Italy
Luca Francioso, Italy
Laurent Francis, Belgium
Paddy French, Netherlands
Lung-Ming Fu, Taiwan
Mohammad Reza Ganjali, Iran
Wei Gao, Japan
Michele Giordano, Italy
K. Vengatajalabathy Gobi, India
Marco Grassi, Italy
Banshi D. Gupta, India
M. del Carmen Horrillo, Spain
Wieslaw Jakubik, Poland
Hai-Feng Ji, USA
K. Kalantar-Zadeh, Australia
Sher Bahadar Khan, Saudi Arabia
Sang Sub Kim, Republic of Korea
Won-Gun Koh, Republic of Korea
Challa Kumar, USA
Hiroki Kuwano, Japan
Laura M. Lechuga, Spain
Jong-Jae Lee, Republic of Korea
Chengkuo Lee, Singapore
Chenzhong Li, USA
Eduard Llobet, Spain
Yu-Lung Lo, Taiwan
Oleg Lupan, Moldova
Eugenio Martinelli, Italy
Yasuko Y. Maruo, Japan
Ignacio R. Matias, Spain
Mike McShane, USA
Igor L. Medintz, USA
Fanli Meng, China
Aldo Minardo, Italy
Joan Ramon Morante, Spain
Lucia Mosiello, Italy
Masayuki Nakamura, Japan
Liviu Nicu, France
Marimuthu Palaniswami, Australia
Gyuhae Park, Republic of Korea
Alain Pauly, France
Michele Penza, Italy
Andrea Ponzoni, Italy
Biswajeet Pradhan, Malaysia
Zhi-Mei Qi, China
Ioannis Raptis, Greece
Leonhard Reindl, Germany
Christos Riziotis, Greece
M. L. Rodríguez-Méndez, Spain
Albert Romano-Rodríguez, Spain
Josep Samitier, Spain
Giorgio Sberveglieri, Italy
Luca Schenato, Italy
Michael J. Schöning, Germany
Andreas Schütze, Germany
Woosuck Shin, Japan
Pietro Siciliano, Italy
Weilian Su, USA
Tong Sun, UK
Hidekuni Takao, Japan
Isao Takayanagi, Japan
Pierre Temple-Boyer, France
Guiyun Tian, UK
Suna Timur, Turkey
Jianhua Tong, China
Yu Chen Tsai, Taiwan
Hana Vaisocherova, Czech Republic
Joel Villatoro, Iran
Dong-ning Wang, Hong Kong
Qihao Weng, USA
Stanley E. Woodard, USA
Hai Xiao, USA
Jerliang Andrew Yeh, Taiwan
Hyeonseok Yoon, Republic of Korea
Wentao Zhang, China
Tao Zhu, China

Contents

Applications of Polarimetric SAR, Jian Yang, Yoshio Yamaguchi, Jong-Sen Lee, Ridha Touzi, and Wolfgang-Martin Boerner
Volume 2015, Article ID 316391, 2 pages

Superresolution Polarimetric ISAR Imaging Based on 2D CP-GTD Model, Da-hai Dai, Jing-ke Zhang, Xue-song Wang, and Shun-ping Xiao
Volume 2015, Article ID 293141, 11 pages

Impact of Topography and Tidal Height on ALOS PALSAR Polarimetric Measurements to Estimate Aboveground Biomass of Mangrove Forest in Indonesia, S. Darmawan, W. Takeuchi, Y. Vetrta, K. Wikantika, and D. K. Sari
Volume 2015, Article ID 641798, 13 pages

Detecting the Depth of a Subsurface Brine Layer in Lop Nur Lake Basin Using Polarimetric L-Band SAR, Chang-An Liu, Huaze Gong, Yun Shao, and Bingyan Li
Volume 2015, Article ID 245790, 11 pages

Comparisons of Circular Transmit and Linear Receive Compact Polarimetric SAR Features for Oil Slicks Discrimination, Yu Li, Hui Lin, Yuanzhi Zhang, and Jie Chen
Volume 2015, Article ID 631561, 14 pages

Model-Based Pseudo-Quad-Pol Reconstruction from Compact Polarimetry and Its Application to Oil-Spill Observation, Junjun Yin, Wooil Moon, and Jian Yang
Volume 2015, Article ID 734848, 8 pages

Monitoring of Damage in Sunflower and Maize Parcels Using Radar and Optical Time Series Data, György Surek and Gizella Nádor
Volume 2015, Article ID 548506, 25 pages

Editorial

Applications of Polarimetric SAR

**Jian Yang,¹ Yoshio Yamaguchi,² Jong-Sen Lee,³
Ridha Touzi,⁴ and Wolfgang-Martin Boerner⁵**

¹*Department of Electronic Engineering, Tsinghua University, Beijing 100084, China*

²*Department of Information Engineering, Niigata University, Niigata 950-2181, Japan*

³*Computational Physics Inc., Springfield, VA 22151-2110, USA*

⁴*Canada Centre for Remote Sensing, Natural Resources Canada, 588 Booth Street, Ottawa, ON, Canada K1A 0Y7*

⁵*UIC-ECE Communications, Sensing & Navigation Laboratory, University of Illinois at Chicago, 900 W. Taylor Street, SEL (607) W-4210, M/C 154, Chicago, IL 60607, USA*

Correspondence should be addressed to Jian Yang; yangjian_ee@tsinghua.edu.cn

Received 21 May 2015; Accepted 27 May 2015

Copyright © 2015 Jian Yang et al. This is an open access article distributed under the Creative Commons Attribution License, which permits unrestricted use, distribution, and reproduction in any medium, provided the original work is properly cited.

Polarimetric SAR is an advanced imaging radar system; it plays an important role in radar remote sensing. With a polarimetric SAR, we can obtain much more information than conventional SAR systems (i.e., single polarized SAR systems) [1]. Up to now, various airborne and spaceborne polarimetric SAR systems have been developed, such as AirSAR, PI-SAR-1/2, E/F-SAR, CV-580 SAR, SIR-C/X-SAR, ALOS-PALSAR1/2, Radarsat-2, TerraSAR-X, and TanDEM-X. They have measured a huge mass of fully polarimetric data. Now polarimetric SAR has many applications in many fields, including agriculture (crop classification, soil moisture extraction, and crop assessment), oceanography (surface currents and wind field retrieval), forestry (forest monitoring, classification, and tree height estimation), disaster monitoring (oil spill detection, disaster assessment), and military (ship detection, target recognition/classification).

After calibration of the polarimetric SAR and image speckle filtering, feature extraction is the key step for target detection and target classification. Some important features were introduced, such as the polarization ratio and the polarization entropy [2]. An important approach to feature extraction is target decomposition. It is to decompose a scattering matrix or a covariance matrix to the linear combinations of some special typical scattering, such as the single bounce scattering, the double bounce scattering, and the volume scattering. The important decomposition includes

Krogager's decomposition [3], Cloude-Pottier's decomposition [2], Freeman-Durden's decomposition [4], Yamaguchi's decomposition [5], Touzi's decomposition [6], and Cameron-Rais decomposition [7]. However, it is impossible to find a matrix to describe various volume scattering. So we still need to improve the volume scattering model in this approach. Another attempt to extract features is to use similarity between two matrices [8]. This method is independent of target decomposition and it can also be used to extract the features on the single bounce scattering, the double bounce scattering, and so on.

With target features, we can classify different kinds of targets/land covers. A lot of investigations have been made, for example, the complex Wishart distribution based method [9], target decomposition based methods [2–7], multifrequency SAR data fusion based methods, and quantitative comparison of classification capability of fully polarimetric versus dual- and single-polarization SAR [10].

Damage monitoring is an important topic in remote sensing [11]. In this special issue, a paper is to investigate the temporal behavior of geometrical structural change of cropland affected by four different types of damages. The authors used a lot of polarimetric SAR data and optical time series data and made a lot of investigations.

Parameter estimation is another important topic in polarimetric SAR applications. Up to now, many investigations

have been made in soil moisture extraction and tree height estimation. Cloude and Papathanassiou [12] made significant contribution to applications of polarimetric-interferometric SAR, especially to estimation of tree height. In this special issue, a paper is to investigate the impact of topography and tidal height by ALOS-1 measurements on HH and HV for estimating above ground biomass of mangrove forest in Indonesia. Another paper is to retrieve the depth of subsurface brine layer in Lop Nur by copolarized phase difference of surface scattering. From both papers, readers will find the potential ability of polarimetric SAR in quantitative remote sensing.

Compact polarimetric SAR is a special dual polarized SAR system. Comparing a polarimetric SAR system, compact polarimetric SAR has some advantages in pulse repeat frequency and width of surveying although it has some disadvantages. In this special issue, two papers are on the applications of compact polarimetric SAR. Readers will find that compact polarimetric SAR can be used for oil spill detection and classification.

“We are very fortunate to be at the doorstep of the golden age for developing polarimetric SAR applications.” We will find more applications in the near future.

Jian Yang
Yoshio Yamaguchi
Jong-Sen Lee
Ridha Touzi
Wolfgang-Martin Boerner

References

- [1] W.-M. Boerner, “Recent advances in extra-wide-band polarimetry, interferometry and polarimetric interferometry in synthetic aperture remote sensing and its applications,” *IEE Proceedings: Radar, Sonar and Navigation*, vol. 150, no. 3, pp. 113–124, 2003.
- [2] S. R. Cloude and E. Pettier, “A review of target decomposition theorems in radar polarimetry,” *IEEE Transactions on Geoscience and Remote Sensing*, vol. 34, no. 2, pp. 498–518, 1996.
- [3] E. Krogager, “New decomposition of the radar target scattering matrix,” *Electronics Letters*, vol. 26, no. 18, pp. 1525–1527, 1990.
- [4] A. Freeman and S. L. Durden, “A three-component scattering model for polarimetric SAR data,” *IEEE Transactions on Geoscience and Remote Sensing*, vol. 36, no. 3, pp. 963–973, 1998.
- [5] Y. Yamaguchi, T. Moriyama, M. Ishido, and H. Yamada, “Four-component scattering model for polarimetric SAR image decomposition,” *IEEE Transactions on Geoscience and Remote Sensing*, vol. 43, no. 8, pp. 1699–1706, 2005.
- [6] R. Touzi, “Target scattering decomposition in terms of roll-invariant target parameters,” *IEEE Transactions on Geoscience and Remote Sensing*, vol. 45, no. 1, pp. 73–84, 2007.
- [7] W. L. Cameron and H. Rais, “Conservative polarimetric scatterers and their role in incorrect extensions of the Cameron decomposition,” *IEEE Transactions on Geoscience and Remote Sensing*, vol. 44, no. 12, pp. 3506–3516, 2006.
- [8] J. Yang, Y.-N. Peng, and S.-M. Lin, “Similarity between two scattering matrices,” *Electronics Letters*, vol. 37, no. 3, pp. 193–194, 2001.
- [9] J.-S. Lee, M. R. Grunes, and R. Kwok, “Classification of multi-look polarimetric SAR imagery based on complex Wishart distribution,” *International Journal of Remote Sensing*, vol. 15, no. 11, pp. 2299–2311, 1994.
- [10] J.-S. Lee and E. Pottier, *Polarimetric Radar Imaging: From Basics to Applications*, CRC Press, Boca Raton, Fla, USA, 2009.
- [11] A. Gaber, F. Soliman, M. Koch, and F. El-Baz, “Using full-polarimetric SAR data to characterize the surface sediments in desert areas: a case study in El-Gallaba Plain, Egypt,” *Remote Sensing of Environment*, vol. 162, pp. 11–28, 2015.
- [12] S. R. Cloude and K. P. Papathanassiou, “Polarimetric SAR interferometry,” *IEEE Transactions on Geoscience and Remote Sensing*, vol. 36, no. 5, pp. 1551–1565, 1998.

Research Article

Superresolution Polarimetric ISAR Imaging Based on 2D CP-GTD Model

Da-hai Dai, Jing-ke Zhang, Xue-song Wang, and Shun-ping Xiao

College of Electronic Science and Engineering, National University of Defense Technology, Changsha, Hunan 410073, China

Correspondence should be addressed to Da-hai Dai; ddh1206@163.com

Received 24 December 2014; Accepted 20 April 2015

Academic Editor: Jong-Sen Lee

Copyright © 2015 Da-hai Dai et al. This is an open access article distributed under the Creative Commons Attribution License, which permits unrestricted use, distribution, and reproduction in any medium, provided the original work is properly cited.

This paper presented a new approach to superresolution ISAR imaging based on a scattering model called coherent polarized geometrical theory of diffraction (CP-GTD) which is better matched to the physical scattering mechanism. The algorithm is a joint processing between polarization and superresolution essentially. It can also estimate the number, position, frequency dependence, span, and normalized scattering matrix of scattering centers instantaneously for each channel rather than the one which extracts parameters from each channel separately, and its performance is better than the latter because the fully polarized information is used. The superiority of the CP-GTD is verified by experiment results based on simulated and real data.

1. Introduction

Since the 1990s there has been a boost in radar target recognition (RTR) based on fully polarized information. Specifically, RTR based on fully polarized high-resolution radars has been taken as a very promising approach [1, 2]. That is because that the association of high resolution and full polarization can afford more information about targets' structure [3–6]. Backscattering from manmade objects is strongly dependent on polarization, so using only a single channel some important scatterers might be totally missed. The appropriate joint processing of the polarization channels provides higher SNR level which is required to achieve high superresolution gains and makes the superresolution algorithm more robust. Furthermore, the scattering matrix will present very useful information for RTR [7–11].

In the high-frequency region, the electric field backscattered from a complex radar target can be modeled approximately by a sum of fields scattered from some dominant scattering centers on the target. How to realize superresolution is always a key problem for ISAR [12]. There are two main approaches: one is the conventional FFT-based processing; the other is model-based processing. The common scattering

center models include point-scattering model, damped exponential (DE) [5] model, and the model based on geometry theory of diffraction (GTD) [6]. The GTD model can accurately match the high-frequency electromagnetic scattering mechanism and approximates the physical mechanism of high-frequency electromagnetic scattering more closely. The existing GTD-based scattering model is already mature for singly polarized modeling. Although it was mentioned that polarization effects can be included for 1D scattering center extraction in [6], it had not explained how to do it in detail and it cannot fit for full-polarization ISAR.

The remainder of the paper is organized as follows. In Section 2, for full-polarization ISAR system, a new model, called 2D coherent polarization GTD (CP-GTD) model, which is capable of accurately describing the high-frequency polarization scattering mechanism of the radar target, is presented. In Section 3, a novel method based on CP-GTD model for full-polarization scattering center extraction and parameter estimation is proposed in detail. In Section 4, the validity is proved by the experimental results based on simulated and real data. Some conclusions are given in Section 5.

2. 2D CP-GTD Signal Model for Fully Polarized ISAR

A fully polarized radar measures the backscattered electric field with two linearly independent transmit and receive polarizations also called dual-channel orthogonal polarization measurements. Without regard to the translational motion, the raw data of ISAR can be represented by a 2D signal of frequency-angular domain. Suppose horizontal and vertical linear polarization (H, V) as the two linearly independent transmit and receive polarizations. We adopt a full-polarization parametric scattering model based on geometrical theory of diffraction (GTD) which is called 2D coherent polarization GTD (CP-GTD) model in this paper.

Taking the coherent stepped-frequency full-polarization radar as an example, fully polarized ISAR can measure a set of scattering matrices $\{S(f_n)\}$ at a set of stepped frequencies at an angular domain. The backscattered signals from d scattering centers are then given by

$$\mathbf{E}_{sc} = \sum_{i=1}^d \exp(-j2kr_i) \left(j \frac{k}{k_c}\right)^{\alpha_i} \mathbf{S}_i \mathbf{E}_{in}. \quad (1)$$

That is,

$$\begin{bmatrix} E_H^{sc}(f, \theta) \\ E_V^{sc}(f, \theta) \end{bmatrix} = \sum_{i=1}^d \left(j \frac{k}{k_c}\right)^{\alpha_i} \exp(-j2kr_i) \cdot \begin{bmatrix} S_{HH}^i(f, \theta) & S_{HV}^i(f, \theta) \\ S_{VH}^i(f, \theta) & S_{VV}^i(f, \theta) \end{bmatrix} \begin{bmatrix} E_H^{in}(f, \theta) \\ E_V^{in}(f, \theta) \end{bmatrix}, \quad (2)$$

where $\mathbf{E}_{in} = \begin{bmatrix} E_H^{in}(f, \theta) \\ E_V^{in}(f, \theta) \end{bmatrix}$ is the incident signal; $\mathbf{E}_{sc} = \begin{bmatrix} E_H^{sc}(f, \theta) \\ E_V^{sc}(f, \theta) \end{bmatrix}$ is the backscattered signal; $\mathbf{S}_i(f, \theta) = \begin{bmatrix} S_{HH}^i(f, \theta) & S_{HV}^i(f, \theta) \\ S_{VH}^i(f, \theta) & S_{VV}^i(f, \theta) \end{bmatrix}$ is the scattering matrix of the i th scattering center of the radar target; $k = 2\pi/\lambda$ is the wavenumber; λ is the wavelength; f is the frequency; θ is the aspect angle. α is a frequency dependence factor of the scattering center which characterizes the geometry and hence is named type factor as well. According to the geometrical theory of diffraction, the type factor is an integer multiple of $1/2$. For canonical scattering geometries, the type parameters are as follows: $\alpha = 1$ is for flat plate at broadside or dihedral; $\alpha = 1/2$ is for singly curved surface reflection; $\alpha = 0$ is for point scatterer or doubly curved surface reflection or straight edge specular; $\alpha = -1/2$ is for edge diffraction; $\alpha = -1$ is for corner diffraction.

Thus, the raw data of every polarization channel can be represented as

$$x_{pq}(f, \theta) = \sum_{i=1}^d \left(j \frac{k}{k_c}\right)^{\alpha_i} S_{pq}^i(f, \theta) \cdot \exp(-j2k(x_i \cos \theta + y_i \sin \theta)) + u_{pq}(f, \theta), \quad (3)$$

where, $p, q = H$ or V , $u_{pq}(f, \theta)$ is the received noise.

Generally, the aspect angle is small; $S_{pq}^i(f, \theta)$ varies very little. Here suppose it is invariable in the imaging processing. Then,

$$x_{pq}(f, \theta) = \sum_{i=1}^d \left(j \frac{k}{k_c}\right)^{\alpha_i} S_{pq}^i \exp(-j2k(x_i \cos \theta + y_i \sin \theta)) + u_{pq}(f, \theta). \quad (4)$$

Taking Stolt interpolation the data in frequency-angular domain [6], let

$$\begin{aligned} k^x &= k \cos \theta, \\ k^y &= k \sin \theta. \end{aligned} \quad (5)$$

After the interpolation, (4) can be written in the Cartesian spectrum domain as

$$\begin{aligned} x_{pq}(k_m^x, k_n^y) &= \sum_{i=1}^d \left(j \frac{k}{k_c}\right)^{\alpha_i} S_{pq}^i \exp(-j2(k_m^x x_k + k_n^y y_k)) \\ &+ u_{pq}(k_m^x, k_n^y) \end{aligned} \quad (6)$$

$m = 1, 2, \dots, M; n = 1, 2, \dots, N.$

Rewrite (6) in the matrix form as

$$\mathbf{z} = \mathbf{A} \mathbf{s} + \mathbf{u}, \quad (7)$$

where \mathbf{z} is a $MN \times 4$ matrix corresponding to the full-polarization measurement information; \mathbf{s} is a $d \times 4$ matrix corresponding to the scattering matrix information of the scattering centers of radar target; \mathbf{A} is a $MN \times d$ matrix; \mathbf{u} is a $MN \times 4$ measurement noise matrix. Their concrete expressing forms are given as

$$\mathbf{z} = [\mathbf{x}_{HH} \quad \mathbf{x}_{HV} \quad \mathbf{x}_{VH} \quad \mathbf{x}_{VV}], \quad (8)$$

$$\mathbf{A} = [\mathbf{a}(\alpha_1, x_1, y_1) \quad \mathbf{a}(\alpha_2, x_2, y_2) \quad \cdots \quad \mathbf{a}(\alpha_d, x_d, y_d)], \quad (9)$$

$$\mathbf{s} = [\mathbf{s}_{HH} \quad \mathbf{s}_{HV} \quad \mathbf{s}_{VH} \quad \mathbf{s}_{VV}], \quad (10)$$

where \mathbf{x}_{pq} denotes the single-polarization measurement information; \mathbf{s}_{pq} and \mathbf{u}_{pq} denote the vectors of the single-polarization scattering information and the measurement noise, respectively; $\mathbf{a}(\alpha_i, x_i, y_i)$ is the steering vector corresponding to the i th scattering center. Their detailed expressions are

$$\mathbf{x}_{pq} = [x_{pq}(1, 1), x_{pq}(2, 1), \dots, x_{pq}(M, 1), x_{pq}(1, 2), \dots, x_{pq}(M, N)]^T,$$

$$\mathbf{a}(\alpha_i, x_i, y_i)$$

$$= \begin{bmatrix} \left(\frac{j\sqrt{(k_1^x)^2 + (k_1^y)^2}}{k_c} \right)^{\alpha_i} & 0 & \dots & 0 \\ 0 & \left(\frac{j\sqrt{(k_2^x)^2 + (k_2^y)^2}}{k_c} \right)^{\alpha_i} & \dots & 0 \\ \vdots & \vdots & \ddots & \vdots \\ 0 & 0 & \dots & \left(\frac{j\sqrt{(k_M^x)^2 + (k_N^y)^2}}{k_c} \right)^{\alpha_i} \end{bmatrix} \begin{bmatrix} \exp[j(k_1^x x_i + k_1^y y_i)] \\ \exp[j(k_2^x x_i + k_1^y y_i)] \\ \vdots \\ \exp[j(k_M^x x_i + k_N^y y_i)] \end{bmatrix} \quad (11)$$

$$\cong \Gamma(\alpha_i) \mathbf{b}(x_i, y_i),$$

$$\mathbf{s}_{pq} = [s_{1,pq} \ s_{2,pq} \ \dots \ s_{d,pq}]^T.$$

What is worthy to point out is that the CP-GTD model is not just a simple extension of the traditional GTD model. It is distinguished from the existing models by considering that each scattering center has an exclusive coherent polarization scattering matrix which can model full-polarization scattering as a whole. Its advantage will be verified in the following two sections.

3. Superresolution and Feature Extraction for Fully Polarized ISAR

In this section, the method of superresolution and feature extraction for fully polarized ISAR based on 2D CP-GTD model will be proposed using a modified 2D Multiple Signal Classification (MUSIC) algorithm [13].

In this modified MUSIC algorithm, using the raw data of full-polarization ISAR, a fully polarized correlation matrix can be obtained which is defined as $\mathbf{R}_{zz} = E(\mathbf{z}\mathbf{z}^H)$, where superscript “H” denotes conjugate transpose.

Make eigenvector-based decomposition of \mathbf{R}_{zz} :

$$\mathbf{R}_{zz} = E(\mathbf{z}\mathbf{z}^H) = \sum_{n=1}^{MN} \lambda_n \mathbf{u}_n \mathbf{u}_n^H. \quad (12)$$

The eigenvectors of the correlation matrix are divided into two subspaces: the signal subspace $\mathbf{U}_s = \text{span}\{\mathbf{u}_1, \mathbf{u}_1, \dots, \mathbf{u}_d\}$ and the noise subspace $\mathbf{U}_N = \text{span}\{\mathbf{u}_{d+1}, \mathbf{u}_{d+2}, \dots, \mathbf{u}_{MN}\}$.

Define two-dimensional full-polarization MUSIC spectrum for a radar target as

$$P_{2\text{DP-MUSIC}}(\alpha, x, y) = \frac{\mathbf{a}(\alpha, x, y)^H \mathbf{a}(\alpha, x, y)}{\mathbf{a}(\alpha, x, y)^H \mathbf{U}_N \mathbf{U}_N^H \mathbf{a}(\alpha, x, y)}. \quad (13)$$

Theoretically speaking, through 3D search, the position (x, y) and the type factor α of each scattering center can be estimated. Since the CP-GTD model is adopted here, the estimations for the position and the type are consistent in every polarization channel, which is very useful because it can guarantee the coherence of different polarization channels.

In order to decrease the computation burden in 3D search, let $\alpha = 0$ and estimate the position of the scattering centers firstly:

$$P_{2\text{DP-MUSIC}}(x, y) = \frac{\mathbf{b}^H(x, y) \mathbf{b}(x, y)}{\mathbf{b}^H(x, y) \mathbf{U}_N \mathbf{U}_N^H \mathbf{b}(x, y)}. \quad (14)$$

When searching (x, y) , a roughly searching method can be used firstly and thereby the accurate estimation by a local searching method based on the rough estimation is suggested.

Once (\hat{x}, \hat{y}) has been derived, searching is only needed for the discrete values of the frequency-dependent factors. The signal steering vector's projection on the signal subspace will reach the maximum when the estimation of α is consistent with the true value at the right range; namely,

$$P(\alpha | (\hat{x}_i, \hat{y}_i)) = \frac{\mathbf{b}^H(\hat{x}_i, \hat{y}_i) \Gamma^H(\alpha) \Gamma(\alpha) \mathbf{b}(\hat{x}_i, \hat{y}_i)}{\mathbf{b}^H(\hat{x}_i, \hat{y}_i) \Gamma^H(\alpha) \mathbf{U}_N \mathbf{U}_N^H \Gamma(\alpha) \mathbf{b}(\hat{x}_i, \hat{y}_i)}. \quad (15)$$

After the position and type estimation of all scattering centers, the estimation of \mathbf{A} can be derived by (9). Then the estimation of \mathbf{s} matrix can be obtained using least square (LS) criterion as follows:

$$\hat{\mathbf{s}} = (\widehat{\mathbf{A}}^H \widehat{\mathbf{A}})^{-1} \widehat{\mathbf{A}} \mathbf{z}. \quad (16)$$

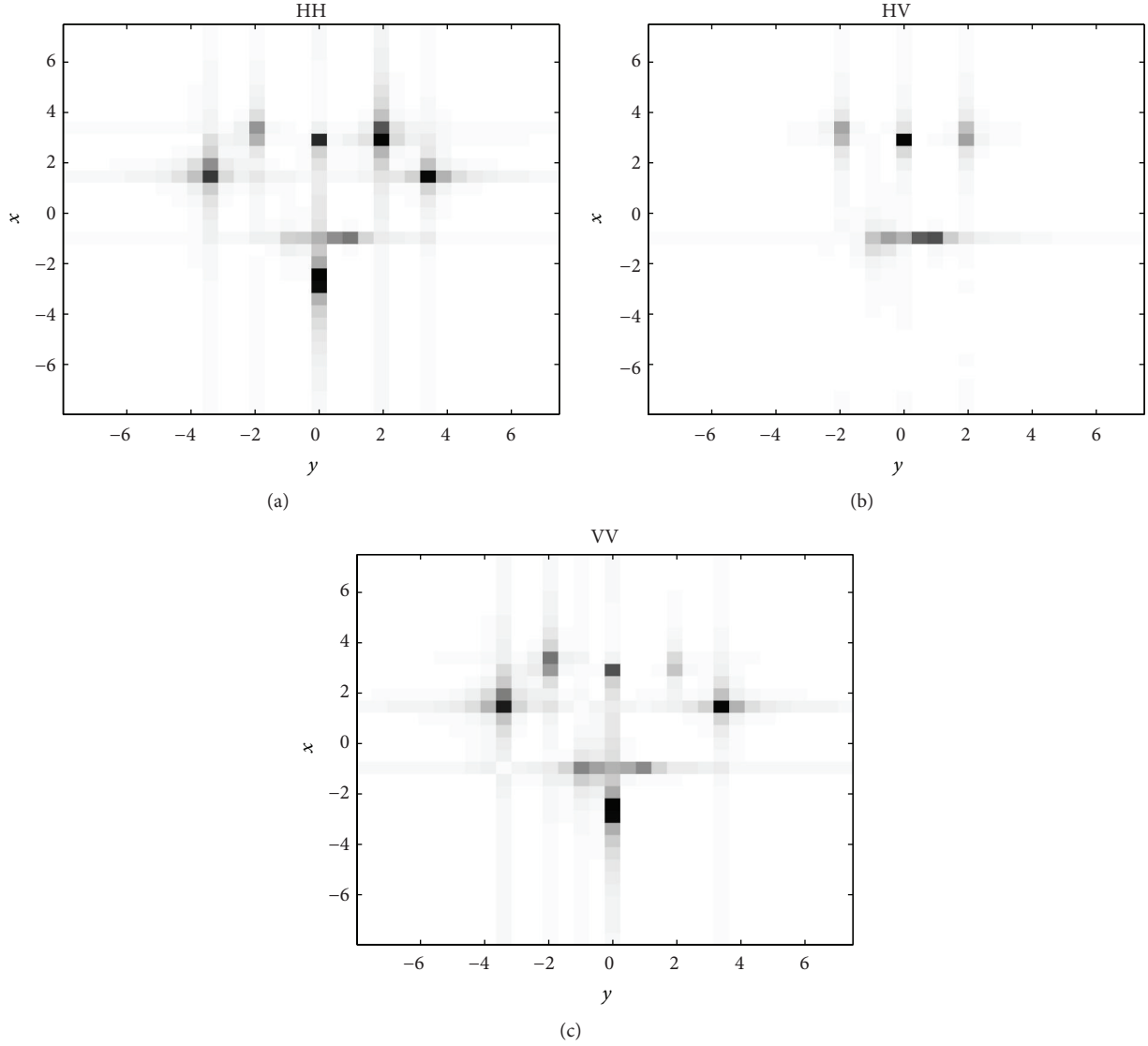


FIGURE 1: The full-polarization ISAR results using conventional FFT method.

Rearrange i th row of $\widehat{\mathbf{s}}$ as $\widehat{\mathbf{S}}_i = \begin{bmatrix} \widehat{S}_{i,HH} & \widehat{S}_{i,HV} \\ \widehat{S}_{i,VH} & \widehat{S}_{i,VV} \end{bmatrix}$, with $\widehat{\mathbf{S}}_i$ as the fully polarized scattering matrix of the i th scattering center. It can be figured out that the span (total power) I_i and normalized scattering matrix $\widehat{\widehat{\mathbf{S}}}_i$ are

$$I_i = |\widehat{S}_{i,HH}|^2 + |\widehat{S}_{i,HV}|^2 + |\widehat{S}_{i,VH}|^2 + |\widehat{S}_{i,VV}|^2, \quad (17)$$

$$\widehat{\widehat{\mathbf{S}}}_i = \frac{\widehat{\mathbf{S}}_i}{\sqrt{I_i}} \exp(-j \arg(\widehat{S}_{i,HH})).$$

The other fully polarized characteristic just like polarization invariables can also be calculated for RTR [10], where $\arg(\cdot)$ denotes the phase angle.

In fact, although the algorithm is studied aiming at the fully polarized stepping frequency signal, it is also applicable

for linear frequency modulated (LFM) signal, and it is compatible with the case of single or double polarization processing (they are just some simple forms of the CP-GTD method). It is a joint processing of polarization and superresolution. It can estimate the number, type factor, position, span, and normalized scattering matrix of scattering centers instantaneously for each channel rather than extracting parameters from every channel separately. Its performance is better than the latter because the fully polarized information is used. The number and the location of scattering centers in each channel are consistent. This characteristic saves complexity in the scattering centers association in different polarizations.

Before applying the modified 2D MUSIC algorithm presented above, the number of the scattering centers and the fully polarized correlation matrix \mathbf{R}_{zz} must be estimated. If the estimation \widehat{d} is less than the true value, some real scattering center will be lost. Contrarily, if the estimation is less than the true value, some false scattering centers will

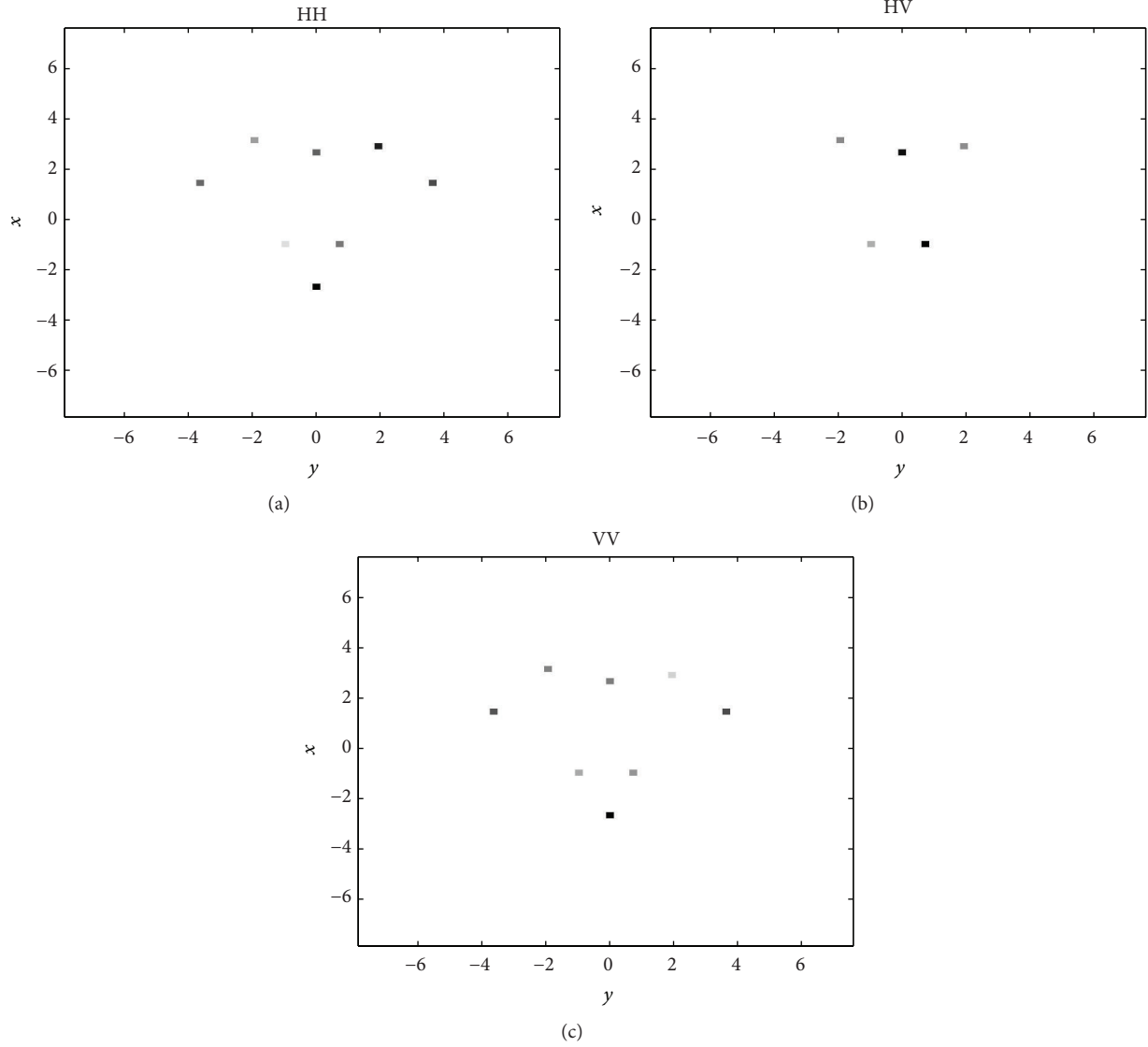


FIGURE 2: The superresolution ISAR results using modified MUSIC algorithm based on 2D CP-GTD model.

appear because of noise. Generally, when the SNR (signal-to-noise ratio) is high enough, the number of scattering centers can be estimated by observing the eigenvalues of \mathbf{R}_{zz} . However, this method is subjective and sensitive to the SNR. The Gerschgorin Disk method is adopted because it is not sensitive to the SNR which is fit for the situation in this paper [14].

To estimate the fully polarized correlation matrix \mathbf{R}_{zz} , a preprocessing scheme known as SSP (spatial smoothing

preprocessing) can be used. For idea point scattering condition, Odendaal et al. [15] applied the MSSP (Modified SSP) to estimate the singly polarized correlation matrix and Kim et al. [5] extended and generalized it in order to estimate the fully polarized correlation matrix. However, considering that the MSSP will disturb the estimation of type, SSP is still adopted here.

A set of L overlapping subarrays with dimensions $p_1 p_2 \times 4$ is defined as

$$\mathbf{z}_l = \begin{bmatrix} x_{HH}(l, l) & x_{HV}(l, l) & \cdots & x_{VV}(l, l) \\ x_{HH}(l+1, l) & x_{HV}(l+1, l) & \cdots & x_{VV}(l+1, l) \\ \vdots & \vdots & \ddots & \vdots \\ x_{HH}(l+p_1-1, l+p_2-1) & x_{HV}(l+p_1-1, l+p_2-1) & \cdots & x_{VV}(l+p_1-1, l+p_2-1) \end{bmatrix}. \quad (18)$$

Applying the full-polarization SSP, the fully polarized correlation matrix is obtained as

$$\widehat{\mathbf{R}}_{zz} = \frac{1}{L} \sum_{l=1}^L \widehat{\mathbf{R}}_l, \quad (19)$$

where $L = (M - p_1 + 1) \times (N - p_2 + 1)$ and $\widehat{\mathbf{R}}_l = \mathbf{z}_l \mathbf{z}_l^H$. In order to obtain an exclusive LS solution of $\widehat{\mathbf{s}}$ in (16), we should make sure that $\widehat{\mathbf{A}}^H \widehat{\mathbf{A}}$ is not singular; that is to say, $p_1 p_2 > d$.

To sum up, the flow chart on the CP-GTD algorithm is as follows.

Step 1. Estimate the full-polarization covariance matrix. Choose the forward smoothing algorithm (see (19)).

Step 2. With the eigendecomposition of the full-polarization covariance matrix, use the Gerschgorin Disks to estimate the number of the scattering centers (see (12)).

Step 3. Estimate the ranges of the scattering centers using the full-polarization MUSIC spectrum search (see (14)).

Step 4. Estimate the frequency-dependent factor of each scattering center (see (15)).

Step 5. The estimation of \mathbf{s} matrix can be obtained using least square (LS) criterion (see (16)).

Step 6. Calculate the span and normalized scattering matrix (see (17)).

Step 7. Classify the attribute of each scattering center and apply the result to target recognition.

4. Performance Analysis

To evaluate the performance of the CP-GTD method, we choose the conventional FFT method and the singly polarized GTD method as comparisons. The last two kinds of method present the progress of extracting the scattering centers in each polarization channel and, then, associating the scattering centers in multiple polarization channels and gathering the associated scattering coefficient in each channel together as the estimation of scattering matrix of the scattering center.

4.1. Evaluation Criteria. The evaluation indexes are classified into two types: one is used to evaluate accuracy of the noncoherent parameters, including the number, type, range, and span of scattering centers. Here assuming that both the traditional GTD method and CP-GTD method are capable of estimating the number of scatterers correctly, we choose the mean square roots of the last three estimated errors as the evaluation indicators corresponding to the estimating accuracy of the noncoherent parameters. The criterion σ_r is defined by

$$\sigma_r = \sqrt{E[(r - \widehat{r})^2]} = \sqrt{E[(x - \widehat{x})^2 + (y - \widehat{y})^2]}. \quad (20)$$

Similarly, $\sigma_\alpha = \sqrt{E[(\alpha - \widehat{\alpha})^2]}$ and $\sigma_I = \sqrt{E[(I - \widehat{I})^2]}$, where $E[\cdot]$ denotes the assembly average.

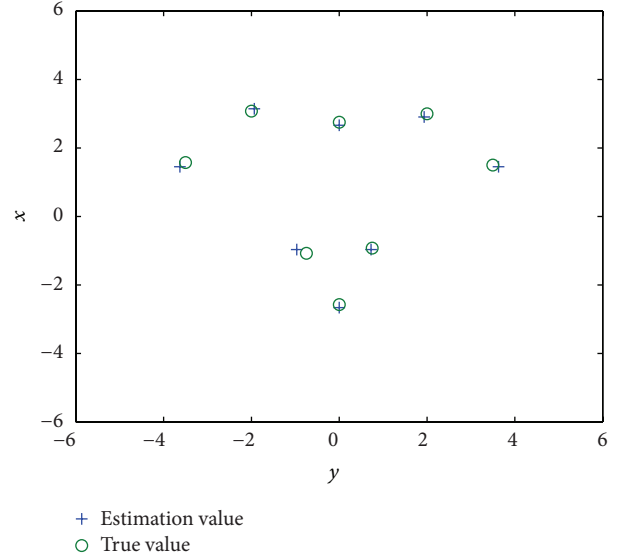


FIGURE 3: The comparison between the true position value and the estimation position value.

The other type is used to evaluate accuracy of the coherent parameters. As we all know, the scattering matrix is a complex matrix, and the phase of each element in the scattering matrix, especially the relative phase difference, is the important information which exactly reflects the polarimetric scattering mechanism of the radar target. Under the condition of symmetry, the coherent polarization scattering matrix includes three relative phases, namely, ϕ_{VV-HH} , ϕ_{HV-HH} , and ϕ_{HV-VV} (where $\phi_{VV-HH} = \arg(S_{VV} S_{HH}^*)$ is the phase difference of the elements s_{VV} and s_{HH} in the scattering matrix). Choose the mean square roots of the above three difference phases' estimated errors as the evaluation criteria corresponding to the estimating accuracy of the coherent parameters; namely,

$$\sigma(\phi_{VV-HH}) = \sqrt{E[(\phi_{VV-HH} - \widehat{\phi}_{VV-HH})^2]}. \quad (21)$$

$\sigma(\phi_{HV-HH})$ and $\sigma(\phi_{HV-VV})$ are defined similarly.

4.2. Simulation Results. An aircraft type target whose size was about $6\text{ m} \times 8\text{ m}$ defined by a set of eight point scatterers as shown in Figure 3 was used to generate raw data of ISAR over a frequency-angular domain. The initial frequency is 8.75 GHz; the frequency step is 10 MHz, the number of frequency points is 32; the total angle is 1.97° ; $p_1 = 5$, $p_2 = 5$; the Monte-Carlo number is 1000; and the signal-to-noise Ratio (SNR) is 25 dB. The SNR is defined as the ratio of the target span and noise intensity; namely, $\text{SNR} = 10 \lg(I/(4 \times \sigma^2))$. The results of full-polarization ISAR are given in Figure 1.

Figure 1 shows the full-polarization ISAR results using conventional FFT method (where the units of axes are

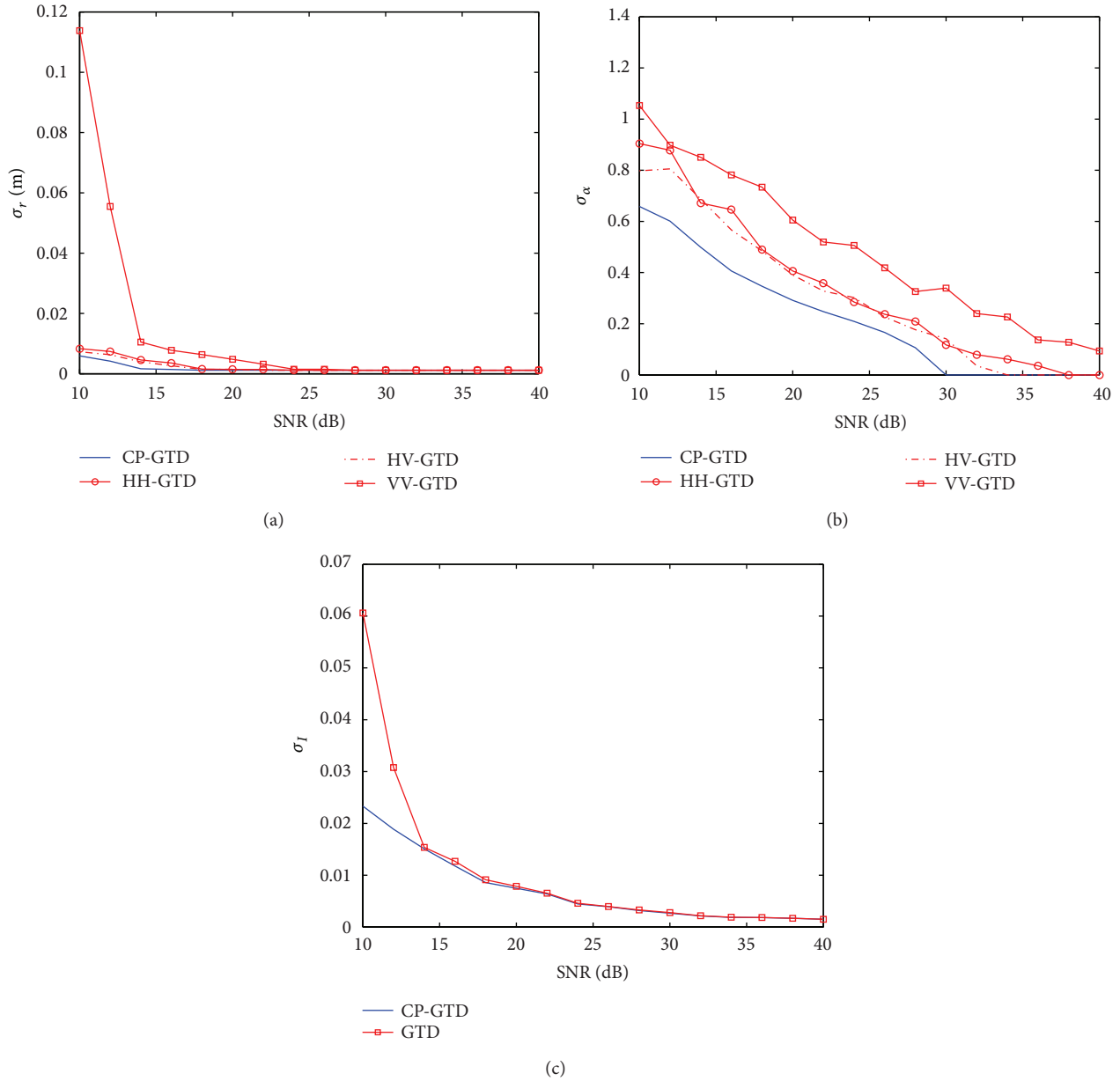


FIGURE 4: The comparison of noncoherent evaluation criteria.

both meter). Figure 2 shows the results using 2D CP-GTD algorithm. Figure 3 shows the comparison between the true position value and the estimation position value. As shown in these figures, some scattering centers cannot be distinguished due to the resolution limitation, which, in return, the scattering matrix of the extracted scattering center obviously cannot correctly reflect the polarimetric information of radar target. Furthermore, the conventional FFT processing cannot estimate the type of the scattering centers. Our 2D CP-GTD algorithm can realize superresolution and estimate the position and other parameters exactly.

The compared evaluating results of the noncoherent evaluation criteria and the coherent criteria in different SNR

situations are, respectively, given in Figures 4 and 5. From the two figures, some conclusion can be derived as following.

The new algorithm has better performance than the conventional singly polarized GTD algorithm both for noncoherent criteria and for coherent evaluation criteria. Especially, for coherent evaluation criteria, the CP-GTD method has more superiority. In order to guarantee the coherence of the scattering matrix, the SNR should be higher than 35 dB for the conventional GTD algorithm. However, for the new algorithm, the requirement of SNR can decline to 15 dB. For other parameters' estimation including the position, type, and span, the CP-GTD method also has better performance than conventional GTD method. This is

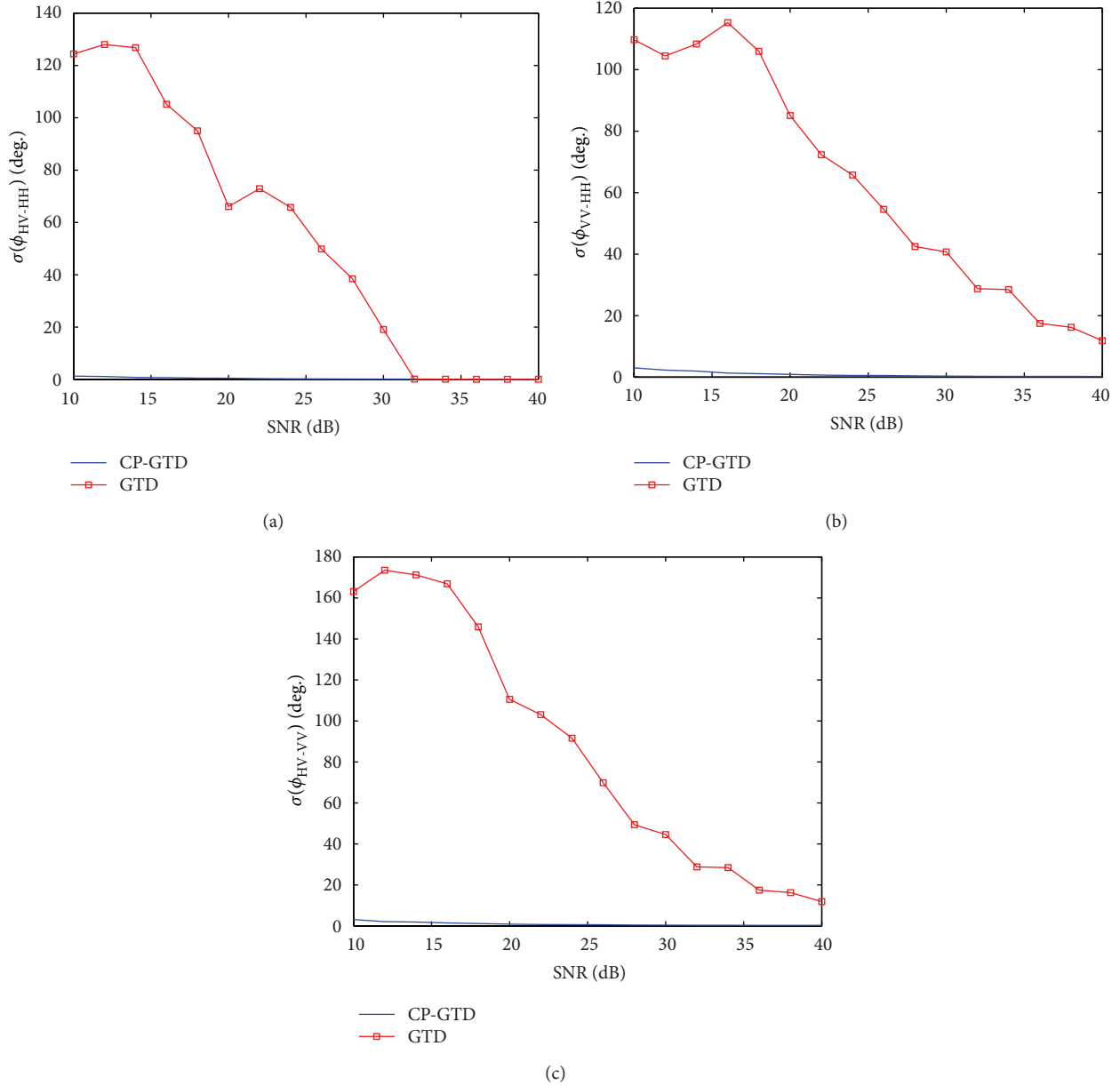


FIGURE 5: The comparison of coherent evaluation criteria.

because the CP-GTD approach is essentially a kind of joint processing based on high resolution and polarization. When estimating the covariance matrix, it makes good use of the full-polarization information from all channels and the SNR is elevated. Besides, the CP-GTD approach is related to only one full-polarization correlation matrix and makes the matrix decomposition only once; therefore, compared to the single processing in each channel, its characteristic extraction has a quicker velocity and higher efficiency.

4.3. Results Based on the Real Data. Figures 6 and 7 show the fully polarized ISAR imaging result of some warhead model with conventional FFT processing and CP-GTD method. The real data is acquired in an anechoic chamber. The target is a

model of some warhead with wing whose size is about 2.1×0.65 m. The initial frequency is 8.75 GHz, the frequency step is 20 MHz, the number of frequency points is 101, the pitching angle is 15° , and the azimuth angle is 0° . It can be seen that the warhead has eight scattering centers which locate at the nose, the middle, and the tail, respectively. Since the model has wings at tail, there are more scattering centers at its tail than at the other part. Its length which is calculated from the scattering center extraction results is almost equal to the true length. And the norm scattering matrix at the nose is very close to that of an idea sphere $(1/\sqrt{2}) \begin{bmatrix} 1 & 0 \\ 0 & 1 \end{bmatrix}$ (see Figures 6 and 7), which can confirm that fully polarized information can reveal the target's structure and prove the CP-GTD algorithm is very promising in RTR.

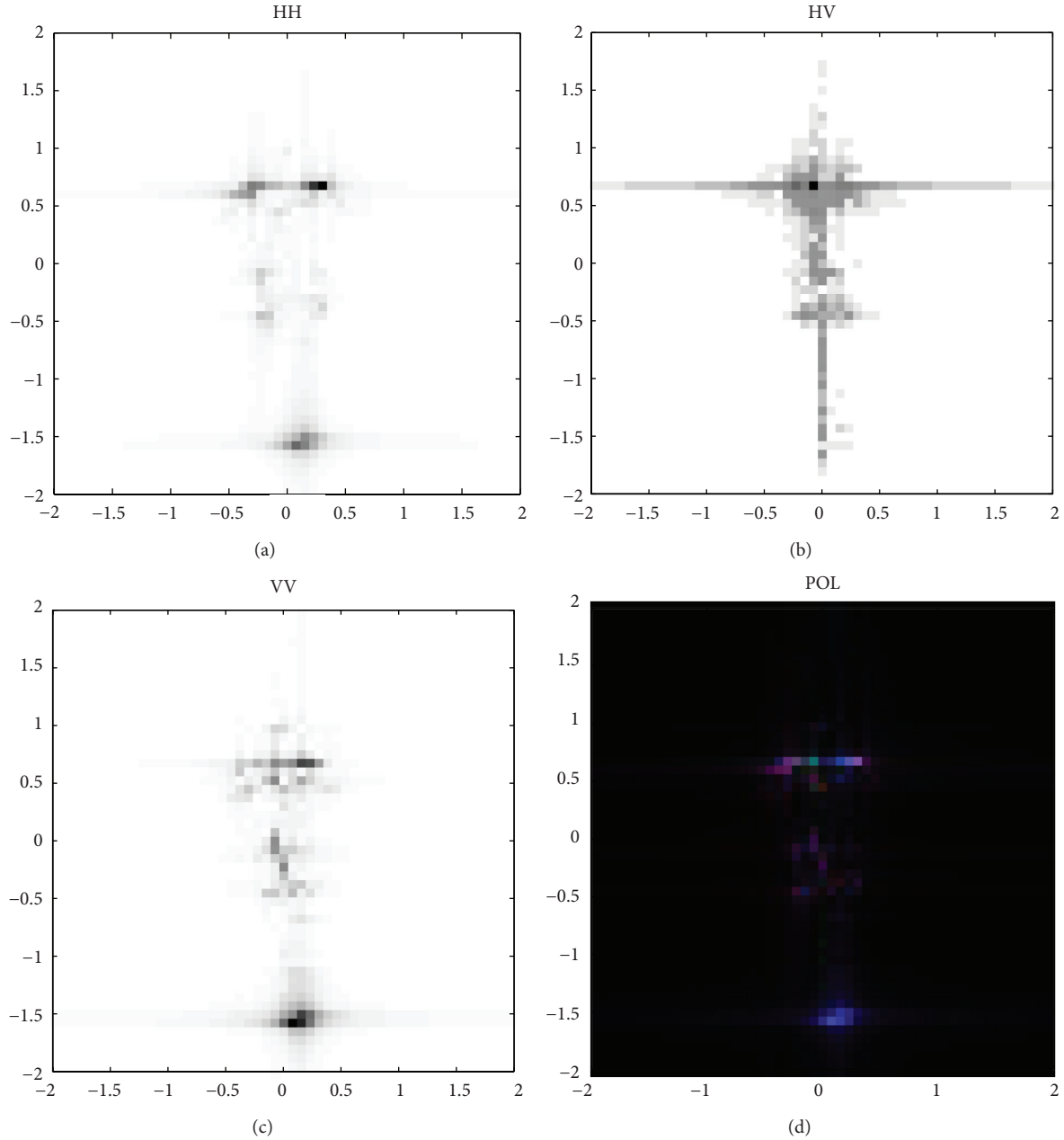


FIGURE 6: The fully polarized ISAR imaging result of some model with conventional FFT processing.

It is worthy of note that the colorful images in Figures 6 and 7 use the Pauli-based color combination (red: $|HH - VV|$, green: $|HV|$, and blue: $|HH + VV|$) to reveal the scattering characteristics of scattering centers. These results show that the full-polarization ISAR superresolution using modified MUSIC based on 2D CP-GTD model gives more faithful description for scattering centers associated with the radar target than the conventional FFT method and the existing singly polarized superresolution techniques. The increase of information contained in the full-polarization ISAR super-resolution image from the proposed algorithm is especially useful for radar target recognition application.

5. Conclusion

We have presented a new model named 2D CP-GTD model which can exactly match the high-frequency polarization scattering mechanism for full-polarization ISAR. We have also proposed a modified MUSIC algorithm based on 2D CP-GTD model for full-polarization ISAR superresolution and feature extraction. The new algorithm can estimate the number, location, frequency-dependent factor, span, and coherent polarization scattering matrix of scattering centers simultaneously and accurately.

The CP-GTD approach is not just a simple extension of traditional methods but a joint processing of polarization and

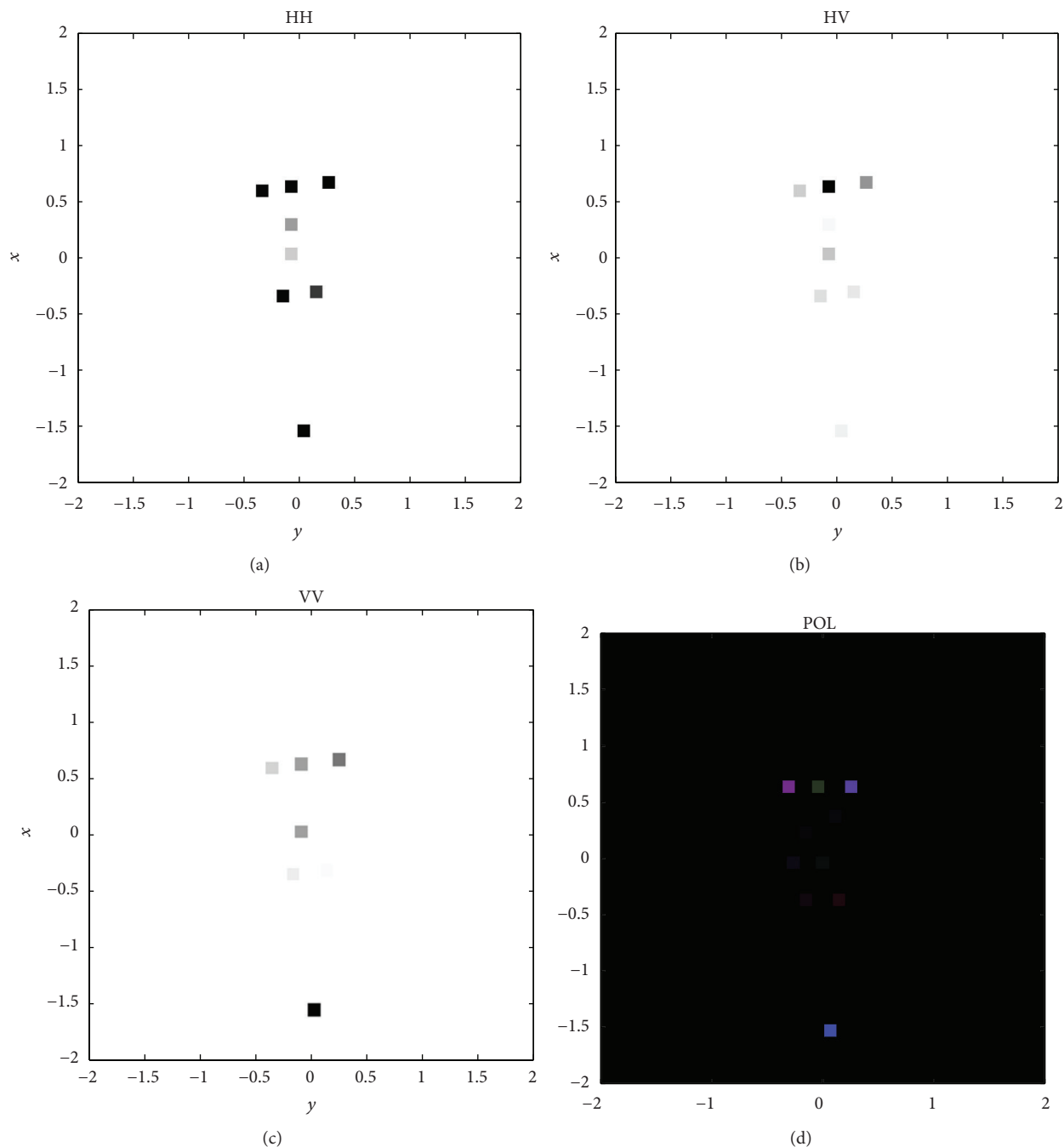


FIGURE 7: The fully polarized ISAR imaging result of some model using CP-GTD method.

superresolution essentially. What distinguishes it from the existing models is its consideration of the exclusive polarization scattering matrix of each scattering center. Its prominent strongpoint is that the scattering centers association is not needed any more and the coherent scattering matrixes of scattering centers can be estimated exactly. The utilization of the full-polarization information has improved the scattering centers extraction velocity and the estimation accuracy.

The objective of ISAR is to achieve target identification. This paper applies the CP-GTD methods to better focus on

scattering centers. It is very promising to enhance target identification by the joint processing of polarization and superresolution essentially.

Conflict of Interests

The authors declare that there is no conflict of interests regarding the publication of this paper.

Acknowledgments

This work is supported partly by the National Natural Science Foundation of China (no. 61302143) and National High-Tech R&D Program of China (no. 2013AA122202).

References

- [1] H. A. Zebker and J. J. van Zyl, "Imaging radar polarimetry: a review," *Proceedings of the IEEE*, vol. 79, no. 11, pp. 1583–1606, 1991.
- [2] W. M. Boerner, *Direct and Inverse Methods in Radar Polarimetry*, Kluwer Academic Publishers, Dordrecht, The Netherlands, 1992.
- [3] W. M. Steedly and R. L. Moses, "High resolution exponential modeling of fully polarized radar returns," *IEEE Transactions on Aerospace and Electronic Systems*, vol. 27, no. 3, pp. 459–469, 1991.
- [4] L. C. Potter, D.-M. Chiang, R. Carriere, and M. J. Gerry, "GTD-based parametric model for radar scattering," *IEEE Transactions on Antennas and Propagation*, vol. 43, no. 10, pp. 1058–1067, 1995.
- [5] K. T. Kim, S. W. Kim, and H. T. Kim, "Two-dimensional ISAR imaging using full polarisation and super-resolution processing techniques," *IEE Proceedings—Radar, Sonar and Navigation*, vol. 145, no. 4, pp. 240–246, 1998.
- [6] D.-H. Dai, X.-S. Wang, Y.-L. Chang, J.-H. Yang, and S.-P. Xiao, "Fully-polarized scattering center extraction and parameter estimation: P-ESPRIT algorithm," in *Proceedings of the CIE International Conference on Radar (ICR '06)*, pp. 97–100, Shanghai, China, October 2006.
- [7] D. F. Fuller, A. J. Terzuoli, P. J. Collins, and R. Williams, "Approach to object classification using dispersive scattering centres," *IEE Proceedings—Radar, Sonar and Navigation*, vol. 151, no. 2, pp. 85–90, 2004.
- [8] E. Ertin and L. C. Potter, "Polarimetric classification of scattering centers using M-ary Bayesian decision rules," *IEEE Transactions on Aerospace and Electronic Systems*, vol. 36, no. 3, pp. 738–749, 2000.
- [9] D. F. Fuller, A. J. Terzuoli, P. J. Collins, and R. Williams, "Approach to object classification using dispersive scattering centres," *IEE Proceedings: Radar, Sonar and Navigation*, vol. 151, no. 2, pp. 85–90, 2004.
- [10] V. Karnychev, V. A. Khlusov, L. P. Ligthart, and G. Sharygin, "Algorithms for estimating the complete group of polarization invariants of the Scattering Matrix (SM) based on measuring all SM elements," *IEEE Transactions on Geoscience and Remote Sensing*, vol. 42, no. 3, pp. 529–539, 2004.
- [11] F. Wang, R. Guo, and Y. Huang, "Radar target recognition based on some invariant properties of the polarization scattering matrix," in *Proceedings of the 6th IEEE CIE International Conference on Radar (RADAR '11)*, pp. 626–629, October 2011.
- [12] A. Quinquis, E. Radoi, and F.-C. Totir, "Some radar imagery results using superresolution techniques," *IEEE Transactions on Antennas and Propagation*, vol. 52, no. 5, pp. 1230–1244, 2004.
- [13] R. O. Schmidt, "Multiple emitter location and signal parameter estimation," *IEEE Transactions on Antennas and Propagation*, vol. 34, no. 3, pp. 276–280, 1986.
- [14] H.-T. Wu, J.-F. Yang, and F.-K. Chen, "Source number estimators using transformed Gerschgorin radii," *IEEE Transactions on Signal Processing*, vol. 43, no. 6, pp. 1325–1333, 1995.
- [15] J. W. Odendaal, E. Barnard, and C. W. I. Pistorius, "Two-dimensional superresolution radar imaging using the MUSIC algorithm," *IEEE Transactions on Antennas and Propagation*, vol. 42, no. 10, pp. 1386–1391, 1994.

Research Article

Impact of Topography and Tidal Height on ALOS PALSAR Polarimetric Measurements to Estimate Aboveground Biomass of Mangrove Forest in Indonesia

S. Darmawan,^{1,2,3} W. Takeuchi,¹ Y. Vetrta,⁴ K. Wikantika,² and D. K. Sari³

¹*Institute of Industrial Science, University of Tokyo, Tokyo 153-8505, Japan*

²*Center for Remote Sensing, Institut Teknologi Bandung (ITB), Bandung 40132, Indonesia*

³*Institut Teknologi Nasional (ITENAS), Bandung 40124, Indonesia*

⁴*Indonesian National Institute of Aeronautics and Space (LAPAN), Jakarta 13710, Indonesia*

Correspondence should be addressed to S. Darmawan; soni_darmawan@yahoo.com

Received 7 January 2015; Accepted 24 April 2015

Academic Editor: Jian Yang

Copyright © 2015 S. Darmawan et al. This is an open access article distributed under the Creative Commons Attribution License, which permits unrestricted use, distribution, and reproduction in any medium, provided the original work is properly cited.

This study is focused on investigating the impact of topography and tidal height on ALOS PALSAR polarimetric measurements on HH and HV for estimating aboveground biomass (AGB) of mangrove forest in Indonesia. We used multitemporal ALOS PALSAR polarimetric measurement that covered mangrove zone in Banyuasin, Cilacap, and Teluk Bintuni and also collected tidal height data within the same acquisition date with multitemporal ALOS PALSAR polarimetric measurement. We analyzed the distribution of flooding and nonflooding areas based on tidal height and SRTM topography data, created three profiles as region of interest (ROI), and got characteristics of backscatter value on HH and HV with different tidal height. The result of this study showed backscatter of the open mangrove zones during high tide with HH value less than -20 dB and HV value less than -25 dB whereas during low tide it showed an HH value around -20 to -10 dB and HV value around -25 to -10 dB. Backscatter of the middle mangrove zones at Cilacap, with low and flat topography, showed a deviation of backscatter on HV value of 1.6 dB. Finally, the average AGB of mangrove forest in Indonesia was estimated based on ALOS PALSAR polarimetric measurements.

1. Introduction

The term of “mangrove” is used to define both the plants that populate the tidal forests and to describe the community itself [1–3]. Mangrove forests can be found along ocean coastlines throughout the tropics and provide important products and services [4]. They are also among the most intense coastal carbon sinks in the world and play a growing and central role in the global carbon cycle [5]. According to Donato et al. [6] mangroves have five times larger number of total carbon storage per unit area basis on average than those typically observed in temperate, boreal, and tropical terrestrial forests. This suggests that mangroves play an important role in global climate change management. In order to gain and build a solid understanding of the global carbon budget and ultimately the effects of diminishing mangrove forests on climate change, it is crucial to obtain an assessment and

quantification of the spatial distribution of mangrove forest biomass. Indonesia has the largest mangroves area in the world, covering an area around 3.5 million ha or around 17%–23% of all mangrove areas in the world [7]. The loss of more than 50% of global mangrove area in recent years suggested the growing importance of mapping and monitoring biomass of mangrove forest. However, conducting field survey for mangrove biomass and its productivity in Indonesia region is proven to be very difficult due to muddy soil condition, heavy weight of the wood [8], the vast area to cover, and tidal influences.

Remote sensing has been widely proven to be essential in monitoring and mapping highly threatened mangrove ecosystems. Tropical and subtropical coastal mangroves are among the most threatened and vulnerable ecosystems worldwide [4]. According to Henderson and Lewis [9], although sensors in the optical range of the electromagnetic

spectrum have received the greatest attention, considerable effort has also been focused on the use of imaging radars. There are many reasons to use radar to monitor and map mangrove ecosystems. As radar operates in the microwave portion of the spectrum, it offers complementary and supplementary data to sensors operating in the optical and thermal bands. At the same time, it also patently provides unique data. Radar backscatter is sensitive to dielectric properties (soil and vegetation moisture content) and geometric (surface roughness) attributes of the imaged surface. In many areas of the world (e.g., cloud-covered and/or low-light regions of the Earth) imaging radar is the only sensor that can provide consistent, periodic data in reliable manner. Optical and thermal systems are also limited by their inability to penetrate vegetation canopies whereas radar systems can, to some degree, provide subcanopy information.

The launch of the Japanese Space Exploration Agency's (JAXA) Advanced Land Observing Satellite (ALOS) Phased Arrayed L-band SAR (PALSAR) in 2006 therefore represented a milestone in the global observation, characterization, mapping, and monitoring of mangroves largely, because these provide more information on the three-dimensional structure and biomass of woody vegetation, as well as the presence and the extent of (primarily tidal) inundation. As data can be days or night regardless of weather conditions, mangroves can be observed more frequently, even in regions with prevalent cloud cover. ALOS-PALSAR penetrates through the foliage and interacts primarily with the woody components of vegetation. Horizontally transmitted waves are either depolarized through volume scattering by branches in the canopy, with a proportion of vertically polarized microwaves returning to the sensor, or penetrate through the canopy and interact with the trunks, returning primarily through double bounce scattering as a horizontally polarized wave [10]. Longer L-band microwaves have a greater likelihood of penetrating the foliage and small branches at the upper canopies of the forest and interacting with woody trunk and larger branch components as well as the underlying surface [11, 12]. L-band SAR (1.3 GHz, 23.5 cm) generally provides greater penetration of forest canopies than does the shorter C-band (5.3 GHz, 5.7 cm) because the wavelength is longer than leaf sizes within the forest canopy [13–17]. Thus, ALOS PALSAR is proven to be potential to estimate aboveground biomass of mangrove forest [8, 10, 18, 19]. The modeling approach treats tree canopy, tree trunks, and ground surface as layered scattering media that scatter and attenuate the incoming microwave energy. The model has four components: surface backscatter (σ_s°), canopy volume scattering (σ_c°), multiple path interactions of canopy-ground (σ_m°), and double bounce trunk-ground interactions (σ_d°). Incoherent summation of the components results in total backscatter (σ_t°) with the algorithms as shown in the following [14]:

$$\sigma_t^\circ = \sigma_s^\circ + \sigma_c^\circ + \sigma_m^\circ + \sigma_d^\circ. \quad (1)$$

The sensitivity of the backscatter to forest parameters and the saturation level is rather sites-dependent, since forest structure influences the relative contribution of the scattering mechanism [12, 19, 20]. In addition, the individual

contribution to the total forest backscatter is also dependent on environmental conditions (i.e., weather conditions, moisture conditions, and weather dynamics) which can affect the dielectric properties of the vegetation and ground surface. The interactions between the radiation and the plant's internal properties (e.g., moisture content influencing the dielectric constant of a material and cell structure) and external components (e.g., size, geometry, and orientation of leaves, trunks, branches, and aerals or stilt roots) also result in a specific backscatter signal [4, 19]. The unique location of mangroves at the zones of transition between terrestrial and marine ecosystem that occurs in tidal forest and the capability of L-band to penetrate until underlying surface lead to a question of the probable impact of tidal height on characteristics of ALOS PALSAR measurement. Hence, the objective of this research is to investigate the impact of topography and tidal height on characteristics of HH and HV derived from ALOS PALSAR measurements for the estimation of aboveground biomass of mangrove forest.

2. Study Area

Indonesia is a country in Southeast Asia that is located on 6° N–11° S and 95° E–141° E, between the Asian and Australian continents, and between the Pacific and Indian Oceans. Indonesia has approximately 17,500 islands and is considered to be the largest archipelagic country in the world. Generally mangroves can be found throughout the Indonesian archipelago, with the largest mangrove area of around 1.3 million ha (38%) found in Papua, around 978 thousand ha (28%) in Kalimantan, and 673 thousand ha (19%) in Sumatera [7]. Indonesian mangrove area can be categorized into four zones [7]. The first is the open zones which sit at the forefront of the sea and the majority of its mangrove types are *Sonneratia alba*. The second is middle zones, which sit behind the open zones and the majority of its mangrove types are *Rhizophora*. The third is payau zone, located along the river, and the majority of its mangrove types are *Nypa* or *Sonneratia*. The fourth is land zone, located behind middle zones and payau zone, and is inhabited by a larger variety of plants species compared to the other three zones.

The area of study for this investigation of topography and tidal height impacts on ALOS PALSAR polarimetric measurements of HH and HV is focused on Banyuasin, South Sumatera (104.464 E, –1.897 N), Cilacap Central Java (108.832 E, –7.679 N) and Teluk Bintuni Papua (133.470 E, –2.525 N). The locations are specifically chosen for their representativeness of all mangrove forest in Indonesia. Profiling as samples of regions of interest (ROIs) was created in each study area. Each study area has three ROIs (e.g., Banyuasin: d1, d2, d3; Cilacap: k1, k2, k3; Teluk bintuni: q1, q2, q3) which can be seen in Figures 1(B), 1(C), and 1(D). The estimation for aboveground biomass is focused on twenty sites of mangrove zones in Indonesia as follows: (a) Langsa, Aceh, (b) Bengkalis, Riau, (c) Indragiri Hilir, Riau, (d) Banyuasin, South Sumatera, (e) Pontianak, West Kalimantan, (f) Kotabaru, South Kalimantan, (g) Kutai Kartanegara, East Kalimantan, (h) Berau, East Kalimantan, (i) Nunukan, East Kalimantan, (j) Subang, West Java, (k) Cilacap, Central Java, (l) Badung, Bali (m)

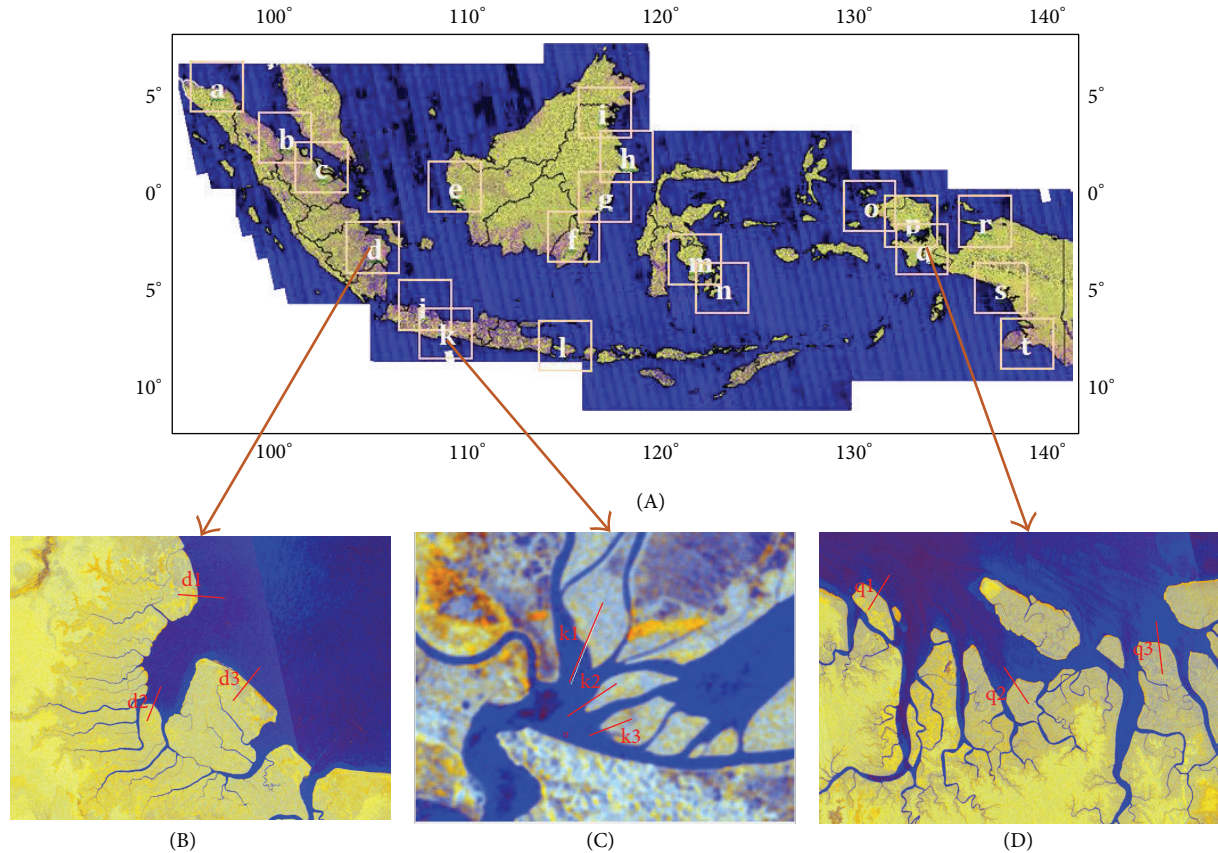


FIGURE 1: Study areas are twenty sites for estimation AGB in Indonesia (A) and ROI in Banyuasin, South Sumatera (B), Cilacap, Central Java (C), and Teluk Bintuni, Papua (D) for investigation impact of topography and tidal height.

Bombana, Southeast Sulawesi (n) Muna, Southeast Sulawesi, (o) Sorong, West Papua, (p) Teluk Bintuni, Papua, (q) Teluk Bintuni, Papua, (r) Waropen, Papua, (s) Asmat, Papua, and (t) Merauke Papua. Their location is shown in Figure 1(A).

3. Methodology

This study collected ALOS PALSAR data, ALOS PALSAR mosaics data, Shuttle Radar Topographic Missions (SRTM) data, and tidal height data. Preprocessing is focused on converting digital number to normalize radar cross sections (NRCS) and filtering of ALOS PALSAR data, profiling of ALOS PALSAR data and calculation of statistic, and calculation of aboveground biomass.

3.1. Data Used in This Study. We collected primary data of dual polarization ALOS PALSAR L-band HH and HV with spatial resolution of 12.5 m. Product ID H1.5 GUA with radiometric and geometric corrections are performed based on the map projection, fine mode was selected for pixel spacing, and the calculation of latitudes and longitudes in the product omitted the altitude. All data were acquired in fine beams dual modes at a viewing angle of 34.3 and delivered in single-look complex (SLC) as the normalized backscattering

coefficient in slant-range geometry by JAXA. ALOS PALSAR data collected in this study was described on Table 1.

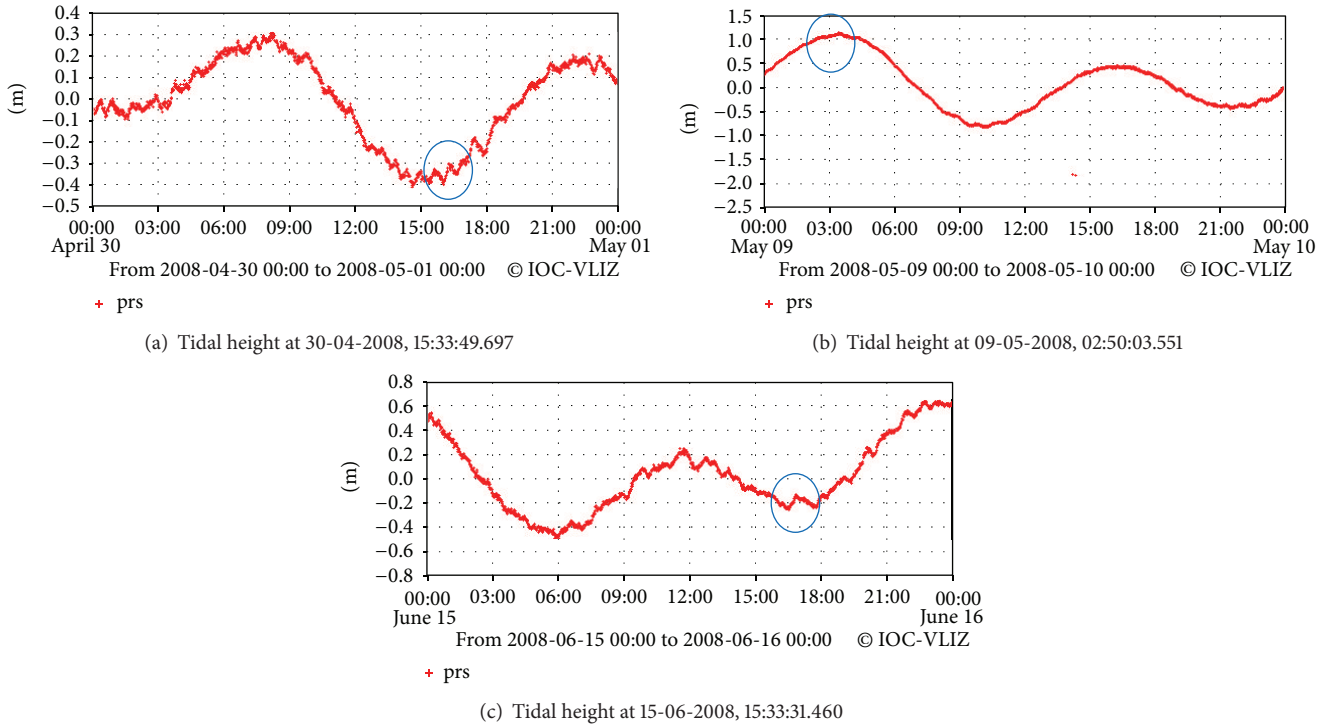
We also used dual polarization ALOS PALSAR L-band HH and HV spatial resolution 50 m orthorectified mosaic product in 2008 from Kyoto and Carbon Initiative.

For secondary data, we collected topography elevation data derived from SRTM which have spatial resolution approximately 90 meters and were processed by NASA and USGS. The data was projected in a Geographic (Lat/Long) projection, with the WGS84 horizontal datum and the EGM96 vertical datum. Another secondary data were sea level measurement data from <http://www.ioc-sealevelmonitoring.org/>. Tidal height data on mangrove zones in Cilacap is shown in Figure 2 as an example. The site has been expanded to a global station monitoring service for measuring of real times sea level that are part of Intergovernmental Oceanographic Commission (IOC) of UNESCO programs. According to Figure 2, the tidal height of ALOS PALSAR measurement at 30-04-2008 15:33:49.697, 09-05-2008 02:50:03.551, and 15-06-2008 15:33:31.460 is around -0.4 meters, 1.0 meter, and -0.2 meters, respectively.

3.2. Preprocessing and Biomass Estimation. Preprocessing was focused on converting digital number (DN) into normalize radar cross sections (NRCS) and filtering of ALOS PALSAR data. The conversion of HH (DN_{HH}) and HV (DN_{HV})

TABLE 1: ALOS PALSAR data was used on study.

Scene ID	Nadir angle	Polarizations	Acquisition date on scene center	Location
ALPSRP1 22177140	34.3	HH and HV	10052008-15:48:07.749	Banyuasin South Sumatera
ALPSRP1 28887140	34.3	HH and HV	25062008-15:47:35.329	
ALPSRP1 20717030	34.3	HH and HV	30042008-15:33:49.697	Cilacap West Java
ALPSRP1 21953770	34.3	HH and HV	09052008-02:50:03.551	
ALPSRP1 27427030	34.3	HH and HV	15062008-15:33:31.460	
ALPSRP1 29167130	34.3	HH and HV	27062008-13:52:53.001	Teluk Bintuni Papua
ALPSRP1 42587130	34.3	HH and HV	27092008-13:51:32.107	

FIGURE 2: Tidal height data corresponding to the same acquisition date with multitemporal ALOS PALSAR polarimetric measurements in Cilacap area (source: <http://www.ioc-sealevelmonitoring.org/>).

backscatter intensities into NRCS (i.e., σ_{HH}° and σ_{HV}°) was based on Shimada et al. [21], while for the reduction of speckle noise we used frost filtering with windows size 6×6 . The conversion of DN into NRCS used the following equations:

$$\begin{aligned} \sigma_{HH}^{\circ} &= 10 \log_{10} (DN_{HH}^2) - 83.2, \\ \sigma_{HV}^{\circ} &= 10 \log_{10} (DN_{HV}^2) - 83.2. \end{aligned} \quad (2)$$

The regions of interest (ROIs) of mangrove forest were determined based on land cover maps from Indonesian Ministry of Forestry and Indonesian base map from Badan Informasi Geospasial (BIG). ROI has the shape of line profiling with length of around 80 to 420 pixels. There were three ROIs of mangrove forest from ALOS PALSAR and SRTM data for each study area, all with calculated means and standard deviations. Several study [8, 10, 19] has established empirical relationships between L-band backscatter and aboveground

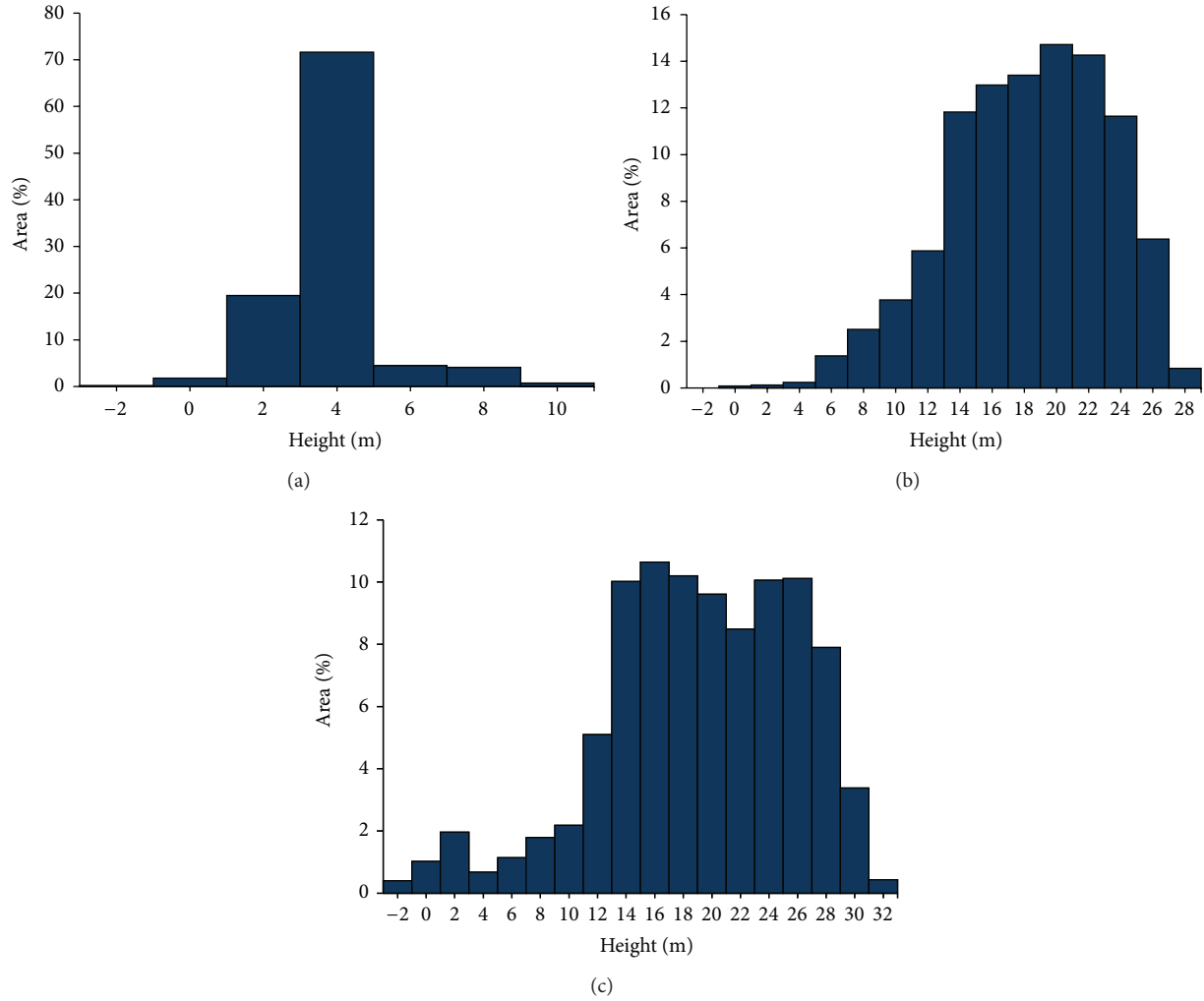


FIGURE 3: Level of topography at study area: (a) Cilacap, West Java, (b) Banyuasin, South Sumatera, and (c) Teluk Bintuni, Papua.

biomass (AGB) of mangrove forest. For this study, we calculated the aboveground biomass with the following equations [8]:

$$\begin{aligned}
 \text{HH} (\sigma^\circ) &= 3.6 \ln(\text{tree height}) - 23.7, \\
 \text{HV} (\sigma^\circ) &= 4.4 \ln(\text{tree height}) - 24.9, \\
 \text{tree height} &= 2.8 \ln(\text{DBH}) + 23.7, \\
 \text{AGB} &= 0.25 \text{DBH}^{2.46}.
 \end{aligned}
 \tag{3}$$

According to Lucas et al. [10], however, an understanding of microwave interaction with the forest volume has proven to be difficult to achieve using empirical relationships with SAR data due to inherent relationships between these components. The retrieval of component biomass was also more difficult in forests above the level of saturation (herein referred to as high biomass forests) compared with those below the level of saturation (low biomass forests), as greater attenuation by the crown volume reduces the diversity of scattering mechanisms between components and the ground surface. Hence, less information on the forest biomass and structure

(and therefore species, growth stage, and form) can be extracted. However, by considering the scattering mechanisms operating within low and high forests, separately, L-band SAR data can be better interpreted.

4. Results and Discussion

4.1. Flooding and Nonflooding on Mangrove Zones. Mangrove forests occupy zones of transition between terrestrial and marine ecosystems determined by the cumulative and complex interaction between hydrology, landscape positions, sediment dynamics, storm-driven processes, sea level change, and subsidence [22]. Tidal flooding patterns are important aspects of mangrove forest [23, 24]. Tidal flooding and surface drainage pattern have often been used to describe mangrove species zonation [25]. Tidal flooding distribution depends on level of topography and tidal height on study area. The level of topography at the study areas derived from SRTM is shown in Figure 3.

According to Figure 3, the dominant level of topography at Cilacap is 4 meters and less, covering around 90% of its

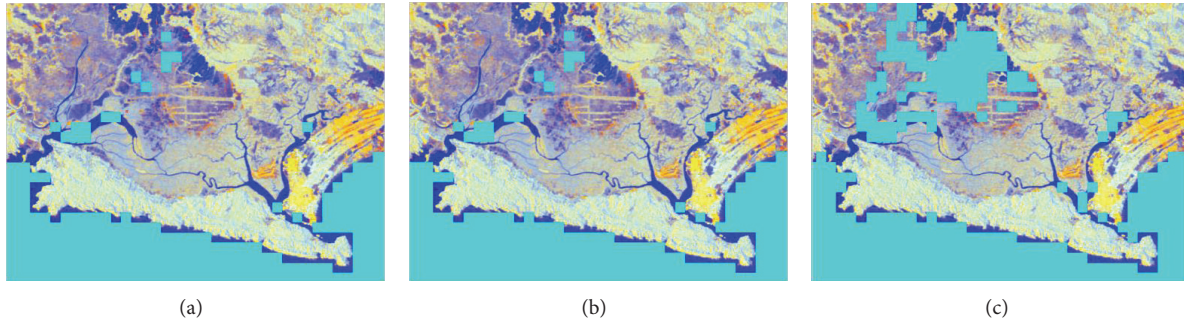


FIGURE 4: Illustration of distribution of flooding and nonflooding at mangrove zone from ALOS PALSAR composite and cyan colors is water (a) tidal height on -0.4 meters, (b) tidal height on -0.2 , and (c) tidal height on 1.0 meter.

total area. Different topographical characteristics are shown for Banyuasin and Teluk Bintuni, where both tend to have varieties of topography at higher height, leaving only around 10% of their total area with the height of 4 meters and less. It means that Cilacap area has relatively low and flat topography, while Banyuasin and Teluk Bintuni are situated at higher topography and have a wider variety of topographical features. It is worth noting that SRTM has a limited accuracy around 5 to 10 meters [26] for topography analysis on mangrove forest. But since more accurate topographical data was impossible to obtain during the study, that is, data derived from surveys terrestrial, photogrammetry, or LIDAR, we believe that this SRTM topography data was sufficient to provide general descriptions for the level of topography at the selected study areas.

The average annual tidal height on the study area is around -1.5 to 1.5 meters, and variances of tidal height will cause variances of flood areas to occur at mangrove zones. However, the size and the spatial distribution of flood areas at mangrove zones were also determined by the level of topography in study areas. Figure 4 illustrates the effect of the level of topography and tidal height to the distribution of flood areas in Cilacap.

Figure 4 shows how various tidal height caused differences in the size and spatial distribution of flood areas. The higher the tidal height is, the larger the areas of flood occurred. With the cyan pixel representing water, the map showed that tidal height of 1 meter can cause much larger areas of flood compared to those caused by much less tidal height. If the pattern continued, a tidal height of 4 meters shall have a very high probability to drown the entire area of mangrove zones due to the relatively low and flat topography of the area. And if we considered the zoning of mangrove areas [7], we can safely assume that the open zones experience stronger impact tidal height than middle zones or land zones. However, it is worth noting that the spatial distribution of flooding on mangrove zones was not solely determined by tidal height and topography but also by rainfall [25], surface roughness [27], vegetation density [23], and human activity.

4.2. Impacts of Flooding on Backscatter Characteristics. Aside from using tidal flooding and surface drainage pattern to describe mangrove species zonation, tidal flooding may have

influence on ALOS PALSAR polarimetric measurement on HH and HV. We have created three ROIs in Banyuasin (d1, d2, d3), Cilacap (k1, k2, k3), and Teluk Bintuni (q1, q2, q3) with multitemporal ALOS PALSAR polarimetric measurement on HH and HV. Multitemporal ALOS PALSAR polarimetric measurement suggests different tidal height, and our next discussions shall focus on the impact of those differences to various zones of mangrove in Banyuasin, Cilacap, and Teluk Bintuni. Each study area has unique characteristics of backscatter value on HH and HV that depend on wavelengths, polarization, incident angle, and temporal data [25], as well as environment (e.g., tidal height, topography, and landscape) and mangrove structure, and will be described exclusively in each section.

4.2.1. Case Study in Banyuasin South Sumatera. We used two ALOS PALSAR polarimetric measurements on HH and HV which covers mangrove forest at Banyuasin South Sumatera. The first acquisition date was on 10-05-2008 at 15:48:07.749, while the second acquisition date was on 25-06-2008 at 15:47:35.329. Each acquisition date has differences in tidal height, whereas tidal height on the first acquisition date is higher than that of the second. SRTM data of topography level in Banyuasin showed that most of the study area has high topography, with topography of less than 4 meters only covering 10% of total area.

Figure 5 shows the impact of tidal height on ALOS PALSAR polarimetric measurement on HH and HV based on profiling of ROI with length of 420 pixels. The number 0 (zero) on the axis “distance on pixel” serves as a starting point for water areas. The water area (distance on pixel 0–60 at d1) shows a majority of backscatter value of less than -20 dB on HH and HV, indicating the specular reflection of ALOS PALSAR radiation which produces small backscatter value. The open zone has different backscatter patterns between the two acquisition dates of 10-05-2008 and 25-06-2008, which might be caused by different tidal height. The measurement on 10-05-2008 shows lower tides, creating a nonflooding condition at the open zone. On the nonflooding areas, ALOS PALSAR penetrated the mangrove areas and dry surface so ALOS PALSAR radiation has multiple and double bounce reflection which produce backscatter value on HH and HV around -20 dB to -10 dB. Different conditions showed on

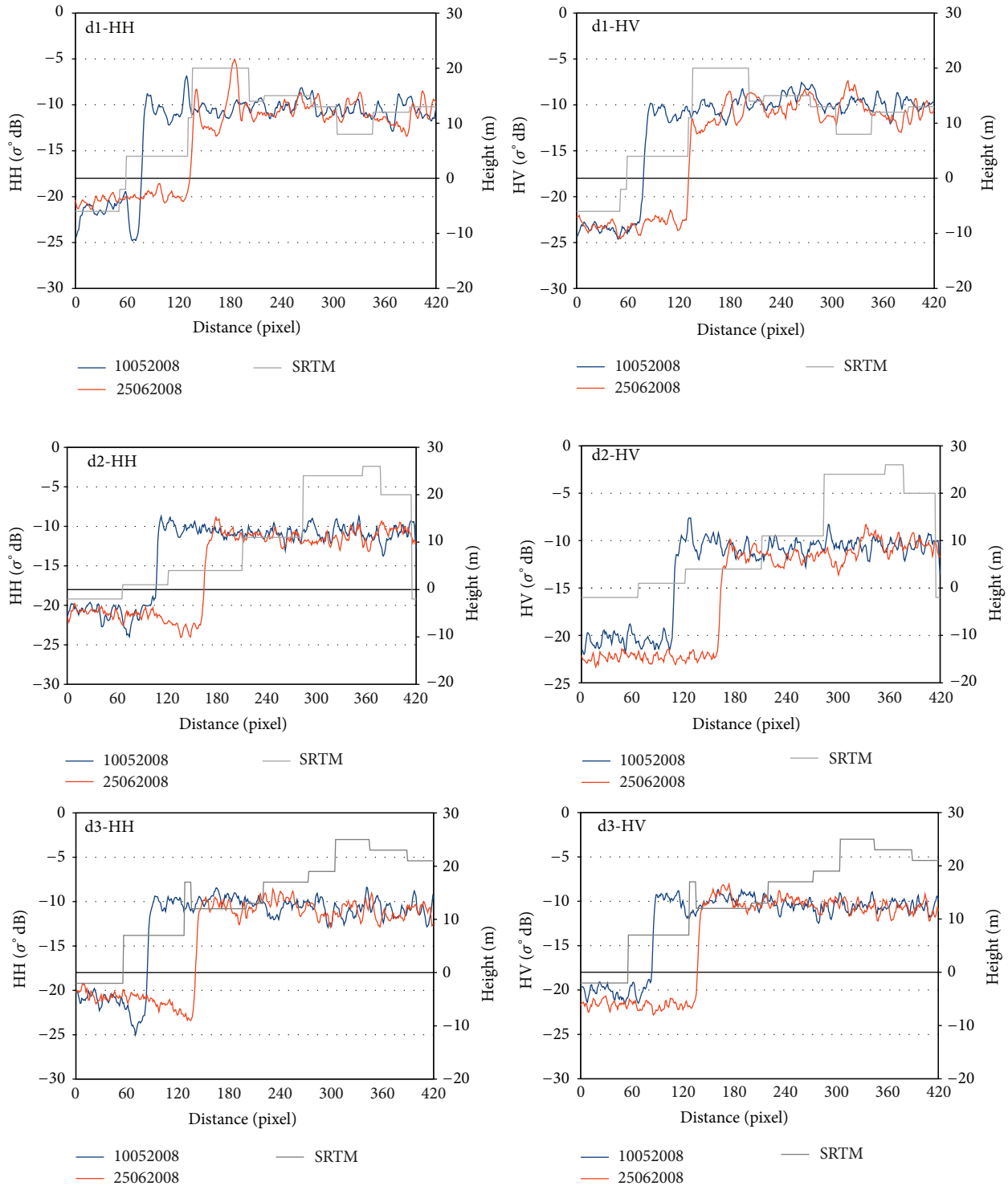


FIGURE 5: Impact of tidal height on ALOS PALSAR polarimetric measurement on HH and HV in Banyuasin, South Sumatera.

25-06-2008 when high tide occurred that high tide caused flooding of open zones, requiring ALOS PALSAR to penetrate more water on the underlying layer. In this situation, ALOS PALSAR radiation has specular reflection which produces backscatter value on HH and HV less on -20 dB. Meanwhile, the majority of area in the middle zone has backscatter value on HH and HV around -10 dB. This shows that on the

middle zone, ALOS PALSAR penetrates mangrove areas and dry surface so its radiation has multiple and double bounce reflection.

4.2.2. Case Study in Cilacap Central Java. We used three ALOS PALSAR polarimetric measurements on HH and HV that covered mangrove forest at Cilacap, Central Java. The

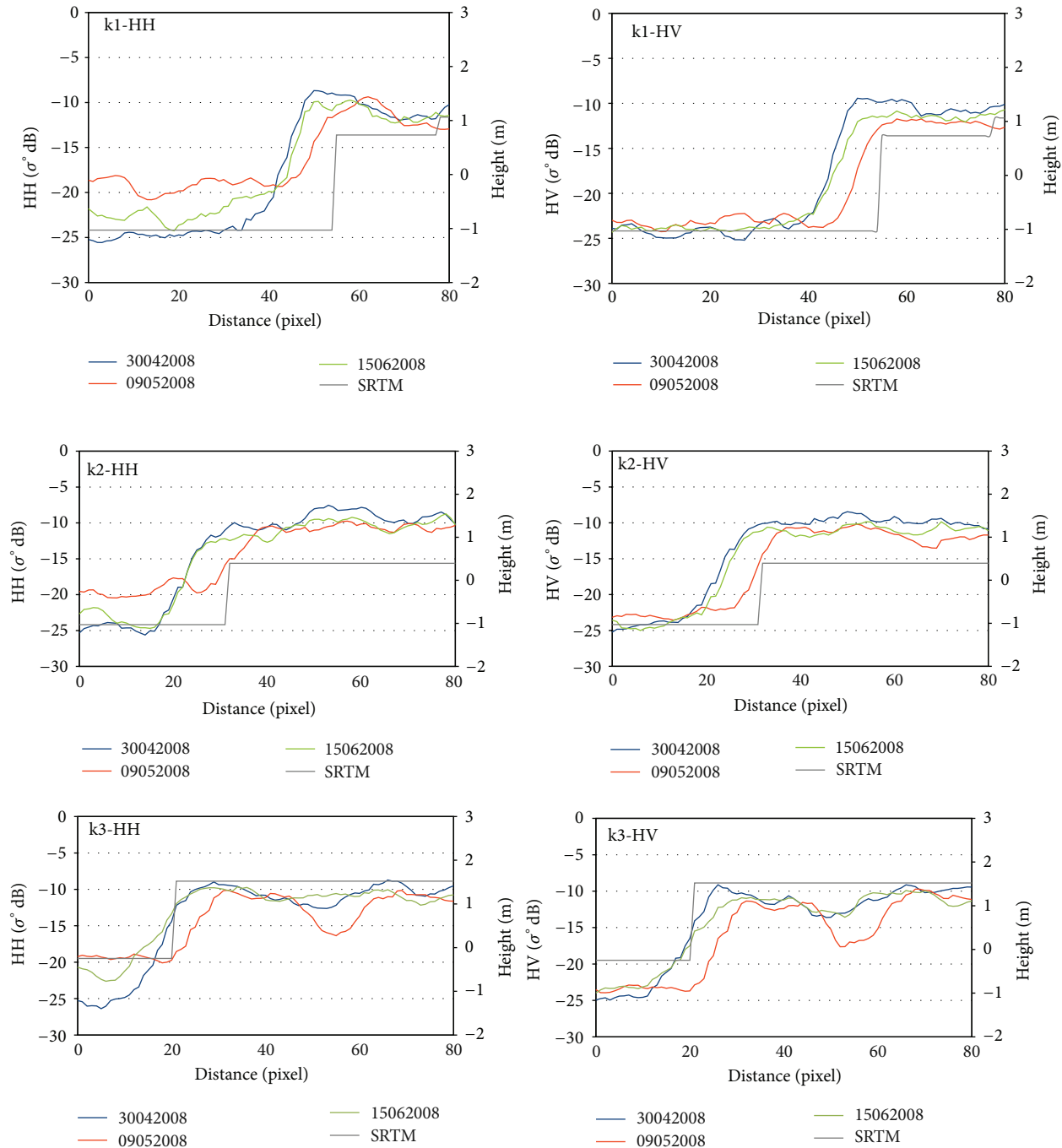


FIGURE 6: Impact of tidal height on ALOS PALSAR polarimetric measurement on HH and HV in Cilacap, Central Java.

first acquisition date was on 30-04-2008 at 15:33:49.697, the second on 09-05-2008 at 02:50:03.551, and the third on 15-06-2008 at 15:33:31.460. Each acquisition date has differences in tidal height. The measurement on acquisition date of 30-04-2008 at 15:33:49.697 showed tidal height around -0.4 meters, on 09-05-2008 at 02:50:03.551 tidal height around 1.0 meter, and on 09-05-2008 at 02:50:03.551 tidal height around -0.2 meter.

According to SRTM data, the level of topography on most of the mangrove zones in Cilacap is low and relatively flat, with 90% of the total areas having level of topography of less than 4 meters.

Figure 6 shows the impact of tidal height on ALOS PALSAR polarimetric measurement on HH and HV based on profiling as ROI with length of 80 pixels. The number 0 (zero) on the axis “distance on pixel” serves as a starting

point for water areas. The water area (distance on pixel 0–40 at k1) showed a majority of backscatter value around -20 dB on HH and around -25 dB on HV. The water area has a wide variety of backscatter value on HH due to the waves, since HH polarimetric is more sensitive to water waves compared to HV polarimetric. The open zone has different backscatter pattern between the three acquisition dates, and these differences are caused by difference in tidal height. The measurement on 15-06-2008 has the highest tides, suggesting flooding on the open zone, thus causing ALOS PALSAR radiation to have specular reflection which produce backscatter value of less than -20 dB on HH and less than -25 dB on HV. The condition is quite different from the measurement with acquisition date of 30-04-2008 when a nonflooding situation occurred at the open zone. The measurement on 30-04-2008 produces backscatter value around -20 to -10 dB on HH and around -25 to -10 dB on HV.

At the middle zone, the measurement with acquisition date of 15-06-2008 has lower backscatter value, especially on HV. A comparison with acquisition dates 30-04-2008 and 09-05-2008 shows a deviation of -1.6 dB. This is due to the characteristics of mangrove zones in Cilacap area with their relatively flat topography, allowing high tides to cause flooding and mud surface. The underlying layer of mud surfaces or more water content will produce lower backscatter value compared to underlying layer of dry soil or sand. This indicates that backscatter value derived on ALOS PALSAR measurement on the mangrove zone is affected by underlying layer (e.g., tidal height and topography) and mangrove structure (e.g., leaf, branches, and trunks).

4.2.3. Case Study in Teluk Bintuni Papua. We used two ALOS PALSAR polarimetric measurements on HH and HV that cover mangrove forest in Teluk Bintuni, Papua. The first acquisition date was on 27-06-2008 at 13:51:32.107 and the second on 27-09-2008 at 13:52:53.001. Each acquisition date has differences of tidal height. Acquisition date on 27-09-2008 at 13:52:53.001 has higher tidal height compared to that of acquisition date on 27-06-2008 at 13:51:32.107. Based on SRTM data, the level of topography of the mangrove zone in Teluk Bintuni, Papua, is mostly high, with level of topography of less than 4 meters only covering 8% of total areas.

Figure 7 shows the impact of tidal height on ALOS PALSAR polarimetric measurement on HH and HV based on profiling as ROI with length of 140 pixels. The number 0 (zero) on the axis “distance on pixel” serves as a starting point for water areas. The water area (distance on pixel 0–50 at q1) shows a majority of backscatter value of less than -20 dB on HH and less than -25 dB on HV. The profiles q1 and q3 for the open zone show different backscatter pattern between acquisition date on 27-06-2008 and 27-09-2008, due to different tidal height. Acquisition date on 27-09-2008 has the highest tidal height, suggesting flooding at the open zone, thus causing ALOS PALSAR radiation to have specular reflection which produce backscatter value of less than -20 dB on HH and less than -25 dB on HV. The condition was quite different from acquisition date 27-06-2008 when a nonflooding situation occurred at the open zone.

The acquisition date 27-06-2008 produce backscatter value around -20 to -10 dB on HH and around -25 to -10 dB on HV. On the middle zone, ALOS PALSAR penetrates mangrove areas and dry surface so ALOS PALSAR radiation has multiple and double bounce reflection.

4.3. Aboveground Biomass Estimation in Indonesia. Previous research on the characterization of mangrove forest in Indonesia [28] revealed the characteristics of mangrove forest based on ALOS PALSAR mosaics on the twenty sites of mangrove forest in Indonesia. Their sites covered a vast areas of mangrove forests, thus enabling them to describe all types of mangrove forest in overall Indonesia. The twenty sites of mangrove forest in Indonesia are (a) Langsa, Aceh, (b) Bengkalis, Riau, (c) Indragiri Hilir, Riau, (d) Banyuasin, South Sumatera, (e) Pontianak, West Kalimantan, (f) Kotabaru, South Kalimantan, (g) Kutai Kartanegara, East Kalimantan, (h) Berau, East Kalimantan, (i) Nunukan, East Kalimantan, (j) Subang, West Java, (k) Cilacap, Central Java, (l) Badung, Bali, (m) Bombana, Southeast Sulawesi, (n) Muna, Southeast Sulawesi, (o) Sorong, West Papua, (p) Teluk Bintuni, Papua, (q) Teluk Bintuni, Papua, (r) Waropen, Papua, (s) Asmat, Papua, and (t) Merauke Papua. Figures 8 and 9 show the characteristics of mean and standard deviation of backscatter coefficients on HH and HV for twenty Indonesian mangrove forests. From those figures, we can see that the mean for HH is around -10 dB to -7 dB, while the mean for HV is around -20 dB to -16 dB.

For estimations of AGB, some researchers [8, 10, 19] found empirical functions to estimate AGB, as derived from relationships between AGB measured on the ground sample plot and ALOS PALSAR polarimetric measurement, although using ALOS PALSAR for estimating AGB at regional level requires more detailed analysis [29]. In this study we have shown the impact of tidal height on ALOS PALSAR polarimetric measurement on HH and HV and we have estimated average AGB of mangrove forest at some area in Indonesia using algorithms 4, 5, and 6 and have the impact of tidal height and level of topography included in the calculation. Basically, the impact of tidal height on the open zones is quite significant, as can be seen from the variances of backscatter values. However, since the open zones only cover a diminutive area compared to the middle zones, this study shall focus on the latter. Based on the case of Cilacap, for the level of topography of less than 4 meters, with the size of mangrove zone impacted by tidal height which reached more than 90% of its total area, the backscatter value on HV has a deviation of -1.6 dB. However, to be able to calculate more accurately the deviation value caused by the impact of tidal height requires more time series ALOS PALSAR measurements and more tidal height data.

Table 2 shows the characteristics of level of topography, impact of tidal height on percentage of area, and the average of AGB estimation. The estimated averages of AGB in this study are within a reasonable range when compared with other studies which estimated an average of aboveground biomass in Aceh around 11.68 ton/ha, South Sumatera 43.72 ton/ha, and Riau 33.40 ton/ha [30], or in Malaysia around 2.98–378 ton/ha with an average of 99.40 ton/ha [19].

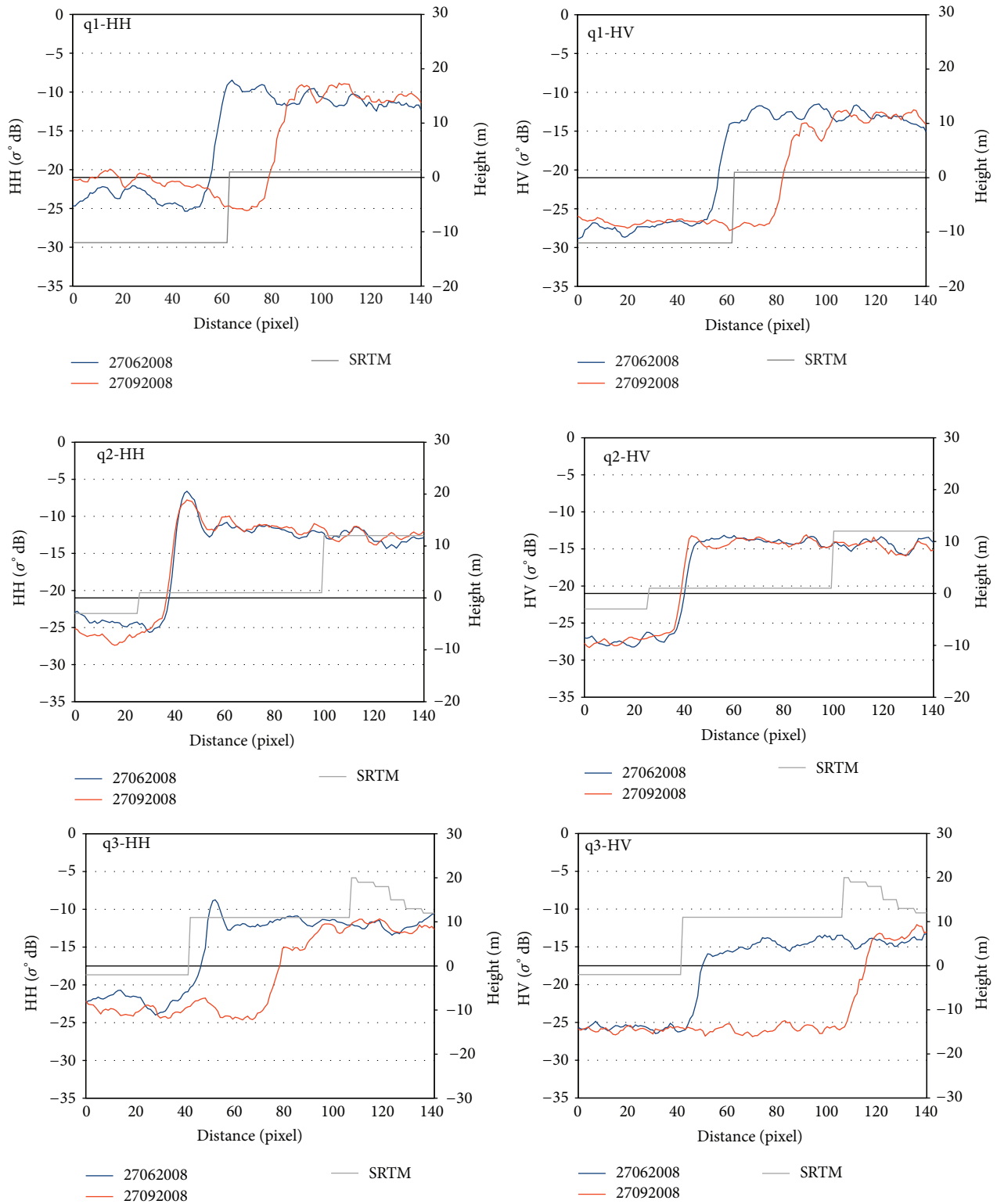


FIGURE 7: Impact of tidal height on ALOS PALSAR polarimetric measurement on HH and HV in Teluk Bintuni, Papua.

TABLE 2: Characteristics of topography, impact of tidal height on % area, and averages estimation of AGB mangroves forest in Indonesia.

Site	Location of mangrove zones	Average level of topography (meters)	Impact of tidal height (on % area)	Averages AGB estimation (ton/ha)
a	Langsa Aceh	2.2 ± 5.4	95	1.57–20.65
b	Bengkalis Riau	4.9 ± 1.9	40	26.08
c	Indragiri hilir Riau	6.8 ± 4.7	4	14.64
d	Banyuasin South Sumatera	16.8 ± 4.9	4	26.68
e	Pontianak West Kalimantan	10.2 ± 3.3	4	18.76
f	Kota Baru South Kalimantan	9.5 ± 5.9	6	62.57
g	Kutai Kartanegara East Kalimantan	9.6 ± 4.8	6	47.59
h	Berau East Kalimantan	15.0 ± 5.4	4	31.38
i	Nunukan East Kalimantan	14.5 ± 3.4	4	32.51
j	Subang West Java	3.0 ± 1.8	95	0.83–4.38
k	Cilacap Central Java	2.9 ± 2.1	90	1.70–19.36
l	Badung Bali	3.1 ± 2.0	73	3.47–85.56
m	Bombana South Sulawesi	8.8 ± 4.4	18	24.92
n	Muna South Sulawesi	10.6 ± 3.8	10	77.78
o	Sorong Papua	13.4 ± 4.5	5	85.76
p	Teluk Bintuni Papua	19.9 ± 11.2	6	17.79
q	Teluk Bintuni Papua	18.7 ± 8.3	4	23.30
r	Waropen Papua	19.3 ± 4.3	2	57.79
s	Asmat Papua	14.8 ± 3.5	2	23.30
t	Merauke Papua	11.7 ± 3.4	2	3.97

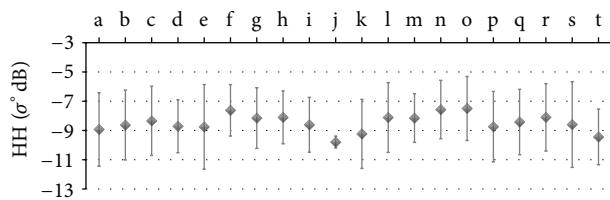


FIGURE 8: Mean and standard deviation of backscatter coefficients on HH.

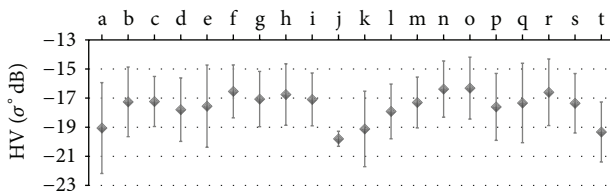


FIGURE 9: Mean and standard deviation of backscatter coefficients on HV.

5. Conclusion

This study showed a variety of tidal heights and levels of topography that cause distribution of flooding and nonflooding area at open and middle zones of mangrove forests. The open zones are highly impacted by tidal height, as evident by the flood that often occurs during high tides, whereas the middle zones experienced no significant impact of tidal height as evident by the occurrence of nonflooding area on most of its zone.

Based on ALOS PALSAR polarimetric measurement on HH and HV, flooding and nonflooding areas on the mangrove zones produce unique characteristics of backscatter value. These characteristics are the combined product of the effect of tidal height and the level of topography of the area. For the open zones, the backscatter during high tide in flooded areas showed values of less than -20 dB on HH and less than -25 dB on HV, except in Banyuasin where HV values are less than -20 dB. On the other hand, low tide and nonflooding produce a backscatter value around -20 to -10 dB on HH and around -25 to -10 dB on HV, except in Banyuasin with HV value from -20 to -10 dB.

At the middle zones, high topography and the variety of tidal height in Banyuasin and Teluk Bintuni produce similar backscatter value, unlike those of Cilacap with its low and flat topography that showed a 1.6 dB deviation of backscatter value on HV.

Differences in backscatter values of the open zones and deviation of backscatter values of the middle zone can be used to enhance and to improve algorithm model for estimating AGB mangrove forest based on ALOS PALSAR measurements, although it is agreed that the degree of accuracy of the estimation depends on the number of time series ALOS PALSAR measurements and tidal height data. Within the acknowledged limitation of this study, the different impact of tidal height on the backscatter value of HH and HV for different zone of mangrove forests has been demonstrated and used to estimate AGB mangrove forest in Indonesia. Based on ALOS PALSAR measurement that had included the impact of topography and tidal height, mangrove zones in Subang West Java have the smallest value of AGB with an

average value of 0.83–4.38 ton/ha, while Sorong Papua has the largest value of AGB with an average value of 85.76 ton/ha.

Conflict of Interests

The authors declare that there is no conflict of interests regarding the publication of this paper.

Acknowledgments

This study is carried out as a JAXA SAFE Project. The author would like to thank JAXA for their support.

References

- [1] P. B. Tomlinson, *The Botany of Mangroves*, Cambridge University Press, Cambridge, UK, 1986.
- [2] G. M. Wightman, "Mangroves of the northern territory," Northern Territory Botanical Bulletin no. 7, Conservation Commission of The Northern Territory, Palmerstone, Australia, 1989.
- [3] W. Giesen, S. Wulffraat, M. Zieren, and L. Scholten, *Mangrove Guidebook for South East Asia*, FAO, Wetlands International, Bangkok, Thailand, 2007.
- [4] C. Kuenzer, A. Bluemel, S. Gebhardt, T. V. Quoc, and S. Dech, "Remote sensing of mangrove ecosystems: a review," *Remote Sensing*, vol. 3, no. 5, pp. 878–928, 2011.
- [5] C. Nellemann, E. Corcoran, C. M. Duarte, L. Valdes, C. de Young, and L. Fonseca, *Blue Carbon, A Rapid Response Assessment*, United Nations Environment Programme, Arendal, Norway, 2009.
- [6] D. C. Donato, J. B. Kauffman, D. Murdiyarto, S. Kurnianto, M. Stidham, and M. Kanninen, "Mangroves among the most carbon-rich forests in the tropics," *Nature Geoscience*, vol. 4, no. 5, pp. 293–297, 2011.
- [7] Y. R. Noor, M. Khazali, and I. N. N. Suryadiputra, *Panduan Pengenaln Mangrove di Indonesia. PHKA/WI-IP*, Wetlands International, Bogor, Indonesia, 1999.
- [8] W. Takeuchi, D. V. Tien, V. T. Phuong, A. N. Van, and K. S. Oo, "Above ground biomass mapping of mangrove forest in Vietnam by ALOS PALSAR," in *Proceedings of the 3rd International Asia-Pacific Conference on Synthetic Aperture Radar (APSAR '11)*, pp. 1–3, IEEE, Seoul, South Korea, September 2011.
- [9] F. M. Henderson and A. J. Lewis, "Radar detection of wetland ecosystems: a review," *International Journal of Remote Sensing*, vol. 29, no. 20, pp. 5809–5835, 2008.
- [10] R. M. Lucas, A. L. Mitchell, A. Rosenqvist, C. Proisy, A. Melius, and C. Ticehurst, "The potential of L-band SAR for quantifying mangrove characteristics and change: case studies from the tropics," *Aquatic Conservation: Marine and Freshwater Ecosystems*, vol. 17, no. 3, pp. 245–264, 2007.
- [11] R. Tsolmon, R. Tateishi, and J. S. S. Tetuko, "A method to estimate forest biomass and its application to monitor Mongolian Taiga using JERS-1 SAR data," *International Journal of Remote Sensing*, vol. 23, no. 22, pp. 4971–4978, 2002.
- [12] R. M. Lucas, M. Moghaddam, and N. Cronin, "Microwave scattering from mixed-species forests, Queensland, Australia," *IEEE Transactions on Geoscience and Remote Sensing*, vol. 42, no. 10, pp. 2142–2159, 2004.
- [13] K. O. Pope, J. M. Rey-Benayas, and J. F. Paris, "Radar remote sensing of forest and wetland ecosystems in the Central American tropics," *Remote Sensing of Environment*, vol. 48, no. 2, pp. 205–219, 1994.
- [14] Y. Wang, L. L. Hess, S. Filoso, and J. M. Melack, "Understanding the radar backscattering from flooded and nonflooded Amazonian forests: results from canopy backscatter modeling," *Remote Sensing of Environment*, vol. 54, no. 3, pp. 324–332, 1995.
- [15] P. Townsend, "Relationships between forest structure and the detection of flood inundation in forested wetland using C-band SAR," *International Journal of Remote Sensing*, vol. 22, pp. 443–460, 2001.
- [16] P. A. Townsend, "Mapping seasonal flooding in forested wetlands using multi-temporal Radarsat SAR," *Photogrammetric Engineering and Remote Sensing*, vol. 67, no. 7, pp. 857–864, 2001.
- [17] C. Proisy, E. Mougin, F. Fromard, V. Trichon, and M. A. Karam, "On the influence of canopy structure on the radar backscattering of mangrove forests," *International Journal of Remote Sensing*, vol. 23, no. 20, pp. 4197–4210, 2002.
- [18] A. C. Morel, S. S. Saatchi, Y. Malhi et al., "Estimating above-ground biomass in forest and oil palm plantation in Sabah, Malaysian Borneo using ALOS PALSAR data," *Forest Ecology and Management*, vol. 262, no. 9, pp. 1786–1798, 2011.
- [19] O. Hamdan, H. Khali Aziz, and I. Mohd Hasmadi, "L-band ALOS PALSAR for biomass estimation of Matang Mangroves, Malaysia," *Remote Sensing of Environment*, vol. 155, pp. 69–78, 2014.
- [20] M. L. Imhoff, "A theoretical analysis of the effect of forest structure on synthetic aperture radar backscatter and the remote sensing of biomass," *IEEE Transactions on Geoscience and Remote Sensing*, vol. 33, no. 2, pp. 341–352, 1995.
- [21] M. Shimada, O. Isoguchi, T. Tadono, and K. Isono, "PALSAR radiometric and geometric calibration," *IEEE Transactions on Geoscience and Remote Sensing*, vol. 47, no. 12, pp. 3915–3932, 2009.
- [22] L. M. Varnell, D. A. Evans, and K. J. Havens, "A geomorphological model of intertidal cove marshes with application to wetlands management," *Ecological Engineering*, vol. 19, no. 5, pp. 339–347, 2003.
- [23] E. Wolanski, "Hydrodynamics of mangrove swamps and their coastal waters," *Hydrobiologia*, vol. 247, no. 1–3, pp. 141–161, 1992.
- [24] Y. Mazda, D. Kobashi, and S. Okada, "Tidal-scale hydrodynamics within mangrove swamps," *Wetlands Ecology and Management*, vol. 13, no. 6, pp. 647–655, 2005.
- [25] J. M. Knight, P. E. R. Dale, R. J. K. Dunn, G. J. Broadbent, and C. J. Lemckert, "Patterns of tidal flooding within a mangrove forest: coombabah Lake, Southeast Queensland, Australia," *Estuarine, Coastal and Shelf Science*, vol. 76, no. 3, pp. 580–593, 2008.
- [26] E. Rodríguez, C. S. Morris, J. E. Belz et al., "An Assessment of the SRTM Topographic Products," http://www2.jpl.nasa.gov/srtm/SRTM_D31639.pdf.
- [27] F. Darboux, P. Davy, C. Gascuel-Oudou, and C. Huang, "Evolution of soil surface roughness and flowpath connectivity in overland flow experiments," *Catena*, vol. 46, no. 2–3, pp. 125–139, 2002.
- [28] S. Darmawan, W. Takeuchi, Y. Vetrira, K. Wikantika, and D. Sari, "Characterization of mangrove forest types based on ALOS-PALSAR in overall Indonesian archipelago," *IOP Conference Series: Earth and Environmental Science*, vol. 20, Article ID 012051, 2014.

- [29] R. Lucas, J. Armston, R. Fairfax et al., "An evaluation of the ALOS PALSAR L-band backscatter—above ground biomass relationship Queensland, Australia: impacts of surface moisture condition and vegetation structure," *IEEE Journal of Selected Topics in Applied Earth Observations and Remote Sensing*, vol. 3, no. 4, pp. 576–593, 2010.
- [30] D. M. Yuwono, S. W. Wijaya, T. Hidayatullah, P. Meissarah, E. Prahasta, and I. Hayatiningsih, *Pemetaan Mangrove Sumatera, Provinsi Aceh, Sumatera Utara dan Riau*, Badan Informasi Geospasial (BIG), Bogor, Indonesia, 2013.

Research Article

Detecting the Depth of a Subsurface Brine Layer in Lop Nur Lake Basin Using Polarimetric L-Band SAR

Chang-An Liu,^{1,2} Huaze Gong,¹ Yun Shao,¹ and Bingyan Li³

¹*Institute of Remote Sensing and Digital Earth, Chinese Academy of Sciences, Datun Road, Beijing 100101, China*

²*University of Chinese Academy of Science, Beijing 100049, China*

³*China University of Geosciences Beijing 100083, China*

Correspondence should be addressed to Huaze Gong; gonghz@radi.ac.cn

Received 28 October 2014; Revised 15 January 2015; Accepted 5 February 2015

Academic Editor: Yoshio Yamaguchi

Copyright © 2015 Chang-An Liu et al. This is an open access article distributed under the Creative Commons Attribution License, which permits unrestricted use, distribution, and reproduction in any medium, provided the original work is properly cited.

Lop Nur once was a huge lake located in northwestern China. At present, there is no surface water in Lop Nur Lake basin and on SAR images it looks like an “Ear.” The objective of this paper is to retrieve the depth of subsurface brine layer in Lop Nur by copolarized phase difference of surface scattering. Based on field investigation and analysis of sample properties, a two-layer scattering structure was proposed with detailed explanations of scattering mechanisms. The relationship between copolarized phase difference and the brine layer depth in the region of Lop Nur were studied. The copolarized phase difference of surface scattering was extracted by model-based polarimetric decomposition method. A good linear correlation between measured subsurface brine layer depth and copolarized phase difference with R^2 reaching 0.82 was found. Furthermore, the subsurface brine layer depth of the entire lake area was analyzed. According to the retrieved maps, some interesting phenomena were found, and several hypotheses about the past water withdrawal process and the environmental evolution had been proposed to theoretically explain these phenomena. Based on the penetration capability of SAR the reconstruction of historical evolution process of Lop Nur will be an interesting topic for future research.

1. Introduction

Lop Nur was once an extensive lake located in the Xinjiang Uygur Autonomous Region in the eastern Tarim Basin, in northwestern China. Lop Nur is located in a typical arid region, which is highly sensitive to climate change, and its history of environmental changes is significant for understanding historic global climate change [1–3]. The Lop Nur basin was an important section of the ancient “Silk Road,” famous as the prosperous communication channel between Eastern and Western cultures. However, Lop Nur has completely dried up during the 20th century, leaving ear-shaped concentric strips (interchanging bright-grey appearance) visible in remote sensing images (Figure 1) [4–6]. Many assumptions have been made about its formation, but they remain to be proven by scientific evidence, and therefore its formation has remained a mystery [7]. It has been called the “Drought Pole” and the “Sea of Death” because of its extremely dry conditions and poor accessibility [6]. The lake

area may expand and shrink several times because of the periodic arrival of moist airflow or flooding. It serves as a region of salt and water accumulation in the Tarim Basin and is therefore rich in mineral salts with many salts at the surface and very low moisture content. With the penetration ability of synthetic aperture radar (SAR) signals and the arid environment of Lop Nur, it is believed that SAR can detect subsurface targets and reflect the information of the thickness of the dry soil layer [8].

One of the significant advantages of SAR is penetrating dry soil. In 1981, space shuttle Columbia installed an L-band HH polarization imaging radar system SIR-A and obtained many images. Scientists have made many valuable applications of the results. Most notably, McCauley of the United States Geological Survey found ancient river and human remains in the eastern Sahara desert under sand cover using SIR-A image analysis, which caused a sensation in the remote sensing and meteorological communities [9]. Blom found igneous dikes buried under up to 2 m of alluvium in

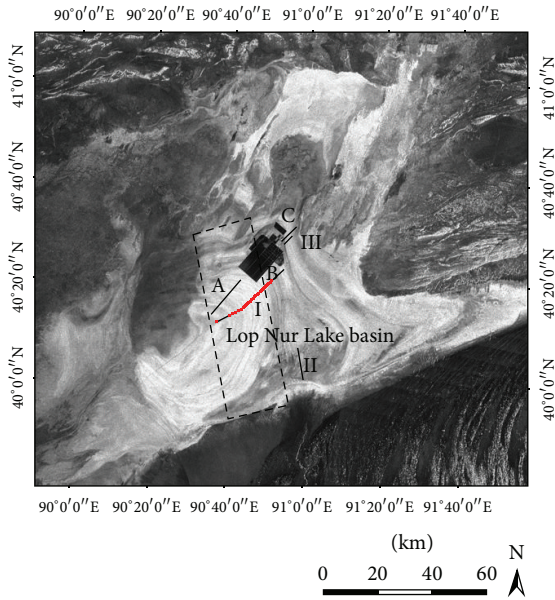


FIGURE 1: Field investigation routes and sampling site locations. A, B, and C are field routes in 2006, and I, II, and III are field routes in 2008. The dashed rectangle is the coverage of full-polarimetric SAR data used in the last part of this paper and the red dots are positions of sampling sites of 2013. There is a large salt pond in the middle of the image as a black square. ALOS-PALSAR image (HH polarization, ScanSAR mode) obtained on January 15, 2011, were used as base map.

the Mojave Desert of California detected by the SEASAT L-band (23.5-cm wavelength) SAR [10]. These findings suggest that subsurface features with potential tectonic or geomorphic significance may be revealed in other orbital radar images in semiarid terrains. Schaber et al. further studied the effects of physical factors that affect penetration and attenuation [11, 12] and found that the estimated penetration depth of L-band radar is approximately 1.5 m through sandy sediment in the southern desert of Egypt [13]. In addition, there are many scientists using SIR-B and SIR-C to study subsurface geological structures and radar penetration depth in desert areas [14–17].

In radar remote sensing, copolarized phase difference has a lot of physical meaning and special significance. Lasne et al. found that the copolarized phase difference has a good correlation with the depth of the dry sand layer [18]. This phase signature may be used as a new tool to map subsurface moisture in arid regions. In their study, a phase difference of 23° between the horizontal (HH) and vertical (VV) channels was clearly observed. It allows the detection of the wet paleosol down to a greater depth (5.2 m) than when only considering HH and HV amplitude signals (3.5 m). They performed several experiments and published many articles to validate their theory [19–23]. Lop Nur also has a two-layer soil structure area and therefore, based on the theory of Lasne et al., we will study the copolarized phase difference in the Lop Nur Lake Basin.

The theory of Lasne et al. is based on the field created by a wet paleosol layer, which is covered by a dry sand layer. The structure of their research objective is relatively

simple, while the structure and chemical composition of the soil layer in the Lop Nur region is more complex, with a rough rock shell on the top surface (Figure 2), and an aqueous saline soil layer in the subsurface. It therefore has complex scattering mechanisms that in this area not only include pure surface scattering, but also subsurface scattering with a complex signal propagation mechanism. To study and verify the applicability of the phase signature based inversion methods of soil thickness in the Lop Nur region, we applied the ALOS L-band full polarization data and the model-based polarization decomposition method to extract copolarized phase difference of the surface scattering. Based on the theory of Lasne et al. [18], we established an empirical relationship between the underground aquifer layer depth and the copolarized phase difference of the surface scattering. The objective of this study was to model and validate the capabilities of the L-band ALOS SAR to penetrate saline soil to detect the subsurface aquifer and to invert the underground aquifer layer depth and use the depth inversion map to study the distribution of the subsurface brine layer in the Lop Nur Lake region.

The study of the underground aquifer depth in the Lop Nur region is of profound environmental and climatic significance. It can reflect the distribution of the underground brine layer in the basin area, revealing subsurface structures below the rock shell, and contribute to the analysis of the cause of the large ear feature in the Lop Nur Lake. Furthermore, this work can provide reference information on past climate history. In addition, the proposed methodology can also be used for detecting underground aquifers in arid regions and the assessment of the stages of farmland soil drought.

First, the test site and field investigations are described. The principles and methods are introduced in the next section. The experimental inversion results of the subsurface brine layer depth of a line perpendicular to the stripes and the entire area are presented and discussed in section three. Finally, conclusions and future topics are presented at the end of this paper.

2. Materials and Methods

2.1. Test Site and Field Investigations

2.1.1. Test Site Description and Image Data. Lop Nur is located in the eastern Tarim Basin in the Xinjiang Uygur Autonomous Region, northwest China. Historically, the major rivers flowing into Lop Nur included the Tarim, Kongqi, and Qarqan rivers carrying large amounts of mineral salts. Because of its special geographical position in the Tarim Basin, mineral salts accumulated producing high salt concentrations in this area, in particular, rich potassium deposits. The basin is located at approximately 39.5° to 41.5° N and 88° to 92° E, and its lowest altitude is approximately 785 m [1, 2]. Because Lop Nur is located far from any ocean and the northeasterly winds prevail throughout the year, it is difficult for moist marine air masses to reach the area; thus, the climate is extremely arid. It is the most arid region of Eurasia, with less than 20 mm of annual precipitation and over 3000 mm of



FIGURE 2: Photos of surface conditions and field sampling.

evaporation. The former lake bed displays features of extreme salinification and severe wind erosion, and a large number of rimous salt crusts are found in the lake basin, resulting in an extremely coarse surface and fairly complex scattering mechanisms that developed during soil formation [8].

Optical and radar images of the Lop Nur Lake area show alternating light and dark textures, where the ring-shaped contour texture resembles a large ear, as shown in Figure 1. Lop Nur is a typical extreme arid region of western China and the world with its changes and history of drying recording the changes in the environment. Studies have shown that the Lop Nur ear feature is a true record of the demise of the lake, with implications for climate change from wet to dry. Remote sensing technology facilitates the spatial analysis of the distribution of the Lop Nur Lake sediments, which can help us analyze global climate change in arid regions.

Figure 1 shows the investigated routes and the distribution of the sampling points, and Figure 2 shows the surface condition and outdoor soil sample collection. HH polarization and ScanSAR mode ALOS-PALSAR data obtained on January 15, 2011, were used as the base map in Figure 1.

Because the radar signals at the L-band have relatively high penetration, this study uses mainly the ALOS-PALSAR remote sensing data to analyze the scattering characteristics of the Lop Nur Lake basin and to perform a phase signature study based on the Freeman target decomposition method. The L-band ALOS-PALSAR imagery for the Lop Nur area is the full polarimetric mode obtained on May 6, 2009, and the off-nadir angle is 23.1° . Images were reprojected onto the UTM/WGS84 coordinate system after basic radiation and geometric correction and processed with PolSARprov4.0 and ENVI 5.0 software.

2.1.2. Field Investigation and Sample Collection. To obtain detailed information on the composition and structure of the surface and subsurface features in the study area, the research group performed six scientific field investigations in Lop Nur, beginning in 2006. The field investigations and measurements define the existing knowledge and research results from Lop Nur and provide powerful data in support of the subsequent quantitative analysis of the scattering mechanisms.

We visited the ruins of the Loulan Kingdom and the Lop Nur Lake basin, where lacustrine deposits were sampled

along a 41 km profile at intervals of 2 km to the northeast of the Lop Nur Lake, as shown in Figure 1. Lacustrine samples from the surface and subsurface were collected at every sampling site. Twelve salt crystal and brine samples were also collected from certain sampling sites. The second field investigation was conducted in November 2008, when GPR (Ground Penetrating Radar) was first used to collect Lop Nur subsurface structural information. In November 2008 field investigation, the GPR detected a boundary between the dry upper layer and the wet lower layer at depth of about 50–55 cm, ranging from the centre to the edge. The measurements made by GPR have the same trend with L-band SAR. Another three field trips were completed in December 2008, April 2010, and November 2010 to determine the northern and western parts of the shoreline and to verify the existence of the shoreline of the East Lop Nur Lake, which has been buried by the lacustrine deposits of the West Lop Nur Lake.

The 2013 field experiments spanned from October 14 to November 3, for a period of 21 days, and this paper is based on this field investigation. The main work included radar remote sensing field sampling, surveying and sampling the OSL sample area, spectral measurement, and sampling. Among them, the radar remote sensing field sampling and spectral measurement expedition route was the same as the route in 2008. Field samples were collected from 43 locations with a total of 622 samples, including 224 large and small boxes for measuring ion content and moisture content, 114 boxes for laboratory measurement of dielectric properties, and 60 optical luminescence light specimens. Based on their sedimentary characteristics, six lacustrine deposit samples were collected for each sampling site from the surface to the base of each sampling pit at different depths and numbered as samples one through six. The depth of the pits ranged from 50 cm to 120 cm. The samples were kept fresh in sampling boxes and transported to the laboratory for analysis, including moisture testing, ion content (e.g., Na^+ , Ca^{2+} , K^+ , Cl^- , and SO_4^{2-}), particle size, pH, and the real (ϵ') and imaginary (ϵ'') parts of the dielectric constant.

2.2. Principles and Methods

2.2.1. Scattering Mechanisms and Phase Signature. Because of the extremely dry rough surface morphology of the Lop Nur

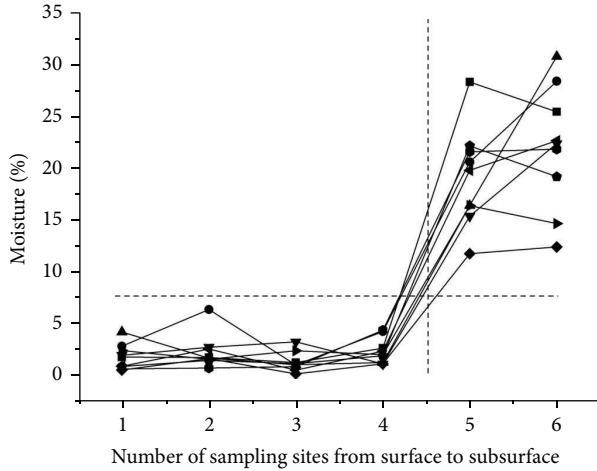


FIGURE 3: Moisture variation from surface to base of the lacustrine deposits at selected sampling sites. It can be seen that the moisture increased abruptly rather than gradually from the fourth sample (average depth of 40 cm) to the fifth sample (average depth of 50 cm) counting from surface to base in each sampling pit. The fourth and fifth samples were from different depths at different sites. The average moisture of the first four samples was approximately 2%, but the moisture of the fifth sample increased to 10% at least. The dash line in the figure stands for the significant difference.

area and the unique ability of SAR to penetrate in the arid region, the scattering mechanism in this area includes pure surface scattering and complex signal propagation mechanisms in subsurface structure. Based on the Lop Nur radar image features combined with field and laboratory measurement data, we conclude that there is a special subsurface layer in the Lop Nur Lake area with different dielectric properties from the other layers (wet and dry change interface). At present, the bed of the Lop Nur Lake is extremely flat and uniform, with endless dry salt crust in all directions. The upper layer of the salt crust is extremely dry with no water content, resulting in a very low complex dielectric constant (the dielectric constants of upper layer is very low, about $3-0.2j$ for C band and $3.5-1j$ for L band). However, with further digging into the lacustrine deposits, a moist layer was found beneath the upper dry layer on all sampling sites. Furthermore, at some sampling sites, brine was clearly visible and even gushed out. In general, brine is visible at depths of 50–60 cm. Figure 3 shows that the moisture increased abruptly from the fourth (average depth of 40 cm) to the fifth sample (average depth of 50 cm), counting from the surface to the base in each sampling pit. The locations of the fourth and fifth samples are not fixed, because every sample site has its specific subsurface condition. The average moisture of the first four samples was approximately 2%, but the moisture of the fifth sample increased to at least 10%. From the center to the edge of the lake, the variation of moisture in the lacustrine deposits at the same layer position is not obvious [6].

For scattering mechanisms, the SAR signal can penetrate the rough surface to detect subsurface targets because the top layer has lower dielectric properties, which indicates that the attenuation effect on the signal is weak. Typically,

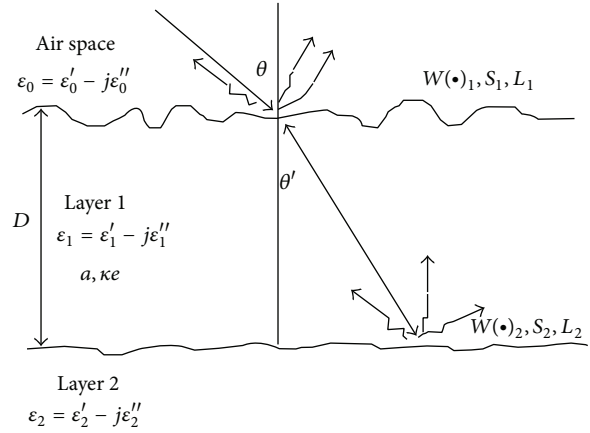


FIGURE 4: Two-layer structure and scattering mechanisms, where ϵ stands for complex dielectric constants, D is the thickness of layer 1, W represents Fourier transformation of surface correlation function, S and L are RMS height and correlation length, respectively, a is albedo, κe means extinction coefficient, and θ and θ' accounts for incidence and transmission angles.

the various effects of signal propagation process cannot be considered one by one. Based on the actual situation, the structure can be simplified by highlighting the main factors to take advantage of a simple model or the combination of models for quantitative characterization. In Figure 4, the Lop Nur subsurface structure is simplified into a two-layer medium layer. For the bottom layer, the water content is close to saturation, the dielectric properties are significant, and the signals cannot continue to spread. Therefore, we only consider the second layer and the parts above it as the main factors.

When the signal arrives at the top interface, strong surface scattering will occur because of the rough microtopography. Then, the transmission effect will allow a partial signal to propagate sequentially into layer 1, where absorption and volume scattering may attenuate the signal intensity. Here, to reduce the complexity of the modeling and to conduct validation combined with model-based polarimetric decomposition results, only the absorption effect is considered. After attenuation, the signal arrives at the bottom interface, where surface scattering occurs once more. Note that, in view of the simple sedimentary environment of Lop Nur, the roughness of the bottom interface is not severe. This assessment agrees with the GPR results, which show that the subsurface interface is much smoother. The signal will transmit continuously into the lower layer, but because of its notable dielectric properties, the imaginary part in particular, which accounts for the attenuation ability, has no strong backscattering intensity. In summary, only the surface scattering at the top and bottom interface and absorption attenuation are considered for the scattering mechanisms of Lop Nur [6]. Based on the measured parameters and the analysis described above, the two-layer structure was used in this study. The specific scattering mechanisms are shown in Figure 4.

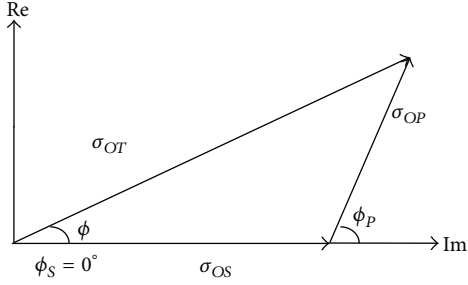


FIGURE 5: Total backscattered power σ_{OT} is represented as the vectorial sum of the upper layer surface σ_{OS} and wet subsurface σ_{OP} contributions.

Based on the theory of Lasne et al., this two-level structure with a dry upper soil layer and a subsurface brine layer will have a copolarized phase difference in the PolSAR images. Next, we will briefly introduce this theory.

The total complex backscattered signal SAR is the coherent sum of the contributions of the top S_S and bottom S_P surfaces, which can be written as

$$S_T = S_S + S_P, \quad (1)$$

with each term described by its amplitude σ_O and phase ϕ . Equation (1) can be represented as the sum of two vectors as shown in Figure 5 and we can set a phase origin so that the phase associated with the sand layer ϕ_S is zero. We can then express the HH and VV polarization as

$$\begin{aligned} \sigma_{OT}^{HH} \angle \phi_T^{HH} &= \sigma_{OS}^{HH} + \sigma_{OP}^{HH} \angle \phi_P^{HH}, \\ \sigma_{OT}^{VV} \angle \phi_T^{VV} &= \sigma_{OS}^{VV} + \sigma_{OP}^{VV} \angle \phi_P^{VV}. \end{aligned} \quad (2)$$

With some approximation, we can assume that the phase of HH and VV signals backscattered by the bottom interface is the same:

$$\phi_P^{HH} = \phi_P^{VV} = \phi_P. \quad (3)$$

The phase ϕ_P is only a function of the distance traveled by the incident wave through the sand layer of thickness D :

$$\phi_P = \Re \left[\frac{(D / \cos \theta')}{(\lambda / \sqrt{\epsilon'_1})} \right] * 2\pi \quad (4)$$

with $\Re[A/B]$ as the remainder of A divided by B .

Then, the phase of the total backscattered signal ϕ_T in Figure 5 can be expressed as

$$\phi_T = \arctan \left(\frac{\sigma_{OP} \sin(\phi_P)}{\sigma_{OS} + \sigma_{OP} \cos(\phi_P)} \right) \quad (5)$$

and we can obtain the phase difference between HH and VV signals as

$$\begin{aligned} \phi_{HH-VV} &= \phi_{T^{HH}} - \phi_{T^{VV}} \\ &= \arctan \left(\frac{\sigma_{OP^{HH}} \sin(\phi_P)}{\sigma_{OS^{HH}} + \sigma_{OP^{HH}} \cos(\phi_P)} \right) \\ &\quad - \arctan \left(\frac{\sigma_{OP^{VV}} \sin(\phi_P)}{\sigma_{OS^{VV}} + \sigma_{OP^{VV}} \cos(\phi_P)} \right). \end{aligned} \quad (6)$$

In [18] Lasne et al. found that the phase difference increases with respect to the thickness of the overlying sand. In the same article they used an analytical approach based on IEM, which was proposed by Fung [24, 25], that reproduced the phase difference between HH and VV signals as a function of the sand layer thickness. Using this analysis we discovered that our study area has similarities with theirs. In this paper, we will introduce this theory to the study of subsurface aquifers in the Lop Nur region.

The study area of Lasne et al. was a two-layered structure consisting of a layer of dry sand and a wet paleosol layer, which is a relatively simple structure. In their study area, relatively weak surface scattering will occur at the surface of the first layer of dry sand. Then, following attenuation some of the signals will arrive at the second wet-paleosol layer, and relatively strong surface scattering will occur at this layer there. As shown in Figure 4, when the SAR signals spread on to the surface in Lop Nur, the surface morphology is very rough at the interface of the first layer, and surface scattering will occur at the rough surface (including single and multiple scattering). Due to the low dielectric properties of layer 1 (very dry), part of the energy will spread into layer 1. In this process, we must take the attenuation effects into consideration. When the signals reach the interface between layers 2 and 1, there will be a surface-like scattering effect due to the differences of the dielectric properties between the two layers. The process and structure described above are suitable for the application of the theory of Lanse et al. However, because of the special structure and chemistry of the Lop Nur surface and subsurface soil, this area experiences surface, dihedral, and volume scattering. Therefore, we must use the model-based polarimetric decomposition method to calculate the copolarized phase difference corresponding to the surface scattering mechanism.

2.2.2. Model-Based Polarimetric Target Decomposition. There is a theoretical relationship between the copolarized phase difference of the surface scattering and the thickness of dry soil layer. In Lop Nur the two-layer scattering mechanism of the dry sediments is special and complex. This region has single and multiple scattering from the upper soil surface, surface scattering from the subsurface layer, and dihedral, volume, and other scattering mechanisms. To extract the phase difference of the contributions from surface scattering we applied the classical Freeman-Durden decomposition method. The Freeman-Durden decomposition is a technique for fitting a physically based, three-component scattering mechanism model to the polarimetric SAR observations,

without using any ground truth measurements [26, 27]. It decomposes the targets covariance matrix into three components by meeting the reflection symmetry. The advantage of the Freeman-Durden decomposition is that it is based on the physical mechanisms of radar backscattering, and its results are easy to correspond to typical scattering mechanisms. It is very practical for application.

We take the phase information into consideration in the dihedral and surface scattering mechanisms. The total covariance matrix C is expressed as the sum of the three matrices accounting for the contributions of volume C_{VOL} , surface C_{ODD} , and dihedral C_{DBL} , as proposed by Freeman and Durden:

$$C = C_{\text{VOL}} + C_{\text{ODD}} + C_{\text{DBL}}. \quad (7)$$

The first component of the Freeman-Durden decomposition consists of a first-order Bragg surface scatterer modeling slightly rough surface scattering in which the cross-polarized component is negligible. In this paper a phase difference between the HH and VV backscatter terms is included to model any propagation delay for H and V from radar to scatter and back [28, 29]. The scattering S matrix for a Bragg surface has the form

$$\begin{aligned} S &= \begin{bmatrix} S_{hh} & 0 \\ 0 & S_{vv} \end{bmatrix}, \\ S_{hh} &= R_{\text{H}} e^{j\varphi_h}, \\ S_{vv} &= R_{\text{V}} e^{j\varphi_v}, \\ R_{\text{H}} &= \frac{\cos \theta - \sqrt{\varepsilon_r - \sin^2 \theta}}{\cos \theta + \sqrt{\varepsilon_r - \sin^2 \theta}}, \\ R_{\text{V}} &= \frac{(\varepsilon_r - 1) \{ \sin^2 \theta - \varepsilon_r (1 + \sin^2 \theta) \}}{(\varepsilon_r \cos \theta + \sqrt{\varepsilon_r - \sin^2 \theta})^2}, \end{aligned} \quad (8)$$

where θ is the local incidence angle and ε_r is the relative dielectric constant of the surface.

This scattering matrix yields a surface scattering covariance matrix C_{ODD} as

$$C_{\text{ODD}} = F_{\text{S}} \cdot \begin{bmatrix} |\beta|^2 & 0 & \beta \\ 0 & 0 & 0 \\ \beta^* & 0 & 1 \end{bmatrix}, \quad (9)$$

where F_{S} corresponds to the contribution of the single-bounce scattering to the $|S_{\text{VV}}|^2$ component, with $F_{\text{S}} = |R_{\text{V}}|^2$ and $\beta = (R_{\text{H}}/R_{\text{V}}) e^{j\Delta\varphi_{vh}}$.

The double-bounce scattering component is modeled by scattering from a dihedral corner reflector, such as ground-tree trunk backscatter, where the reflector surfaces can be made of different dielectric materials. The vertical trunk surface has reflection coefficients R_{TH} and R_{TV} for horizontal and vertical polarizations, respectively. The horizontal

ground surface has Fresnel reflection coefficients R_{GH} and R_{GV} . The model can be made more general by incorporating propagation factors $e^{2j\gamma_h}$ and $e^{2j\gamma_v}$, where the complex coefficients γ_h and γ_v represent any propagation attenuation and phase change effects. The covariance matrix for double-bounce scattering is therefore

$$C_{\text{DBL}} = F_{\text{D}} \cdot \begin{bmatrix} |\alpha|^2 & 0 & \alpha \\ 0 & 0 & 0 \\ \alpha^* & 0 & 1 \end{bmatrix}, \quad (10)$$

where F_{D} corresponds to the contribution of the double-bounce scattering to the $|S_{\text{VV}}|^2$ component, with

$$F_{\text{D}} = |R_{\text{TV}} R_{\text{GV}}|^2, \quad \alpha = \frac{R_{\text{TH}} R_{\text{GH}}}{R_{\text{TV}} R_{\text{GV}}} e^{2j(\gamma_h - \gamma_v)}. \quad (11)$$

The volume scattering from a forest canopy is modeled as the contribution from a cloud of randomly oriented cylinder-like scatters. We then assume that the scatterers are randomly oriented about the radar look direction with an angle ϕ from the vertical polarization direction and the probability density function of the orientation angle is assumed to be uniform ($p(\phi) = 1/2\pi$). The volume scattering averaged covariance matrix C_{VOL} is thus given by

$$C_{\text{VOL}} = \frac{F_{\text{V}}}{8} \begin{bmatrix} 3 & 0 & 1 \\ 0 & 2 & 0 \\ 1 & 0 & 3 \end{bmatrix}, \quad (12)$$

where F_{V} corresponds to the contribution of the volume scattering component.

For all of these backscatter components, it is assumed that the backscatter is reciprocal. It has also been shown that the like- and cross-polarized returns are uncorrelated. Taking into account the previous considerations, the main elements of the C_{int} matrix can be decomposed as

$$\begin{aligned} C_{11} &= F_{\text{S}} |\beta|^2 + F_{\text{D}} |\alpha|^2 + \frac{3F_{\text{V}}}{8}, \\ C_{13} &= F_{\text{S}} \beta + F_{\text{D}} \alpha + \frac{F_{\text{V}}}{8}, \\ C_{22} &= \frac{2F_{\text{V}}}{8}, \\ C_{33} &= F_{\text{S}} + F_{\text{D}} + \frac{3F_{\text{V}}}{8}. \end{aligned} \quad (13)$$

Now we can estimate the volume scatter contribution directly. The volume contribution can then be subtracted from C_{11} , C_{13} , and C_{33} terms, leaving three equations and four unknowns. Based on van Zyl [30], we then interpret whether double-bounce or surface scatter is the dominant contribution in the residual, based on the sign of the real part of $S_{\text{HH}} S_{\text{VV}}^*$. If $\text{Re}(S_{\text{HH}} S_{\text{VV}}^*)$ is positive, we deduce that surface scatter is dominant and fix $\alpha = -1$. If $\text{Re}(S_{\text{HH}} S_{\text{VV}}^*)$ is negative, we know that double-bounce scatter is dominant and fix $\beta = 1$. Then F_{S} , F_{D} and β or α can be estimated

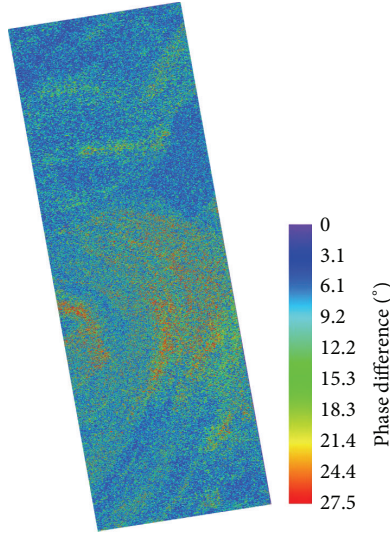


FIGURE 6: The distribution of the copolarized phase difference from the surface scattering contribution throughout the Lop Nur Lake area got from Freeman-Durden model-based decomposition method. In the lake area we can see significant changes in copolarized phase difference.

from the residual radar measurements. In most of our area the $\text{Re}(S_{\text{HH}}S_{\text{VV}}^*)$ is positive, which indicates that the dominant contribution is surface scatter. We can therefore calculate out $|\beta|$ and $\Delta_{\psi_{\text{vh}}}^s$. Then, the copolarized phase difference of the surface scattering mechanism can be expressed as

$$\phi_{\text{HH-VV}} = \Delta_{\psi_{\text{vh}}}^s. \quad (14)$$

3. Results and Discussion

To retrieve the brine layer depth, the copolarized phase difference from the surface scattering contribution in Lop Nur must be calculated first. Because of the special structure and chemistry of the Lop Nur surface and subsurface soil, there are several different scattering mechanisms. To extract and calculate the surface scattering mechanism and the corresponding copolarized phase difference, we used a physically based polarization decomposition method. In recent years, scattering model-based polarization decomposition methods have gained more attention, because we can establish a correspondence between its decomposition results and the specific scattering mechanism. It is also very easy to understand and apply.

We calculated the copolarized phase difference information of the Lop Nur Lake basin using the Freeman-Durden decomposition as described in Section 2.2.2. The phase difference is due to the two-layer structure of the Lop Nur Lake basin. Figure 6 shows the distribution of the copolarized phase difference from the surface scattering contribution throughout the Lop Nur Lake area. We can see significant changes in the copolarized phase difference in the lake area, which is also distributed in a ring shape in the ancient lake in the Lop Nur region.

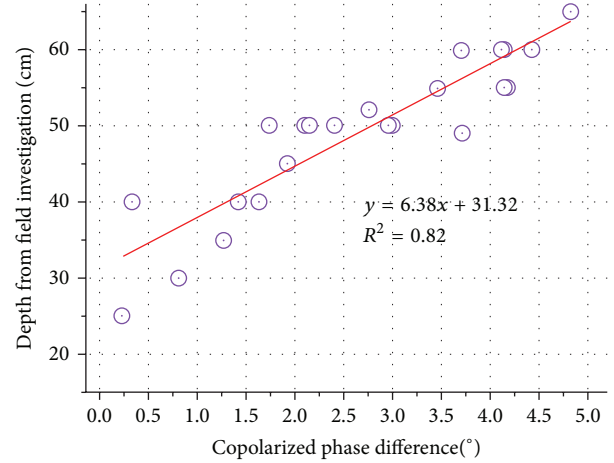


FIGURE 7: Comparison between $\phi_{\text{HH-VV}}$ from the surface scattering contribution using Freeman model-based decomposition and the measured depth results got from the field investigation. One scene of ALOS-PALSAR polarimetric data (L-band, quad-polarization, 23.9° incidence angles for 6 May 2009) was used, with RMSE, R^2 , and linear fitting formula shown. The solid line in diagram accounts for the linear fitting line.

Based on the research of Lasne et al., in areas that have a two-layer structure (a layer of wet soil covered by a dry sandy layer), there is a high correlation between the depth of the subsurface dielectric layer and the copolarized phase difference. Within a certain range of the depth distribution of the dry-upper layer, the copolarized phase difference increases with the depth of the subsurface wet layer. The Lop Nur Lake basin also has a two-layer scattering structure. There is a significant change in the dielectric properties of soil under the dry soil layer with a thickness of less than a meter, which indicates that it has a wet-dry change interface. To study the relationship between the copolarized phase difference due to the surface scattering and the depth of the brine layer in the Lop Nur region, we carried out a detailed field survey in 2013. A total of 32 sampling points were obtained from the lake region. The positions of the sampling points are marked out with red dots in Figure 1. Figure 7 shows the linear fit of the results between the copolarized phase difference and the brine layer depth at the same sampling points. One image of the ALOS-PALSAR polarimetric data (L-band, quad-polarization, 23.9° incidence angle for May 6, 2009) was used. We found that the copolarized phase difference has a good correlation with the subsurface brine layer depth, with a RMSE value and R^2 of 4.1 cm and 0.82, respectively.

Based on the relationship established in Figure 7 and using the extracted copolarized phase difference from the model-based Freeman-Durden decomposition in the Lop Nur region, we calculated the brine layer depth for a line perpendicular to the stripes. The inversion results are shown in Figure 8. The ROIs (regions of interest) were selected perpendicular to the stripes and were evenly distributed along the center to the shore of the lake. We can see significant fluctuations of the subsurface brine layer depth along the

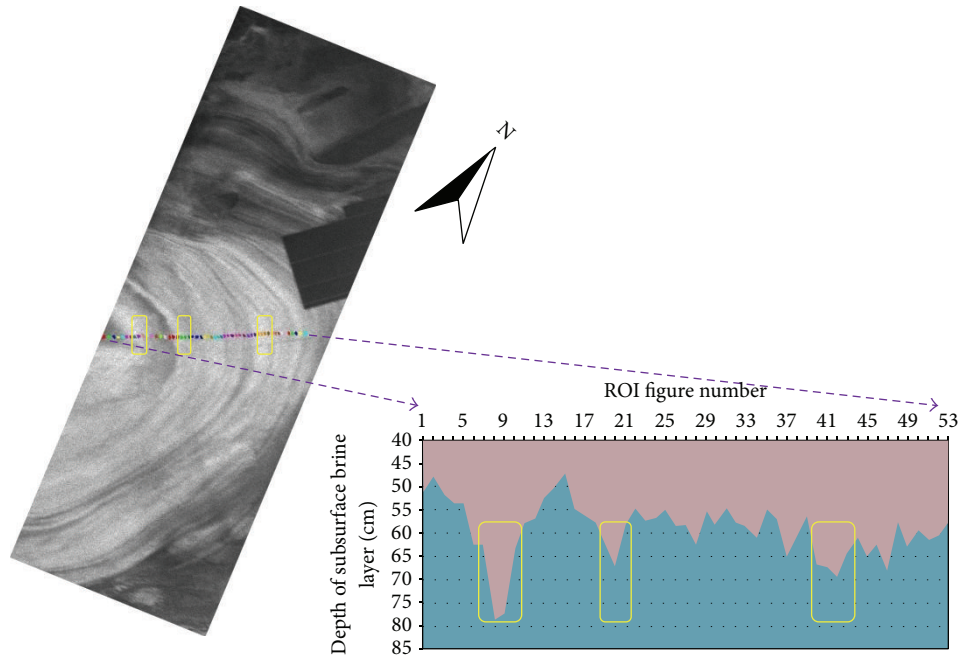


FIGURE 8: The distribution of retrieved subsurface brine layer depth from the heart to the shore of the lake. To get the depth line 53 ROIs (regions of interest) were selected. The base map is HV polarization L-band ALOS image. Significant fluctuations of the subsurface brine layer depth along the center to the shore of the lake can be seen. Three anomaly areas of the depth profile are marked out by yellow boxes.

heart to the shore of the lake. In general, the subsurface brine layer depth increases from the center to the shore of the lake, which is in line with the general evolution of the lake retreat progress. However, Figure 8 shows three anomaly areas of the subsurface brine layer depth profile, indicated by the yellow boxes. If the water withdrawal process is continuous, then the extracted depth profile of the brine layer should have a continuous trend, and the anomaly areas in the figure will not appear.

After the drying-up process, the morphological traces of the Lop Nur Lake are the combined result of the chemical deposition of the upper surface and the invasion of the underground brine water deposition. First, it is needed to introduce the evolution of the surface salt crust. During the early lake retreat, the remaining water forms the prototype of the surface salt crust over a short time period. Then, the upper surface becomes dryer, and the brine water invades the upper layer by soil capillarity action crystallized in the near-surface. Next, the underground brine rises to the subsurface and experiences crystallization. However, because of the pressure of the upper layer, the position of the brine water crystallization is continuously reducing. When it reaches a certain depth, the pressure of the upper layer and the force from the brine water crystallization will level off and will not have much impact on the upper and lower soil structure. This will increase the level of the horizontal pressure force and will ultimately form a dense layer, with an effect of holding the water below it, and finally the subsurface will have a distinct interface between wet and dry. Moreover, the formation of the ring textures of the lake should be analyzed, which are traces of its retreat. The bright stripes of the SAR image were

formed during relatively dry periods. During this time very little water flowed into the lake and it retreated very quickly. The brine salt precipitation in the surface and underground has a joint effect on the formation of the bright stripes. The dark stripes formed during a sudden increase of the surface water in the lake, as it partially submerged the bright striped-regions that had formed before, namely, in the middle of a large lake retreat cycle; due to a temporary abrupt climate change, there will be several reciprocate cycles. Such sudden flood or climate events do not last long in general, after which there will be a rapid withdrawal process. Because of the short duration, it is assumed some of the salts up to the wet and dry interface will be lost. However, the dense interface between the wet and dry will not be affected. Therefore, the pressure from the layer above the wet and dry interface will be reduced, because of the force of the underground brine water, and the wet and dry interface in subsurface will be further uplifted. After this process a dark stripe will form, and its boundary between the bright stripes is clearly visible.

The satellite images of the Lop Nur area display light and dark, approximately concentric, ring structures. These ring stripes vary in width and are sometimes stacked. The “big ear,” composed of the ring textures, is the most striking feature of Lop Nur in remote sensing images. Different interpretations have been provided for the ring-shaped stripes. Although the arguments differ, it is clear that each ring texture is the mark of a Lop Nur Lake border during a climate period. The depth of subsurface brine layer throughout the Lop Nur Lake area is shown in Figure 9. The depth map of the subsurface brine layer also has ring structures, which is consistent with common knowledge.

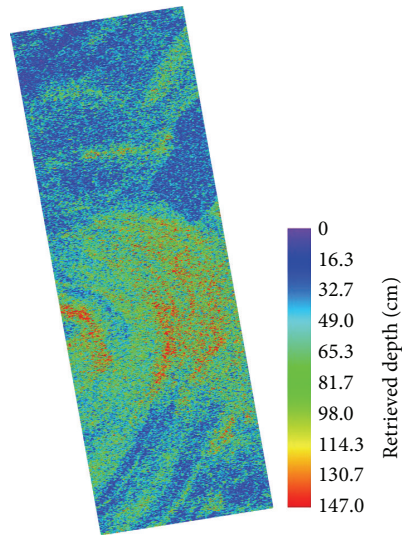


FIGURE 9: The distribution of the depth of brine layer throughout the Lop Nur lake area by phase inversion method. In the lake area we can see significant changes in depth. In this figure we used the mean filter with 11×11 windows size to highlight the differences.

However, using the inversion map, we found that the depth of the subsurface brine layer is different during each ring stripe (deeper in the northeast). This is contrary to the normal process of lakeshore retreat. In the general process of lakeshore retreat, the different parts of one ring stripe are formed during the same period and may have the same subsurface brine layer depth. This phenomenon may be due to the effects of wind stress, as proposed by Wang et al. [31], because there was a prevailing perennial northeasterly wind in the Lop Nur region. Particularly in the spring, the wind speed is up to 40 m/s. Thus, during the process of lake retreat, the northeast of Lop Nur was at times covered with water. Because of the strong evaporation in this part, the surface out of the water will have collected more crystallized salt. After the lake dried up, the expansion of the upper surface salinity became stronger and it was difficult for the underground brine water to rise and crystallize, which led to the increased depth of the subsurface wet and dry interface. The ring stripes in the southwest direction of the lake had not been out of the water and would experience the normal crystallization process. Therefore, the distribution of the depth of the subsurface brine layer is comparatively lower in the southwest direction of the lake. This phenomenon is particularly evident in Figure 9.

4. Conclusions

Based on field investigations and laboratory analysis, we studied the dielectric properties and structure of the soil layers in the Lop Nur lake region, where a subsurface wet and dry interface layer is thought to exist with different dielectric properties. We then simplified the structure of the soil in the Lop Nur Lake into a two-layer medium. The material composition of first layer is not uniform, with some

pure salt and some saline mixed layers. The water content of first layer is very low. The second layer and the soil beneath it is very wet and contains a lot of salt, and the SAR signals cannot penetrate and continue to spread. Based on the theory proposed by Lasne et al. and the two-layer structure established above, we studied the relationship between the copolarized phase difference of the surface scattering and the dry medium thickness in the Lop Nur Lake region. The surface scattering copolarized phase difference is extracted using the model-based polarimetric decomposition method. By analyzing 25 field sampling points and the extracted surface scattering copolarized phase difference, we found a good linear correlation between the measured subsurface brine layer depth and the copolarized phase difference with an R^2 of 0.82. This indicates that the inversion of the subsurface brine layer depth by copolarized phase difference is feasible.

On this basis, we calculated the copolarized phase difference and the subsurface brine layer depth of the entire lake area. By analyzing the distribution of the subsurface brine layer depth, we found that the dielectric layer depth has an overall trend with an increasing subsurface brine layer depth from the center to the shore of the lake, which is consistent with the known pattern of lake retreat. We found three anomaly areas on the profile of the subsurface brine layer depth, shown as a sudden deepening of the dielectric layer depth. This may be mainly due to a sudden injection of large amounts of flood water, which indicates a temporary regression of the drying-up cycle of the lake. The regression may also be caused by certain climate processes and will cause large structural changes to the soil layer in the Lop Nur Lake area. We have discussed the mechanism of this process in detail. Using the estimated depth map we found that the depth of the subsurface brine layer is different during each ring stripe (deeper in the northeast). This is contrary to the normal process of lakeshore retreat. Based on the hypothesis of the evolution of the surface salt crust and the wind stress factors, we are able to explain this phenomenon theoretically.

Remote sensing has advantages for studying geological phenomena on a large spatial scale. We have confirmed that the surface patterns and specific subsurface parameters, such as brine layer depth, are correlated with the process of paleoclimatic changes. Given the paleoclimatic significance of the Lop Nur Lake and based on the capability of SAR to detect structural and chemical parameters in subsurface layers, the reconstruction of historical evolution process of Lop Nur will be an interesting topic for future research.

Conflict of Interests

The authors declare that there is no conflict of interests.

Acknowledgments

The authors would like to express their sincere appreciation of the anonymous reviewers. This work was funded by the CAS Knowledge Innovation Program (KZCX2-EW-320), the National Natural Science Foundation of China (41431174,

61471358, 41201346, U1303285, 41301394, and 41301464), the fund of the State Key Laboratory of Remote Sensing Science (Y1Y00201KZ), IRSA/CAS (Y3SG1900CX, Y1S01200CX), and Industry Application Projects (05-Y30B02-9001-13/15-03).

References

- [1] X. C. Xia, *Lop Nur in China*, Science Press, Beijing, China, 2007.
- [2] H. Y. Lü, X. C. Xia, J. Q. Liu et al., "A preliminary study of chronology for a newly-discovered ancient city and five archaeological sites in Lop Nur, China," *Chinese Science Bulletin*, vol. 55, no. 1, pp. 63–71, 2010.
- [3] Y. Shao, H. Gong, Z. Gao, L. Liu, T. Zhang, and L. Li, "SAR data for subsurface saline lacustrine deposits detection and primary interpretation on the evolution of the vanished Lop Nur Lake," *Canadian Journal of Remote Sensing*, vol. 38, no. 3, pp. 267–280, 2012.
- [4] B. Li, L. Ma, P. Jiang et al., "High precision topographic data on Lop Nur basin's Lake "great Ear" and the timing of its becoming a dry salt lake," *Chinese Science Bulletin*, vol. 53, no. 6, pp. 905–914, 2008.
- [5] F. Wang, C. Ma, X. Xia, Q. Cao, and Q. Zhu, "Environmental evolution in Lop Nur since late pleistocene and its response to the global changes," *Quaternary Sciences*, vol. 28, pp. 150–153, 2008.
- [6] H. Z. Gong, *SAR remote sensing research on subsurface targets detection and environmental evolution in Lop Nur palaeo-lacustrine basin [Ph.D. thesis]*, Institute of Remote Sensing Applications, Chinese Academy of Sciences, Beijing, China, 2010.
- [7] H. Gong, Y. Shao, T. Zhang, L. Liu, and Z. Gao, "Scattering mechanisms for the 'ear' feature of lop nur lake basin," *Remote Sensing*, vol. 6, no. 5, pp. 4546–4562, 2014.
- [8] Z. Gao, H. Gong, X. Zhou, Y. Shao, M. Yuan, and L. Wang, "Study on the polarimetric characteristics of the Lop Nur arid area using PolSAR data," *Journal of Applied Remote Sensing*, vol. 8, no. 1, Article ID 083681, 2014.
- [9] J. F. McCauley, "Subsurface valleys and geoarcheology of the eastern Sahara revealed by shuttle radar," *Science*, vol. 218, no. 4576, pp. 1004–1020, 1982.
- [10] R. G. Blom, R. E. Crippen, and C. Elachi, "Detection of subsurface features in SEASAT radar images of Means Valley, Mojave Desert, California," *Geology*, vol. 12, no. 6, pp. 346–349, 1984.
- [11] G. G. Schaber, "SAR studies in the Yuma Desert, Arizona: sand penetration, geology, and the detection of military ordnance debris," *Remote Sensing of Environment*, vol. 67, no. 3, pp. 320–347, 1999.
- [12] G. G. Schaber and C. S. Breed, "The importance of SAR wavelength in penetrating blow sand in Northern Arizona," *Remote Sensing of Environment*, vol. 69, no. 2, pp. 87–104, 1999.
- [13] G. G. Schaber, J. F. McCauley, C. S. Breed, and G. R. Olhoef, "Shuttle imaging radar: physical controls on signal penetration and subsurface scattering in the eastern sahara," *IEEE Transactions on Geoscience and Remote Sensing*, vol. 24, no. 4, pp. 603–623, 1986.
- [14] G. L. Berlin, M. A. Tarabzouni, A. H. Al-Naser, K. M. Sheikho, and R. W. Larson, "SIR-B subsurface imaging of a sand-buried landscape: Al Labbah Plateau, Saudi Arabia," *IEEE Transactions on Geoscience and Remote Sensing*, vol. GE-24, no. 4, pp. 595–602, 1986.
- [15] M. G. Abdelsalam and R. J. Stern, "Mapping Precambrian structures in the Sahara desert with SIR-C/X-SAR radar: the Neoproterozoic Kerfah suture, NE Sudan," *Journal of Geophysical Research E: Planets*, vol. 101, no. 10, pp. 23063–23076, 1996.
- [16] A. E. Dabbagh, K. G. Al-Hinai, and M. A. Khan, "Detection of sand-covered geologic features in the Arabian Peninsula using SIR-C/X-SAR data," *Remote Sensing of Environment*, vol. 59, no. 2, pp. 375–382, 1997.
- [17] G. G. Schaber, J. F. McCauley, and C. S. Breed, "The use of multifrequency and polarimetric SIR-C/X-SAR data in geologic studies of Bir Safsaf, Egypt," *Remote Sensing of Environment*, vol. 59, no. 2, pp. 337–363, 1997.
- [18] Y. Lasne, P. Paillou, T. August-Bernex, G. Ruffié, and G. Grandjean, "A phase signature for detecting wet subsurface structures using polarimetric L-band SAR," *IEEE Transactions on Geoscience and Remote Sensing*, vol. 42, no. 8, pp. 1683–1694, 2004.
- [19] P. Paillou, G. Grandjean, N. Baghdadi, E. Heggy, T. August-Bernex, and J. Achache, "Subsurface imaging in south-central Egypt using low-frequency radar: bir Safsaf revisited," *IEEE Transactions on Geoscience and Remote Sensing*, vol. 41, no. 7, pp. 1672–1684, 2003.
- [20] G. Grandjean, P. Paillou, P. Dubois-Fernandez, T. August-Bernex, N. N. Baghdadi, and J. Achache, "Subsurface structures detection by combining L-band polarimetric SAR and GPR data: example of the pyla dune (France)," *IEEE Transactions on Geoscience and Remote Sensing*, vol. 39, no. 6, pp. 1245–1258, 2001.
- [21] P. Paillou and T. August-Bernex, "Sub-surface imaging by combining airborne SAR and GPR: application to water detection in arid zones," in *Proceedings of the International Geoscience and Remote Sensing Symposium (IGARRS '01)*, vol. 3, pp. 1384–1386, July 2001.
- [22] P. Paillou, G. Grandjean, J.-M. Malézieux et al., "Performances of ground penetrating radars in arid volcanic regions: consequences for Mars subsurface exploration," *Geophysical Research Letters*, vol. 28, no. 5, pp. 911–914, 2001.
- [23] Y. Lasne, P. Paillou, G. Ruffié, and M. Crapeau, "Effect of multiple scattering on the phase signature of wet subsurface structures: applications to polarimetric L- and C-band SAR," *IEEE Transactions on Geoscience and Remote Sensing*, vol. 43, no. 8, pp. 1716–1726, 2005.
- [24] A. K. Fung, Z. Li, and K. S. Chen, "Backscattering from a randomly rough dielectric surface," *IEEE Transactions on Geoscience and Remote Sensing*, vol. 30, no. 2, pp. 356–369, 1992.
- [25] A. K. Fung, *Microwave Scattering and Emission Models and Their Applications*, Artech House, Norwood, Mass, USA, 1994.
- [26] S. R. Cloude and E. Pettier, "A review of target decomposition theorems in radar polarimetry," *IEEE Transactions on Geoscience and Remote Sensing*, vol. 34, no. 2, pp. 498–518, 1996.
- [27] A. Freeman and S. L. Durden, "A three-component scattering model for polarimetric SAR data," *IEEE Transactions on Geoscience and Remote Sensing*, vol. 36, no. 3, pp. 963–973, 1998.
- [28] A. Freeman, "Fitting a two-component scattering model to polarimetric SAR data from forests," *IEEE Transactions on Geoscience and Remote Sensing*, vol. 45, no. 8, pp. 2583–2592, 2007.
- [29] J. D. Ballester-Berman and J. M. Lopez-Sanchez, "Applying the Freeman-Durden decomposition concept to polarimetric SAR interferometry," *IEEE Transactions on Geoscience and Remote Sensing*, vol. 48, no. 1, pp. 466–479, 2010.

- [30] J. J. van Zyl, "Unsupervised classification of scattering behavior using radar polarimetry data," *IEEE Transactions on Geoscience and Remote Sensing*, vol. 27, no. 1, pp. 36–45, 1989.
- [31] L. Wang, H. Gong, Y. Shao, and B. Li, "Analysis of elevation discrepancies along the Lop Nur ear-shaped stripes observed using GLAS and DGPS data," *International Journal of Remote Sensing*, vol. 35, no. 4, pp. 1466–1480, 2014.

Research Article

Comparisons of Circular Transmit and Linear Receive Compact Polarimetric SAR Features for Oil Slicks Discrimination

Yu Li,^{1,2} Hui Lin,^{1,2,3} Yuanzhi Zhang,² and Jie Chen⁴

¹*Institute of Space and Earth Information Science, The Chinese University of Hong Kong, Shatin, New Territories, Hong Kong*

²*Shenzhen Research Institute, The Chinese University of Hong Kong, Shenzhen 518057, China*

³*Key Laboratory of Poyang Lake Wetland and Watershed Research, Ministry of Education, Jiangxi Normal University, Nanchang 330022, China*

⁴*School of Electronics and Information Engineering, Beihang University, Beijing 100037, China*

Correspondence should be addressed to Hui Lin; huilin@cuhk.edu.hk

Received 26 December 2014; Revised 8 April 2015; Accepted 15 April 2015

Academic Editor: Chengkuo Lee

Copyright © 2015 Yu Li et al. This is an open access article distributed under the Creative Commons Attribution License, which permits unrestricted use, distribution, and reproduction in any medium, provided the original work is properly cited.

Compact polarimetric (CP) synthetic aperture radar (SAR) has proven its potential in distinguishing oil slicks and look-alikes. Polarimetric information can be retrieved directly from scattering vector or from reconstructed pseudo-Quad-Pol covariance matrix of CP SAR data. In this paper, we analysed features from Circular Transmit and Linear Receive (CTLR) CP SAR data that are derived by taking both of these two methods. *K*-means clustering followed by accuracy assessment was also implemented for performance evaluation. Through experiments that were conducted based on L-band UAVSAR fully polarimetric data, it was found that optimum extraction methods varied for different features. The histogram analysis and segmentation results also demonstrated the comparable performance of CP SAR features in distinguishing different damping properties within oil slicks. This study proposed a framework of statistically analyzing polarimetric SAR (Pol-SAR) features and provided guidelines for determining optimum feature extraction methods from CP SAR data and for marine oil-spills detection and classification.

1. Introduction

As one of the major marine disasters, oil-spill pollution largely threatens the marine environment. Early warning of oil-spills by remote sensing is very crucial for the pollution evaluation, control, and clean-up operations. Synthetic aperture radar has been widely used in marine applications for its all-day, all-night, and weather-independent capabilities [1]. It has become a cost-effective way to monitor oil pollution in large areas [2]. SAR images of oil slicks have been captured by a variety of SAR sensors, from previous SIR-C, ERS-1/2, ENVISAT, ALOS-1, and RADARSAT-1 to current RADARSAT-2 and TerraSAR-X [3–5]. There are also some operational oil-spill monitoring systems, such as CleanSeaNet satellite monitoring service developed by European Maritime Safety Agency (EMSA), ISTOP (Integrated Satellite Tracking of Pollution) operated by Canadian Ice Service, and semiautomatic SAR oil-spill detection system developed by Kongsberg Satellite Services, Norway [6].

Currently a major difficulty for marine oil slicks detection is the discrimination between mineral oil and its look-alikes (physical or chemical phenomena which cause dark area in SAR images similarly to mineral oil slicks). As compared with single polarimetric SAR, fully polarimetric (FP) SAR has much stronger target classification capability of distinguishing mineral oil and look-alikes [7, 8]. However, FP SAR mode has only half the swath-width due to doubled pulse repetition frequency (PRF) and requires much higher data rate compared with single polarimetric SAR [9]. To overcome this difficulty, compact polarimetric (CP) SAR modes are proposed. CP SAR modes could acquire part of the polarimetric information at reduced PRF and data rate while maintaining the same swath-width as single polarimetric SAR or double the swath-width at the same PRF as fully polarimetric SAR [10]. As a result, CP SAR modes are suitable for the task of broad-area marine surveillance.

Previously there were several studies conducted on CP SAR based marine applications: Shirvany et al. studied ship

and oil-spill detection based on degree of polarization derived from dual and CTLR compact polarimetric SAR data [11]. Xie et al. investigated maritime applications based on H-decomposition on compact and Dual-Pol SAR data [12]. Collins et al. proposed an empirical model to estimate N in variance of incidence angles by fitting the observed data with negative exponent function for the reconstruction of pseudo-Quad-Pol SAR data from CP SAR data and used it for ships detection [13]. Li et al. improved Souyris' iterative reconstruction algorithm to derive pseudo-Quad-Pol covariance matrix from CP SAR images of sea surface that is covered by oil slicks [10]. Yin et al. proposed three novel CTLR CP SAR based parameters that are suitable for maritime target detection based on Bragg scattering model and tested their capabilities in oil-spill classification [14]. Salberg et al. utilized the structure of CTLR CP SAR mode to derive features and evaluated their performance in oil-spills detection and suppression of look-alikes [2]. Nunziata et al. proposed and tested several new features that can be derived from CTLR CP SAR data and proved their capabilities in distinguishing slick-free, weak damping slick-covered, and mineral oil-covered sea surfaces [15].

Among all the CP SAR modes, CTLR (also known as hybrid) compact polarimetric SAR mode has the advantages of invariance with the target orientation, stability to the affection of Faraday's rotation [16], and comparable robustness to the affection of systematic errors such as noise and crosstalk [17]. Working in CTLR CP SAR mode, as a small, low mass synthetic aperture radar that flew on the Indian Space Research Organization's Chandrayaan-1 mission, Mini-SAR aims to study the crater deposits in the permanently dark areas of the lunar poles from lunar orbit [18]. Currently and in the near future there are and will be several spaceborne SAR sensors that are equipped with this mode, including RADAR Imaging Satellite (RISAT) by India Space Agency, ALOS-2 by Japanese Space Agency (JAXA), SAOCOM of Argentina, and RADARSAT Constellation Missions (RCM) by Canada Space Agency.

In order to take advantage of CP SAR data, generally two strategies have been taken by previous studies. One is to reconstruct pseudo-Quad-Pol SAR matrix from CP SAR data and then conduct Quad-Pol feature analysis [19, 20]. The other is directly extracting features from scattering matrix or Stokes vectors of CP SAR data. Recently the latter method is relatively more frequently used [2, 11, 14, 15] while there are also some studies on the improvement of CP SAR reconstruction algorithms for marine applications [10, 13].

The advantage of analyzing CP SAR data based on Quad-pol reconstruction is that all current polarimetric SAR features can then be directly calculated from pseudo-Quad-Pol SAR data. However, since CP SAR has insufficient data dimension compared with Quad-Pol SAR mode, the reconstruction algorithms inevitably rely on assumptions of relationships between different polarimetric channels, which may lead to biased estimation. Extracting Pol-SAR features directly from CP SAR features provides another way to utilize CP SAR data, which can avoid errors to be introduced during the process of reconstruction. Since the data of CP SAR modes has different form and physical meanings compared

with those in Quad-Pol SAR mode, features extraction algorithms should be adjusted according to their special configuration.

In this paper, we will focus on the evaluation of CP SAR features extracted by using both of these different strategies. Several often used Pol-SAR features that can be derived from both Quad-Pol and CTLR modes will be reviewed and considered in the experiment. Parameters such as normalized difference between the means and relative difference were used to quantitatively analyse statistical behaviour of these Pol-SAR features. Then K -means clustering was implemented to demonstrate the performance of oil slicks segmentation, followed by classification accuracy assessment based on overall accuracy and Kappa coefficient.

2. Polarimetric SAR Features

In this section, the signal model of fully and CTLR CP SAR mode will be briefly introduced, and then different strategies that take advantage of CP SAR data will be reviewed.

2.1. Basic Representation of SAR Polarimetry. Fully polarimetric SAR systems could obtain the scattering matrix \mathbf{S} of the observed target, which describes the relationship of Jones vectors between the scattered and incident electromagnetic field, in the backscattered coordinate system:

$$\mathbf{E}^S = \frac{e^{-jkr}}{r} \mathbf{S} \mathbf{E}^i, \quad (1)$$

where k is the wavenumber of the EM wave, r is the distance, and the 2×2 scattering matrix \mathbf{S} on the traditional linearly horizontal (h) and vertical (v) bases can be described by

$$\mathbf{S} = \begin{pmatrix} S_{hh} & S_{hv} \\ S_{vh} & S_{vv} \end{pmatrix}, \quad (2)$$

where the subscript of S_{ij} describes the transmitted and received polarization, respectively.

For the monostatic case, the reciprocity usually holds, which means that the two cross-polarized terms are identical; that is, $S_{hv} = S_{vh}$. And when the reciprocal property is held, the scattering vector \vec{k} can be defined as

$$\vec{k}_{3B} = [S_{hh}, \sqrt{2}S_{hv}, S_{vv}]^T. \quad (3)$$

Based on \vec{k}_{3B} the covariance matrix of fully polarimetric SAR data can be derived by

$$\mathbf{C} = \vec{k}_{3B} \vec{k}_{3B}^{*T} = \begin{bmatrix} |S_{hh}|^2 & \sqrt{2}S_{hh}S_{hv}^* & S_{hh}S_{vv}^* \\ \sqrt{2}S_{hv}S_{hh}^* & 2|S_{hv}|^2 & \sqrt{2}S_{hv}S_{vv}^* \\ S_{vv}S_{hh}^* & \sqrt{2}S_{vv}S_{hv}^* & |S_{vv}|^2 \end{bmatrix}. \quad (4)$$

2.2. CTLR Compact Polarimetric SAR Data. In the CTLR CP SAR mode, the radar transmits circularly polarized signal and linearly receives both horizontal and vertical polarizations simultaneously. The 2D measurement vector \vec{K} is

the projection of the full backscattering matrix on the transmit polarization state, and in CTLR mode it can be defined as [1]

$$\vec{K} = (E_H \ E_V)^T, \quad (5)$$

where $E_H = (S_{HH} - jS_{HV})/\sqrt{2}$ and $E_V = (S_{HV} - jS_{VV})/\sqrt{2}$ and S_{XY} is the component of the scattering matrix of target, with X denoting the received wave polarization and Y indicating the transmitted wave polarization.

The covariance matrix of compact polarimetric SAR modes, which is derived from their scattering vector, can be defined by [1]

$$C_{CP} = 2 \langle \vec{K}_{CP} \vec{K}_{CP}^* \rangle, \quad (6)$$

where the superscript “*” denotes the transpose conjugate and $\langle A \rangle$ denotes the spatial average of A over a window size, for instance, 5×5 . In this paper, the multilook complex Quad-Pol SAR data was used to simulate the covariance matrix of CTLR CP SAR mode:

$$C_{CTLR} = \frac{1}{2} \begin{bmatrix} \langle S_{HH}^2 \rangle + \langle S_{HV}^2 \rangle + j \langle S_{HH} S_{HV}^* \rangle - j \langle S_{HH}^* S_{HV} \rangle & \langle S_{HH}^* S_{HV} \rangle - j \langle S_{HV}^2 \rangle + j \langle S_{HH} S_{VV}^* \rangle + \langle S_{HV} S_{VV} \rangle \\ \langle S_{HH} S_{HV}^* \rangle - j \langle S_{HV}^2 \rangle + j \langle S_{HH} S_{VV}^* \rangle + \langle S_{HV} S_{VV}^* \rangle & \langle S_{HV}^2 \rangle + \langle S_{VV}^2 \rangle + j \langle S_{HV} S_{VV}^* \rangle - j \langle S_{HV}^* S_{VV} \rangle \end{bmatrix}. \quad (7)$$

2.3. Feature Extraction from Quad-Pol and Reconstructed Pseudo-Quad-Pol SAR Data. In order to extract Pol-SAR features from CP SAR data through reconstruction of pseudo-Quad-Pol data, we employed the iterative algorithm proposed in Dubois-Fernandez et al. [19]. The algorithm is based on the hypotheses that Pol-SAR data of different channels are related and also it assumes that reciprocity and reflection symmetry of geophysical SAR data are held. The algorithm can be basically divided into three steps, namely, initialization, iteration, and reconstruction. The output of CP SAR reconstruction algorithm is pseudo-Quad-Pol covariance matrix. Please note that elements in C_{Rec} are estimated values, through the reconstruction algorithm:

$$C_{Rec} = \begin{pmatrix} \langle S_{HH} S_{HH}^* \rangle & 0 & \langle S_{HH} S_{VV}^* \rangle \\ 0 & 2 \langle S_{HV} S_{HV}^* \rangle & 0 \\ \langle S_{VV} S_{HH}^* \rangle & 0 & \langle S_{VV} S_{VV}^* \rangle \end{pmatrix}. \quad (8)$$

Then the following Pol-SAR features can be extracted from the reconstructed Quad-Pol covariance matrix C_{Rec} the same as those from Quad-Pol SAR data. The only difference between features extracted from original and reconstructed Quad-Pol covariance matrices is that for the reconstructed Quad-Pol data, multilook cross products between co- and cross-polarimetric channels are assumed to be zero, such as $\langle S_{HH} S_{VV}^* \rangle$. This approximation can be made on scattering coefficients of distributed targets.

(1) VV^2 . The power information of SAR data has been widely used for target detection and classification since the very beginning of marine SAR applications. Generally speaking, VV^2 is more suitable for oil-spills detection for its high SNR and sensitivity to sea surface roughness while HV^2 is more suitable for tasks such as ships detection, for its sensitivity to scattered signal from vertical structures. So, in the analysis of this paper, VV^2 is considered.

(2) *Standard Deviation of Copolarized Phase Difference*. It was a large breakthrough to realize that phase information within coherence polarimetric SAR data can be used to

boost the discrimination between mineral oil and look-alikes. Migliaccio et al. used copolarized phase difference (CPD) to characterize the scattering behavior of oil-spills and biogenic look-alikes [4]. It was discovered that, for sea surface covered by mineral oil, larger CPD standard deviation could be observed while for biogenic slicks a lower CPD standard deviation similar to that of clean sea surface is obtained. From Quad-Pol SAR data, CPD can be derived by

$$CPD = \arg(S_{HH}) - \arg(S_{VV}) = \arg(S_{HH} S_{VV}^*). \quad (9)$$

(3) *Correlation Coefficient*. Correlation coefficient reflects the averaged phase difference between scattering coefficients in HH and VV channels [2]:

$$Corr = \frac{\text{Re} \langle S_{HH} S_{VV}^* \rangle}{\sqrt{\langle |S_{HH}|^2 \rangle \langle |S_{VV}|^2 \rangle}}. \quad (10)$$

For clean sea surface where Bragg scattering is dominant, S_{HH} and S_{VV} are highly correlated, so $Corr$ is close to 1, while for mineral oil-covered area where strong damping property is held, S_{HH} and S_{VV} are uncorrelated; then $Corr$ is expected to be much lower.

(4) *Conformity Coefficient*. Conformity coefficient was used for the study of marine oil slicks detection from CTLR compact polarimetric SAR data [21]. By assuming the reflection symmetry, it can be also derived from Quad-pol SAR data by [21]

$$Conf \cong \frac{2(\text{Re}(S_{HH} S_{VV}^*) - |S_{HV}|^2)}{(|S_{HH}|^2 + 2|S_{HV}|^2 + |S_{VV}|^2)}. \quad (11)$$

It has been proved that for ocean Bragg scattering, S_{HV} is small, CPD is close to zero, and real part of S_{HH} and S_{VV} cross products is larger than $|S_{HV}|^2$; as a result $Conf$ is positive,

while for non-Bragg scattering the situation is reverse: Conf is negative.

(5) *Coherency Coefficient*. The magnitude of the coherency coefficient is useful for oil-spills classification [2]. It can be derived from coherency matrix of Quad-Pol SAR data:

$$\text{Coh} = \frac{|T_{12}|}{\sqrt{T_{11}T_{22}}}, \quad (12)$$

where

$$T = kk^*T \quad (13)$$

and k is the Pauli vector:

$$k = \frac{1}{\sqrt{2}} [S_{HH} + S_{VV} \quad S_{HH} - S_{VV} \quad 2S_{HV}]^T. \quad (14)$$

(6) *Entropy*. The polarimetric scattering property of targets can be described by their polarimetric entropy, which is derived from eigenvalue analysis on the coherency matrix [22]. Entropy describes the randomness of the scattering mechanism of ground target. For clean and biogenic slicks covered sea surface, Bragg scattering mechanism is dominant, so low scattering entropy is expected. While for sea surface that is covered by mineral oil, the proportion of volume scattering increases, and the entropy becomes much higher. Polarimetric entropy can be derived from the coherency matrix of Quad-Pol SAR data by [22]

$$H = \sum_{i=1}^3 -P_i \log_3 P_i, \quad (15)$$

where

$$P_i = \frac{\lambda_i}{\sum_j \lambda_j} \quad (16)$$

and λ_i ($i = 1, 2, 3$) is the eigenvalue of coherency matrix T .

2.4. Feature Extraction Directly from CTLR Compact Polarimetric SAR Data. Based on slightly modified definitions and some assumptions, the corresponding Pol-SAR features in Section 2.3 can also be extracted directly from scattering coefficient and coherency matrix of CTLR CP SAR data.

(1) $|E_V|^2$ (*Corresponding to VV^2 in Quad-Pol Mode*). Due to the Bragg scattering mechanism, in SAR images of sea surface cross-polarized term is usually much larger than copolarized terms, so E_H and E_V in CTLR mode are comparable to S_{HH} and S_{VV} in Quad-Pol SAR mode. In this study we chose $|E_V|^2$ as the corresponding feature to VV^2 .

(2) *Standard Deviation of Copolarized Phase Difference (CPD)*. CPD can be approximately estimated from covariance matrix of CTLR CP SAR data by

$$\phi_{\text{CPD}} = \arg \{-iE_H E_V^*\}. \quad (17)$$

Then its standard deviation within a certain spatial window can be computed.

(3) *Correlation Coefficient*. Following the same rationale as feature 1, correlation coefficient in CTLR CP SAR mode can be defined as

$$\text{Corr} = \frac{\text{Re} \{-i \langle E_H E_V^* \rangle\}}{\sqrt{\langle |E_H|^2 \rangle \langle |E_V|^2 \rangle}}. \quad (18)$$

(4) *Conformity Coefficient*. Conformity coefficient was originally proposed to distinguish land surface scattering mechanisms [21]. For CTLR CP SAR mode, it is expressed as [21]

$$\text{Conf} \cong \frac{2 \text{Im} (\langle E_H E_V^* \rangle)}{\langle E_H E_H^* \rangle + \langle E_V E_V^* \rangle}. \quad (19)$$

(5) *Coherency Coefficient*. For CTLR CP SAR mode, the coherency coefficient can be derived by [2]

$$\text{Coh} = \frac{|D_{12}|}{\sqrt{D_{11}D_{22}}}, \quad (20)$$

where the coherency matrix D can be defined as

$$D = \begin{pmatrix} \langle E_H + iE_V \rangle^2 & \langle E_H + iE_V \rangle \langle E_H - iE_V \rangle^* \\ \langle E_H + iE_V \rangle^* \langle E_H - iE_V \rangle & \langle E_H - iE_V \rangle^2 \end{pmatrix}. \quad (21)$$

(6) *Entropy*. Polarimetric entropy of CP SAR data can be directly calculated by implementing eigenvalue decomposition to the covariance matrix C_{CP} :

$$H = \sum_{i=1}^2 -P_i \log_3 P_i, \quad (22)$$

where

$$P_i = \frac{\lambda_i}{\sum_j \lambda_j} \quad (23)$$

and λ_i ($i = 1, 2$) is the eigenvalue of covariance matrix C_{CP} . Entropy that is derived directly from CP SAR data has similar property with that derived from Quad-Pol SAR data, in describing the complexity of physical scattering mechanisms of targets.

3. Comparisons of CP SAR Features for Oil Slicks Discrimination

In this experiment, SAR data acquired by Uninhabited Aerial Vehicle Synthetic Aperture Radar (UAVSAR) is used. It is a reconfigurable, fully polarimetric L-band synthetic aperture radar with a 22-km wide ground swath at 22° to 65° incidence

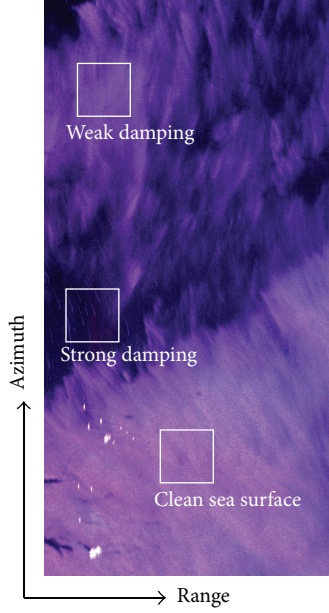


FIGURE 1: Pseudocolor image of the Quad-Pol SAR data (in dB), with red for HH^2 , green for HV^2 , and blue for VV^2 (UAVSAR data courtesy NASA/JPL-Caltech).

angles. The experimental image was taken at Gulf of Mexico on September 2, 2009, with flight number 32014-09066, in which an oil slick is present. Multilook complex (MLC) data were used for the analysis, with spatial resolution around 5.5 m. A segment was picked from the image for the convenience of analysis and display. The size of the sample was 1000 pixels in azimuth (vertical) and 500 pixels in range (horizontal) direction. Within the study area, three kinds of typical sea surface are picked out for analysis, namely, strong damping area, weak damping area, and clean sea surface. The pseudocolor image of the studied sample area is shown in Figure 1.

In this study, Pol-SAR features that are derived directly from CP SAR data and via Quad-Pol reconstruction algorithm proposed by Dubois-Fernandez et al. [19], together with those derived from original Quad-Pol SAR data, are compared. Figure 2 shows the flowchart of the whole experiment: MLC data are used as the input in form of covariance matrix. Then, based on the Quad-Pol SAR data, three different ways are used to extract polarimetric SAR features, for discriminating damping status. (1) Pol-SAR features were directly computed from coherence matrix T and covariance matrix C of Quad-Pol SAR data; (2) Quad-Pol reconstruction was implemented on simulated covariance matrix of CTRL compact polarimetric SAR data; then Pol-SAR features were extracted from the reconstructed pseudo-Quad-Pol covariance matrix; (3) CP SAR features were extracted directly from the stokes matrix \mathbf{g} , covariance matrix \mathbf{C}_{CP} , and coherence matrix \mathbf{D} of the simulated CTRL CP SAR data without the process of reconstruction. Then all the Pol-SAR features that are derived from different methods were compared and analyzed.

Figure 3 shows the six Pol-SAR features that are derived via different methods. From visual inspection, it can be observed that these corresponding features are very close to each other, except that some noises can be observed from the right part of CP SAR reconstructed features. It was also observed that, in this analyzed case, conformity coefficient holds the strongest capability of distinguishing strong and weak damping sea surface, since it has the largest within-slick contrast. This finding is in correspondence with the analysis results of [23]. Figure 4 is the histograms of these Pol-SAR features. The difference between the distributions of Quad-Pol SAR features and CP SAR features derived by different methods is generally very small, except that slightly larger difference between CPD derived by different means can be observed.

To statistically analyze the difference between polarimetric characteristics, in distinguishing strong damping, weak damping, and clean sea surface, several statistical differences can be used.

(1) *Normalized Distance between Means* (d_{norm}). Consider

$$d_{norm} = \frac{|\mu_1 - \mu_2|}{\sigma_1 + \sigma_2}, \quad (24)$$

where μ and σ are mean value and standard deviation, respectively, and subscripts 1 and 2 stand for two different sample areas, for example, weak damping (WD), strong damping (SD), and clean sea surface (sea).

(2) *Modified Distance between Samples*. Consider

$$J_d = \sum_{i=1}^C P_i \left[\frac{(m_i - m)^2}{((1/N_i) \sum_{x_i \in W_i} (x_i - m_i)^2)} \right], \quad (25)$$

where C are different classes, for example, for oil $i = 1$, sea $i = 2$; m_i is mean value of class i ; m is mean value of all classes; and P_i is prior possibility of each class, set to 0.5 in this case.

(3) *Bhattacharyya Distance*. Consider

$$B_d = -\ln \left(\sum_{i=1}^n (p_1(i), p_2(i))^{1/2} \times \Delta \right), \quad (26)$$

where $p_1(i)$ and $p_2(i)$ stand for possibilities of features from oil and sea sample in i th interval, n stands for the number of intervals used to count possibility function, which is 1000 for this experiment, and Δ stands for the length of the interval.

Experiments have proved that, in measuring statistical difference between Pol-SAR features of sea surfaces under different damping status, these three measurements have very similar performance. An example is provided in Figure 5, in which three statistical distances represented very similar trend in measuring the statistical distances between weak damping area and clean sea surface. As a result, in this study, we mainly considered the first feature d_{norm} to keep the analysis concise. d_{norm} is the statistical distance that is closely related to the performance of minimum distance based classifier.

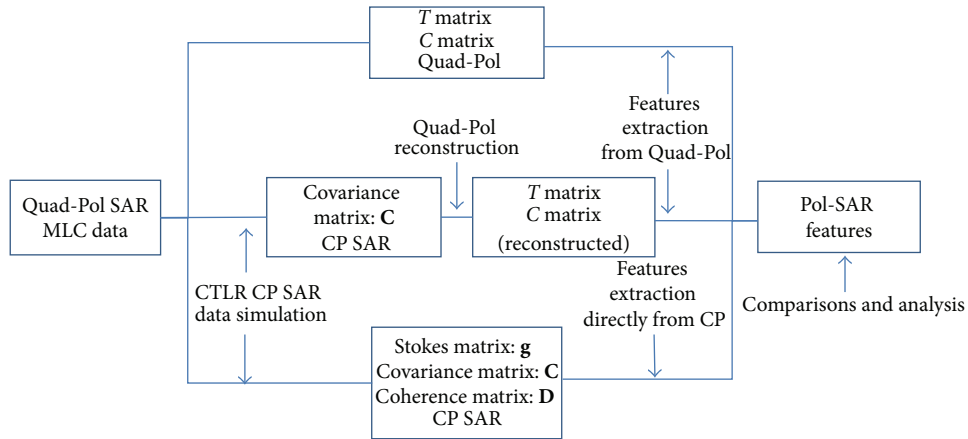


FIGURE 2: Flowchart of the experiment conducted in this paper.

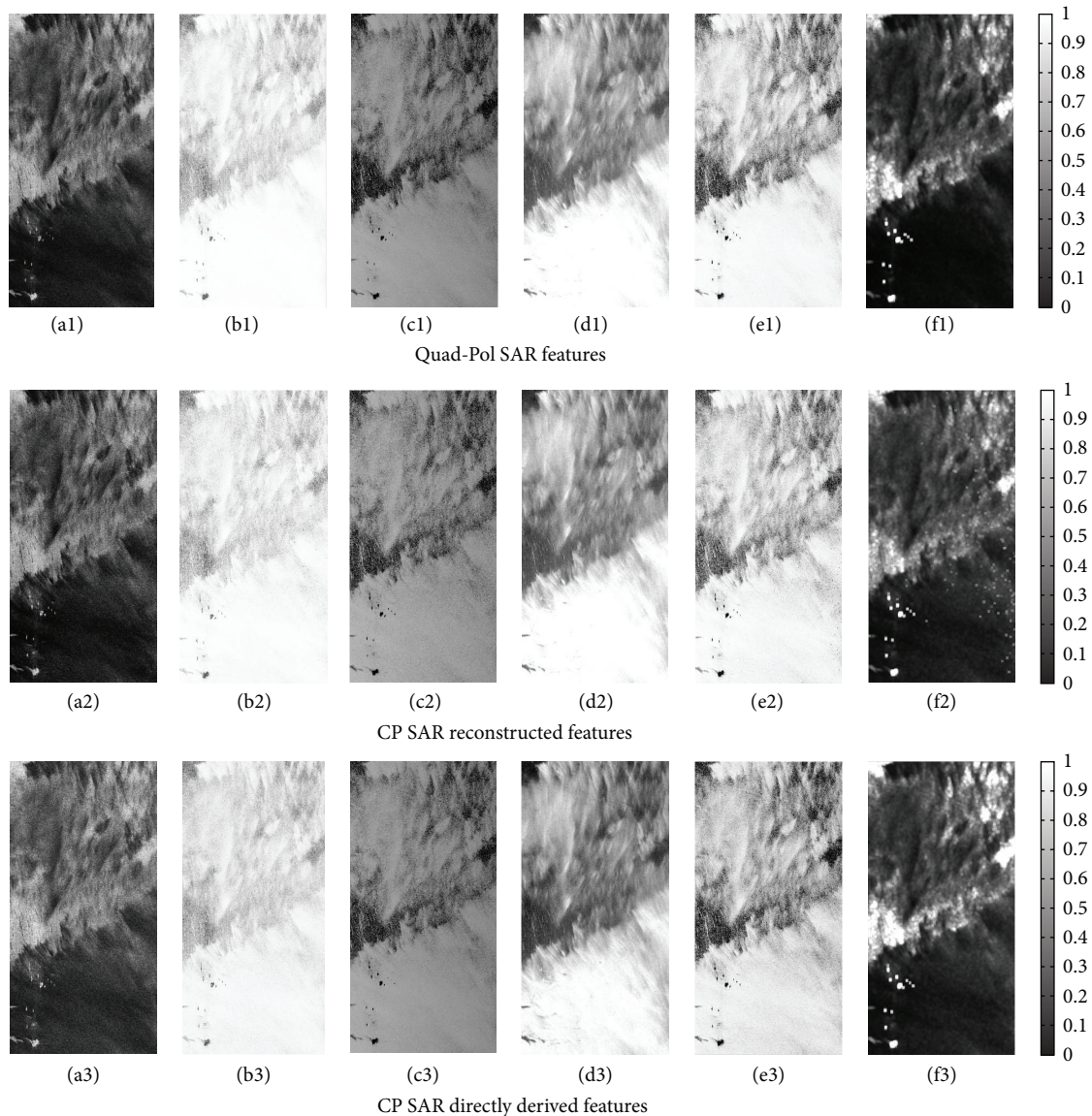
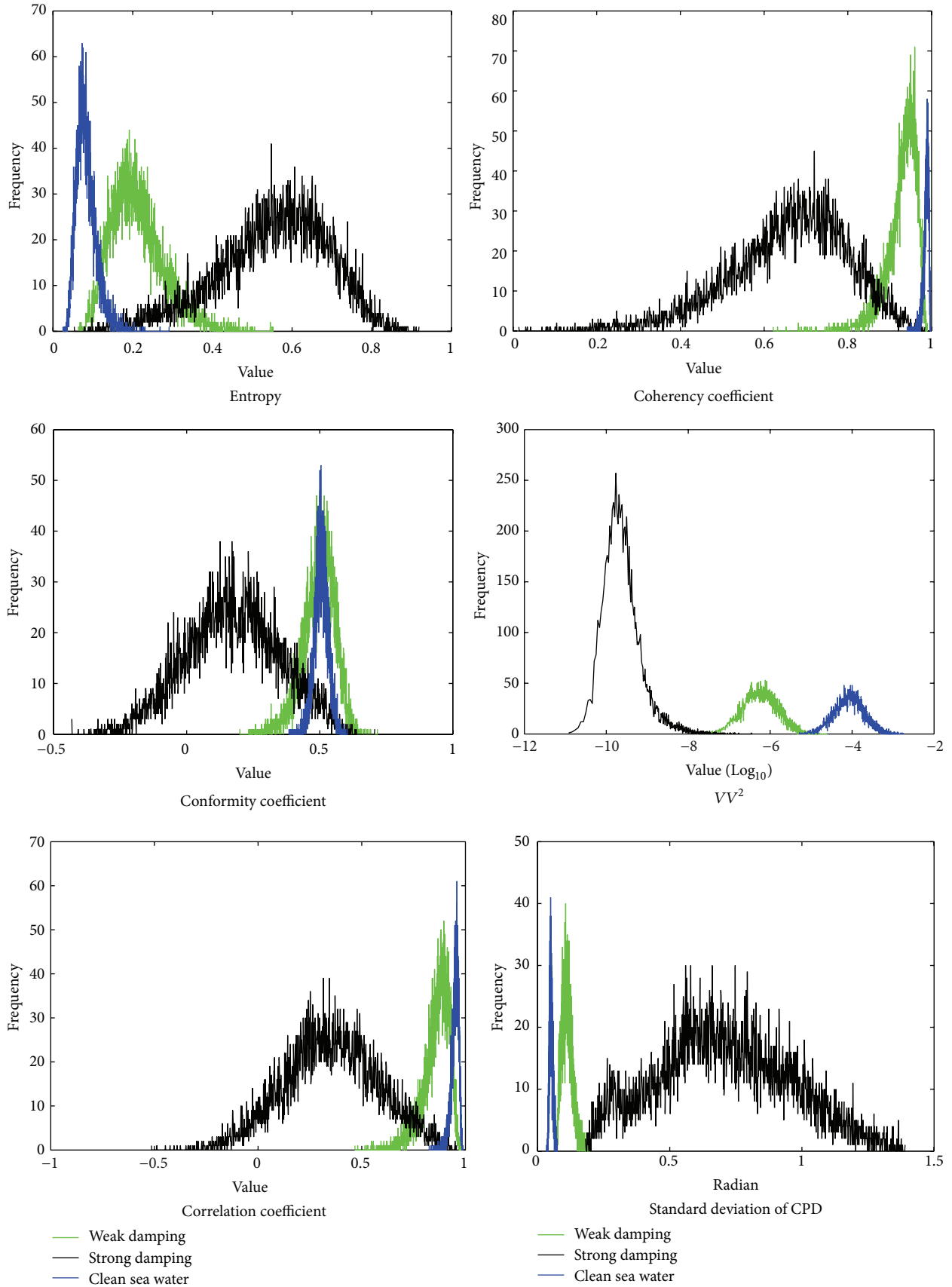
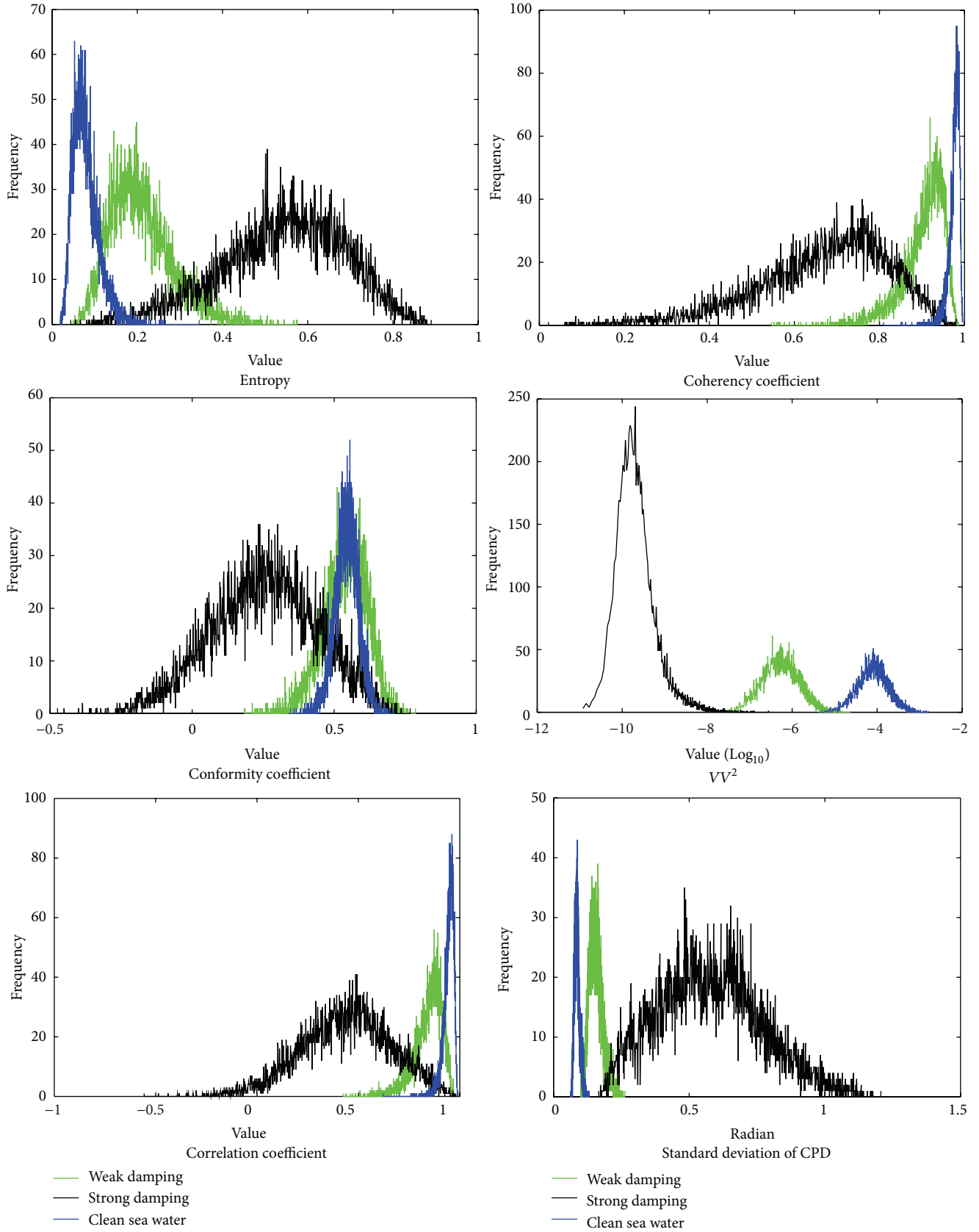


FIGURE 3: Pol-SAR features that are derived by using three different methods. From top to bottom (1~3), they are (1) features that are derived from original Quad-Pol SAR data, (2) features that are derived from reconstructed pseudo-Quad-Pol SAR data, and (3) features that are derived directly from CTLR CP SAR mode data. From left to right (a~f), they are (a) entropy, (b) coherency coefficient, (c) conformity coefficient, (d) $VV^2 (|E_V|^2)$, (e) correlation coefficient, and (f) standard deviation of CPD.



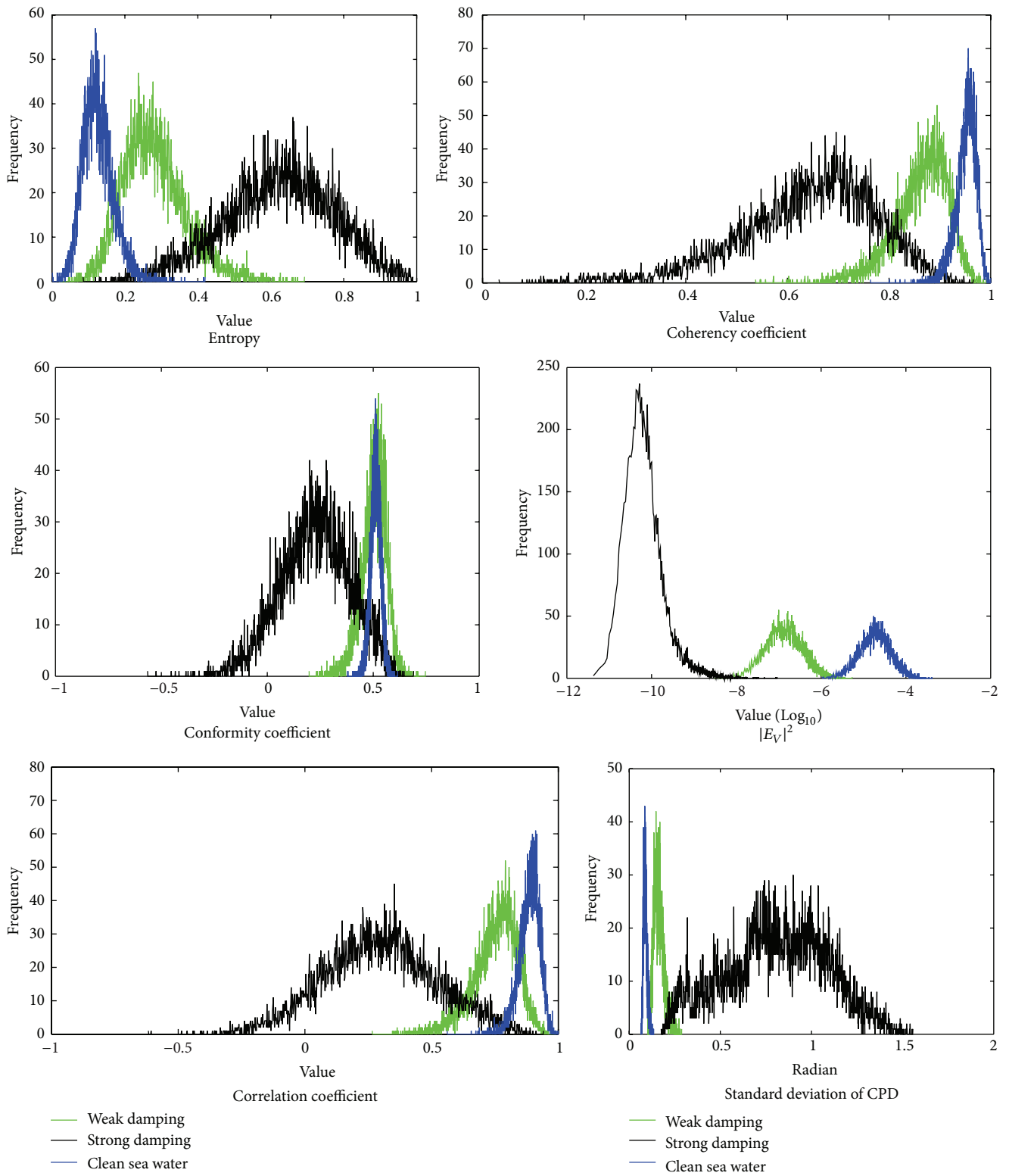
(a) Quad-Pol SAR features

FIGURE 4: Continued.



(b) CP SAR reconstructed features

FIGURE 4: Continued.



(c) CP SAR directly derived features

FIGURE 4: Histograms of Pol-SAR features in Figure 3. From top to bottom are (a) features that are derived from Quad-Pol covariance matrix, (b) features that are derived from pseudocovariance matrix that is reconstructed from CP SAR data, and (c) features that are derived directly from simulated CTRLR CP SAR scattering matrix, respectively.

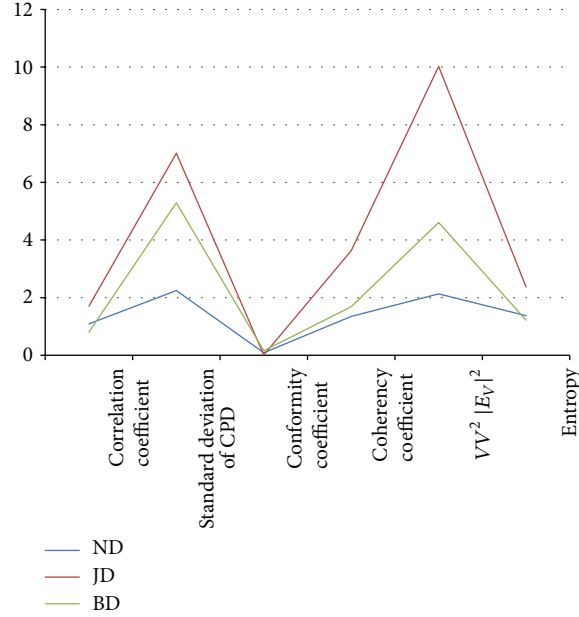


FIGURE 5: Statistical differences of Pol-SAR features between weak damping and clean sea surface measured by different means. ND: normalized distance between means; JD: modified distance between samples; and BD: Bhattacharyya distance.

TABLE 1: d_{norm} of Pol-SAR features between clean sea surface and weak damping and strong damping areas.

Characteristics	$d_{\text{WD-Sea}}$			$d_{\text{SD-Sea}}$		
	QP	CP Rec.	CP Direct	QP	CP Rec.	CP Direct
Corr Co.	1.0864	0.9774	1.0459	2.4303	2.0582	2.2730
Std. CPD	2.2471	1.9823	1.9761	2.4984	2.4409	2.4394
Conf Co.	0.0894	0.0385	0.0954	1.6407	1.2837	1.5191
Coh Co.	1.3477	1.1519	1.1924	2.2048	1.8323	2.0127
$VV^2 E_V ^2$	2.1294	2.1374	2.1124	2.7468	2.7590	2.7330
Entropy	1.3759	1.2513	1.2088	2.8360	2.6281	2.5658

Normalized distances calculated from Quad-Pol and CP SAR features are listed in Table 1. They are calculated by (24) from three sample areas of different damping status. It can be observed that, for all these features, normalized distance between strong damping area and clean sea surface ($d_{\text{SD-Sea}}$) is larger than that between weak damping area and clean sea surface ($d_{\text{WD-Sea}}$). This is in accordance with physical interpretation: stronger damping properties cause Pol-SAR features in this area to have larger deviation than those in clean sea surface.

From Table 1 it also can be found that, in terms of segmenting oil slicks from oil-free sea background, VV^2 is the most effective feature. Since the normalized difference of VV^2 between strong damping area and clean sea surface is the largest, it was one of the most previously used features in traditional single polarimetric SAR based applications. However, in terms of distinguishing weak damping from strong damping properties, other polarimetric SAR features work far better than VV^2 , among them the conformity coefficient works the best, manifesting the fact that for this dataset it has the largest capability in distinguishing different damping status. It should be noted that the feature CPD does

not work well on this dataset, but it could be a very good damping status indicator on SAR data of shorter wavelength, for example, C and X bands [4].

Polarimetric SAR features considered in the analysis stand for different physical meanings and they could all help in the oil slicks classification. More analysis and comparisons of these Pol-SAR features in distinguishing different damping status can be found in previous studies [2, 23, 24]. In this paper, however, we mainly focus on analyzing the differences of Pol-SAR features that are derived by two different methods from CP SAR data, namely, directly and through pseudo-Quad-Pol reconstruction.

To further evaluate the performance of CP SAR feature extraction methods, relative difference between d_{norm} that is extracted from Quad-Pol and CP SAR data was calculated:

$$\text{Rd} = \frac{(d_{\text{norm_QP}} - d_{\text{norm_CP}})}{d_{\text{norm_QP}}}, \quad (27)$$

where $d_{\text{norm_QP}}$ stands for $d_{\text{WD-Sea}}$ and $d_{\text{SD-Sea}}$ that are calculated by Quad-Pol data (QP column in Table 1) and $d_{\text{norm_CP}}$ stands for those features that are calculated from CP SAR

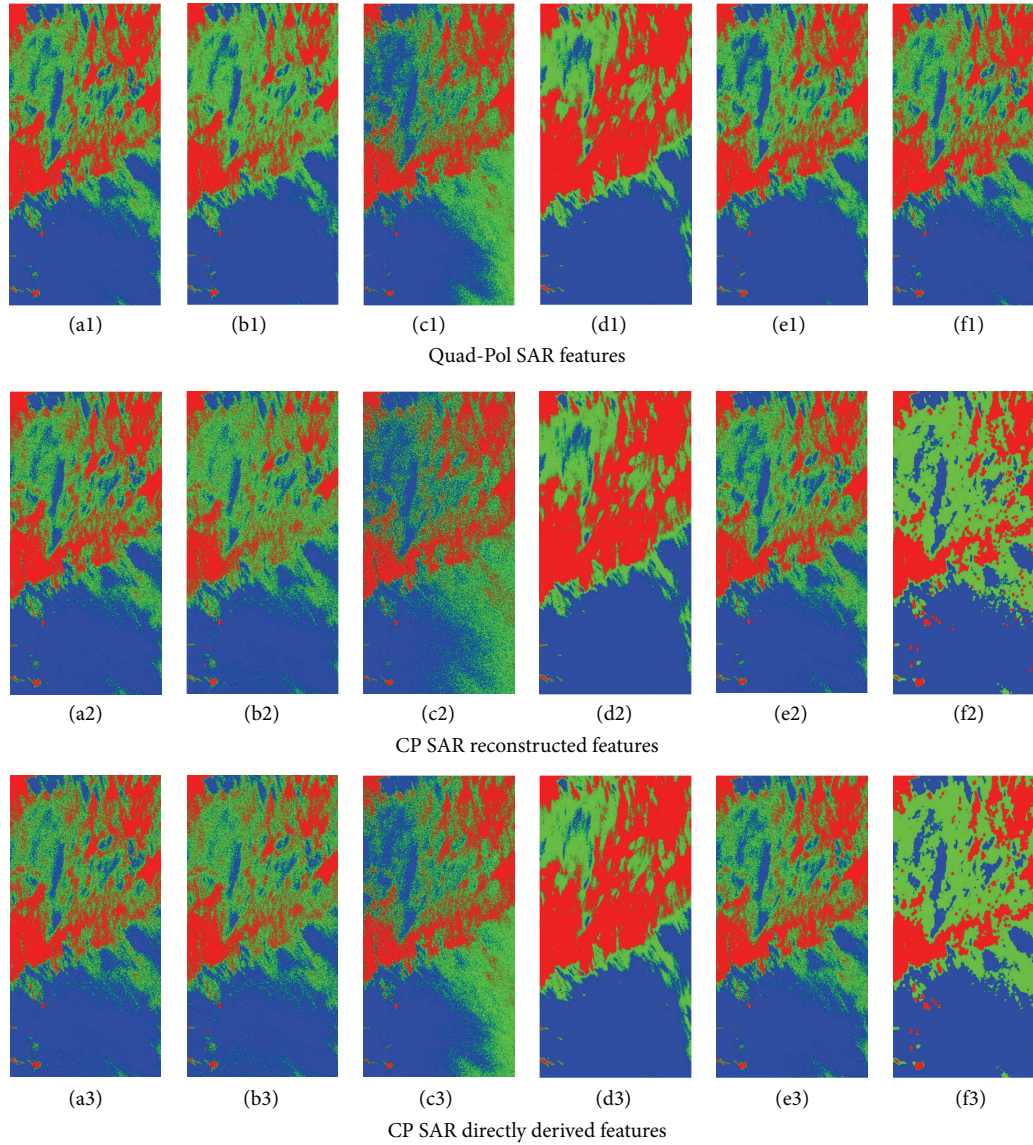


FIGURE 6: K -means segmentation of Pol-SAR features that are derived by taking three different methods. The results of different features are listed in the same sequence as in Figure 3.

data, either with or without CP SAR reconstruction (CP Rec. or CP Direct column in Table 1).

The smaller the relative difference, the closer the CP SAR feature to its corresponding original Quad-Pol one and the better the polarimetric information was preserved by taking this method. In Table 2 Rd_{WD-sea} stands for the relative distance that is calculated between the normalized difference of Pol-SAR features in weak damping and clean sea surface (column d_{WD-Sea} in Table 1) and similarly for Rd_{SD-sea} . From Table 2 it is observed that in calculating features such as VV^2 ($|E_V|^2$) and entropy, reconstruction based method resulted in smaller Rd compared with the method that extracts Pol-SAR features directly. Whereas for features such as correlation coefficient, conformity coefficient, and coherency coefficient, extracting Pol-SAR features directly can achieve lower Rd.

For standard deviation of CPD, performances by taking these two methods are very close.

4. Experiments on Oil Slicks Segmentation

In this section, conventional K -means clustering was used to partition previously derived Pol-SAR features into three classes. K -means clustering is an unsupervised partitioning method that ensures that members' objects belonging to each class have the smallest distance to its centroid.

Figure 6 shows the results of the K -means clustering. The segmentation results are consistent with previous analysis: Conf Co. could reflect the details of damping properties to the largest extent, followed by Corr Co. and other Pol-SAR features. Based on single polarimetric feature VV^2 ,

TABLE 2: Relative difference Rd between d_{norm} estimated from Quad-Pol, CP reconstruction, and CP Direct methods.

Features	$Rd_{\text{WD-sea}}$		$Rd_{\text{SD-sea}}$	
	QP versus CP Rec.	QP versus CP Direct	QP versus CP Rec.	QP versus CP Direct
Corr Co.	-0.10033137	-0.037279087	-0.15310867	-0.06472452
Std. CPD	-0.117840773	-0.120599884	-0.023014729	-0.023602305
Conf Co.	-0.56935123	0.067114094	-0.217590053	-0.074114707
Coh Co.	-0.145284559	-0.115233361	-0.168949565	-0.087128084
$VV^2 E_V ^2$	0.003756927	-0.00798347	0.004441532	-0.005024028
Entropy	-0.090558907	-0.12144778	-0.073307475	-0.095275035

TABLE 3: Accuracy assessment of CP SAR features based segmentation results that take Quad-Pol SAR results for ground truth.

Features	Overall accuracy		Kappa coefficient	
	CP Rec.	CP Direct	CP Rec.	CP Direct
Corr Co.	84.50%	85.401%	0.7763	0.7613
Std. CPD	85.17%	90.58%	0.8207	0.8517
Conf Co.	77.55%	92.88%	0.6582	0.8914
Coh Co.	82.27%	82.78%	0.7271	0.7329
$VV^2 E_V ^2$	98.63%	96.54%	0.9791	0.9473
Entropy	88.95%	86.29%	0.8318	0.7917

large homogenous segmentation area was obtained, which manifests its limitation in distinguishing different damping status of oil slicks and other marine phenomena.

Taking the segmentation result derived from Quad-Pol SAR features as ground truth, the CP SAR features based segmentation results can be quantitatively evaluated by overall accuracy and Kappa coefficient. Both of these parameters measure the performance of CP SAR derived features. In Table 3, the results of accuracy assessment are consistent with Rd listed in Table 2. The highest segmentation accuracy was achieved by VV^2 derived from pseudo-Quad-Pol reconstruction with overall accuracy of 98.63% and Kappa coefficient of 0.9791. Among all these features, the segmentation accuracy of conformity coefficient has the largest difference between different CP SAR feature extraction methods. Coincidentally in Table 2, Rd of conformity coefficient derived by different methods also holds the largest difference. Although accuracy parameters in Table 3 are computed from the whole image while Rd is only estimated from selected three typical sample areas, they are highly consistent with each other.

5. Summary

In this paper, the performance of CTRLR compact polarimetric SAR features in distinguishing different damping status of oil slicks is evaluated. Six categories of mainly used Pol-SAR features were considered in the analysis. They were derived from original Quad-Pol SAR data, from reconstructed pseudo-Quad-Pol SAR data, and directly from CP SAR mode data, respectively.

To statistically analyze the behavior of these polarimetric SAR features, normalized difference between the means is

considered (Table 1). Then relative difference Rd is computed to measure their capabilities of distinguishing different damping status (Table 2). From the analysis it was found that optimum feature extraction methods from CP SAR varied for different features. Table 2 demonstrated that for VV^2 ($|E_V|^2$) and entropy, Souyris' reconstruction algorithm based feature extraction works better. Whereas for correlation coefficient, conformity coefficient, and coherency coefficient, directly extracting Pol-SAR features could maintain the polarimetric information to a larger extent.

Probable explanations for these findings are as follows: polarimetric entropy of Quad-Pol and CP SAR data is calculated based on different numbers of eigenvalues. Besides, VV^2 and $|E_V|^2$ of Quad-Pol and CTRLR CP SAR data contain different scattering coefficient elements. As the result, these two features derived from Quad-Pol reconstruction are more similar to those derived from original Quad-Pol SAR data, for their closer data structure. For features such as correlation coefficient, conformity coefficient, and coherency coefficient, they are closely related to relative phase between polarimetric channels and sensitive to the errors induced during the process of Quad-Pol reconstruction. As the result, extracting those features directly from CP SAR modes may achieve higher accuracy compared with calculating them from reconstructed pseudo-Quad-Pol SAR data, since extracting features directly could avoid adding noise and bias to the sample data.

K-means clustering was implemented to all of these Pol-SAR features to examine their capabilities in distinguishing different damping properties. Through classification accuracy assessment based on overall accuracy and Kappa coefficient, the performance of different feature extraction methods can be further compared (see Table 3). The result is also consistent with previous analysis result (Table 2).

Although the analysis was carried on limited data samples, some basic characteristics of features derived from CP SAR modes can be obtained. CTRLR CP SAR mode proved again its potential in obtaining damping status of oil slicks and sea surfaces. The performance of CP SAR features in oil slicks classification is comparable to that obtained in Quad-Pol SAR modes. Due to some limitations, the analysis in this paper was conducted only on MLC data of UAVSAR, which is processed from SLC data by JPL with a multilook of 12 pixels in azimuth direction and 3 pixels in range direction. It has to be noted that, in the generation of MLC data, symmetry assumption is assumed, and its actual affection on

reconstruction and feature extraction should be evaluated in future study.

To derive general rules for feature extraction, more data samples under various damping status and sea conditions have to be considered. However this paper proposed a framework of selecting optimum CP SAR features based on statistical analysis on typical data samples. In the near future, there will be plenty of SAR satellites offering compact polarimetric SAR modes, which will provide polarimetric observation of sea surface with larger coverage area. We are confident that this technique will be further developed and make more contribution to operational marine oil-spills monitoring.

Conflict of Interests

The authors declare that there is no conflict of interests regarding the publication of this paper.

Acknowledgments

This work is partially supported by the National Key Basic Research Program of China (2015CB954103), the National Natural Science Foundation of China (Grants nos. 41171146 and 41271434), and the Collaborative Innovation Center for Major Ecological Security Issues of Jiangxi Province and Monitoring Implementation (no. JXS-EW-00). The authors would also like to thank JPL, NASA, for providing the UAVSAR data and the anonymous reviewers for their insightful comments that greatly improved the quality of the paper.

References

- [1] M. Gade and W. Alpers, "Using ERS-2 SAR images for routine observation of marine pollution in European coastal waters," *Science of the Total Environment*, vol. 237-238, pp. 441-448, 1999.
- [2] A.-B. Salberg, Ø. Rudjord, and A. H. S. Solberg, "Oil spill detection in hybrid-polarimetric SAR images," *IEEE Transactions on Geoscience and Remote Sensing*, vol. 52, no. 10, pp. 6521-6533, 2014.
- [3] M. Migliaccio, G. Ferrara, A. Gambardella, and F. Nunziata, "A new stochastic model for oil spill observation by means of single-look SAR data," *Environmental Research, Engineering and Management*, vol. 39, pp. 24-29, 2007.
- [4] M. Migliaccio, F. Nunziata, and A. Gambardella, "On the co-polarized phase difference for oil spill observation," *International Journal of Remote Sensing*, vol. 30, no. 6, pp. 1587-1602, 2009.
- [5] K. Topouzelis, D. Stathakis, and V. Karathanassi, "Investigation of genetic algorithms contribution to feature selection for oil spill detection," *International Journal of Remote Sensing*, vol. 30, no. 3, pp. 611-625, 2009.
- [6] Y. Zhang, Y. Li, and H. Lin, "Oil-spill pollution remote sensing by synthetic aperture radar," in *Advanced Geoscience Remote Sensing*, chapter 2, pp. 27-50, 2014.
- [7] J. Yang, T. Xiong, and Y.-N. Peng, "Polarimetric SAR image classification by using generalized optimization of polarimetric contrast enhancement," *International Journal of Remote Sensing*, vol. 27, no. 16, pp. 3413-3424, 2006.
- [8] Y. Cui, Y. Yamaguchi, J. Yang, H. Kobayashi, S.-E. Park, and G. Singh, "On complete model-based decomposition of polarimetric sar coherency matrix data," *IEEE Transactions on Geoscience and Remote Sensing*, vol. 52, no. 4, pp. 1991-2001, 2014.
- [9] J. Chen and S. Quegan, "Calibration of spaceborne CTRLR compact polarimetric low-frequency SAR using mixed radar calibrators," *IEEE Transactions on Geoscience and Remote Sensing*, vol. 49, no. 7, pp. 2712-2723, 2011.
- [10] Y. Li, Y. Zhang, J. Chen, and H. Zhang, "Improved compact polarimetric SAR Quad-pol reconstruction algorithm for oil spill detection," *IEEE Geoscience and Remote Sensing Letters*, vol. 11, no. 6, pp. 1139-1142, 2014.
- [11] R. Shirvany, M. Chabert, and J.-Y. Tourneret, "Ship and oil-spill detection using the degree of polarization in linear and hybrid/compact dual-pol SAR," *IEEE Journal of Selected Topics in Applied Earth Observations and Remote Sensing*, vol. 5, no. 3, pp. 885-892, 2012.
- [12] L. Xie, H. Zhang, C. Wang, F. Wu, B. Zhang, and Y. Tang, "Maritime application using H-a decomposition in compact and dual-pol SAR," in *Proceedings of the Asia-Pacific Conference on Synthetic Aperture Radar (APSAR '13)*, pp. 563-566, September 2013.
- [13] M. J. Collins, M. Denbina, and G. Atteia, "On the reconstruction of quad-pol sar data from compact polarimetry data for ocean target detection," *IEEE Transactions on Geoscience and Remote Sensing*, vol. 51, no. 1, pp. 591-600, 2013.
- [14] J. Yin, J. Yang, Z. Zhou, and J. Song, "The extended bragg scattering model-based method for ship and oil-spill observation using compact polarimetric SAR," *IEEE Journal of Selected Topics in Applied Earth Observations and Remote Sensing*, no. 99, pp. 1-13, 2014.
- [15] F. Nunziata, M. Migliaccio, and X. Li, "Sea oil slick observation using hybrid-polarity SAR architecture," *IEEE Journal of Oceanic Engineering*, vol. PP, no. 99, pp. 1-15, 2014.
- [16] J. Chen and S. Quegan, "Calibration of spaceborne CTRLR compact polarimetric low-frequency SAR using mixed radar calibrators," *IEEE Transactions on Geoscience and Remote Sensing*, vol. 49, no. 7, pp. 2712-2723, 2011.
- [17] R. K. Raney, "Hybrid-polarity SAR architecture," *IEEE Transactions on Geoscience and Remote Sensing*, vol. 45, no. 11, pp. 3397-3404, 2007.
- [18] R. K. Raney, P. D. Spudis, B. Bussey et al., "The lunar mini-RF radars: hybrid polarimetric architecture and initial results," *Proceedings of the IEEE*, vol. 99, no. 5, pp. 808-823, 2011.
- [19] P. C. Dubois-Fernandez, J.-C. Souyris, S. Angelliaume, and F. Garestier, "The compact polarimetry alternative for spaceborne SAR at low frequency," *IEEE Transactions on Geoscience and Remote Sensing*, vol. 46, no. 10, pp. 3208-3222, 2008.
- [20] M. E. Nord, T. L. Ainsworth, J.-S. Lee, and N. J. S. Stacy, "Comparison of compact polarimetric synthetic aperture radar modes," *IEEE Transactions on Geoscience and Remote Sensing*, vol. 47, no. 1, pp. 174-188, 2009.
- [21] B. Zhang, W. Perrie, X. Li, and W. G. Pichel, "Mapping sea surface oil slicks using RADARSAT-2 quad-polarization SAR image," *Geophysical Research Letters*, vol. 38, Article ID L10602, 2011.
- [22] S. R. Cloude and E. Pottier, "An entropy based classification scheme for land applications of polarimetric SAR," *IEEE Transactions on Geoscience and Remote Sensing*, vol. 35, no. 1, pp. 68-78, 1997.

- [23] Y. Li, H. Lin, Y. Zhang, and J. Chen, "Analysis of polarimetric features from CTLR compact polarimetric SAR data for discriminating oil slick damping status," in *Proceedings of the IEEE International Geoscience and Remote Sensing Symposium*, pp. 3490–3493, July 2014.
- [24] S. Skrunes, C. Brekke, and T. Eltoft, "Characterization of marine surface slicks by radarsat-2 multipolarization features," *IEEE Transactions on Geoscience and Remote Sensing*, vol. 52, no. 9, pp. 5302–5319, 2014.

Research Article

Model-Based Pseudo-Quad-Pol Reconstruction from Compact Polarimetry and Its Application to Oil-Spill Observation

Junjun Yin,^{1,2} Wooil Moon,¹ and Jian Yang²

¹*Geophysics, Faculty of Environment, Earth and Resources, University of Manitoba, Room 328, Wallace Building, Winnipeg, MB, Canada R3T 2N2*

²*Department of Electronic Engineering, Tsinghua University, Room 8-302, Rohm Building, Beijing 100084, China*

Correspondence should be addressed to Junjun Yin; yinjj07@gmail.com

Received 30 December 2014; Revised 16 March 2015; Accepted 15 April 2015

Academic Editor: Mike McShane

Copyright © 2015 Junjun Yin et al. This is an open access article distributed under the Creative Commons Attribution License, which permits unrestricted use, distribution, and reproduction in any medium, provided the original work is properly cited.

Compact polarimetry is an effective imaging mode for wide area observation, especially for the open ocean. In this study, we propose a new method for pseudo-quad-polarization reconstruction from compact polarimetry based on the three-component decomposition. By using the decomposed powers, the reconstruction model is established as a power-weighted model. Further, the phase of the copolarized correlation is taken into consideration. The phase of double-bounce scattering is closer to π than to 0, while the phase of surface scattering is closer to 0 than to π . By considering the negative (double-bounce reflection) and positive (surface reflection) copolarized correlation, the reconstruction model for full polarimetry has a good consistency with the real polarimetric SAR data. *L*-band ALOS/PALSAR-1 fully polarimetric data acquired on August 27, 2006, over an oil-spill area are used for demonstration. Reconstruction performance is evaluated with a set of typical polarimetric oil-spill indicators. Quantitative comparison is given. Results show that the proposed model-based method is of great potential for oil-spill observation.

1. Introduction

Crude oil and petroleum products pollution has severe impact on the marine environment. It results in large scale damage to local ecosystem, presenting potential enormous harm to deep ocean and coastal fisheries, wildlife, and regeneration. Rapid increase in oil-spill pollution is primarily due to the increased human ocean activities, which increase the risk of oil-spillage from both ship/oil-platform/pipeline accidents and routine ship operations like tank washing and engine effluent discharge. One of the mostly used instruments for ocean surveillance is synthetic aperture radar (SAR), which has the all-day and all-weather imaging capability and is sensitive to the ocean surface capillary-gravity waves [1–3]. Polarimetric SAR (Pol-SAR) offers multichannel polarimetric information, and the fully or quad polarimetric (quad-pol) SAR system allows the complete backscattering characterization for scatterers. However, the fully polarimetric imaging mode suffers from system complexity, data volume, and the limited imaging coverage compared to SAR systems

which use a single polarization for transmission [4]. In 2005, a polarimetric imaging concept was proposed and generally well known as compact polarimetry (CP) [5]. At present, both the Indian RISAT-1 and JAXA ALOS/PALSAR-2 can provide the CP mode. In the future, the CP mode will be prepared for launches of other Earth Observation (EO) satellites, for example, SAOCOM-1 and Radarsat Constellation Mission (RCM).

The compact SAR data can be processed in two manners: the first one is to reconstruct pseudo-quad-polarization data from compact polarimetry, and then many quad-pol methods can be applied to the reconstructed data [5–9] for various applications; the second one is to extract target scattering information directly from compact data [4, 10, 11]. In this study, we focus on the reconstruction method. In the multipolarization reconstruction, two assumptions are very essential. One is the well-known reflection symmetry assumption, and the other is the polarization state extrapolation model, that is, the reconstruction model. There mainly exist five reconstruction methods in the literature.

Studies in [5–8] are based on reflection symmetry to estimate the pseudocovariance matrix. The main difference between these methods is that they adopt different reconstruction model parameter N . N is determined by either theoretical assumptions or empirical tests. In [9], we developed a method which can be applied to the nonreflection case based on the four-component decomposition. However, the four-component decomposition is not applied well to describe the ocean surface where reflection symmetry always holds for most sea state conditions. Methods proposed in [7] by Collins et al. and in [8] by Li et al. are designed for ocean target detection. However, both methods are all empirical methods which need the prior fully polarimetric SAR data to fit the model parameter N . The nonlinear regression is usually used to determine the best curve fitting parameters. The difference between these two methods is that Li's model parameter N needs updating when performing the iteration, while Collins's model parameter N is a constant only relating to the incidence angle. Moreover, in [7], Collins et al. proposed to use a negative exponential curve to estimate N for the C-band RADARSAT-2 data, while in [8], Collins's model parameter is fitted with a polynomial function for the L-band UAVSAR data. This implies that, for different SAR sensors, imaging geometry, and sea conditions, the fitting curves would probably like to vary greatly. This is not beneficial for practical applications. If the selected objective curve is not a best fit of the acquired data, then reconstruction performance can be expected to deteriorate.

In this paper, a model-based reconstruction method is proposed to extract the quad-pol information from compact polarimetry for oil-spill observation. By assuming a three-component decomposition for backscatter of the ocean surface, the model parameter N is estimated based on the decomposed scattering powers. L-band ALOS/PALSAR-1 fully polarimetric data are used for demonstration. L-band polarimetric SAR data, especially the satellite data, are not widely investigated for oil-spill detection due to its long wavelength. Since L-band polarimetric SAR satellites are in operation (e.g., ALOS/PALSAR-2) and to be planned for future missions, it is necessary to explore the performance of L-band compact polarimetric data for oil-spill observation. Performance of the proposed method is evaluated in terms of a set of polarimetric indicators which are widely used for oil-spill observation in the literature [1]. The organization of the rest of this paper is as follows. In Section 2, we briefly introduce the L-band test data. In Section 3, the proposed reconstruction method is presented. Section 4 gives the experiments and comparison; and conclusions are given in Section 5.

2. Test Data and Preprocessing

L-band ALOS/PALSAR-1 fully polarimetric data acquired over the southern-eastern coast of Negros Island on August 27, 2006, are used for demonstration. These data are relevant to an oil-spill accident happened on August 11, 2006 [12]. A subset of the image is shown in Figure 1, from which we can see dark areas of oil-slicks. The fully polarimetric data are

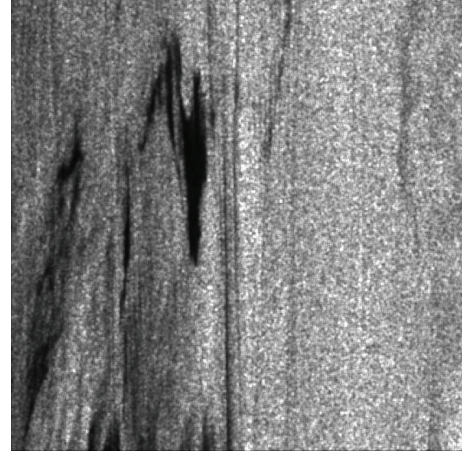


FIGURE 1: Span image of the test data, acquired on August 27, 2006. ALOS/PALSAR-1 site identification is ALPSRP031440190. The dark area is an oil-slick [12].

received in the single look complex (SLC) product format. This subset contains 1088×1088 pixels. Before performing analysis, a boxcar filter with a window size 7 has been applied to reduce the speckle. Linear compact polarimetric SAR data are synthesized from the fully polarimetric SAR data according to its specific scattering matrix, which will be introduced in Section 3.

3. Pseudo-Quad-Polarization Reconstruction from Linear Compact Polarimetry

3.1. Quad-Pol Data and Three-Component Decomposition. In the linear horizontal (H) and vertical (V) polarization base, the scattering vector is defined as shown in the following equation under the reciprocity theorem for the monostatic backscattering case:

$$\vec{k}_L = [S_{HH} \quad \sqrt{2}S_{HV} \quad S_{VV}]^T, \quad (1)$$

where S_{HV} denotes V in transmission and H in reception. For the multilook case, the covariance matrix is shown in the following equation to represent the average scattering property:

$$\begin{aligned} \mathbf{C} &= \left\langle \vec{k}_L \vec{k}_L^H \right\rangle \\ &= \begin{bmatrix} \langle |S_{HH}|^2 \rangle & \sqrt{2} \langle S_{HH} S_{HV}^* \rangle & \langle S_{HH} S_{VV}^* \rangle \\ \sqrt{2} \langle S_{HV} S_{HH}^* \rangle & 2 \langle |S_{HV}|^2 \rangle & \sqrt{2} \langle S_{HV} S_{VV}^* \rangle \\ \langle S_{VV} S_{HH}^* \rangle & \sqrt{2} \langle S_{VV} S_{HV}^* \rangle & \langle |S_{VV}|^2 \rangle \end{bmatrix}, \quad (2) \end{aligned}$$

where $\langle \dots \rangle$ and H denote spatial average and matrix transpose conjugate, respectively and * denotes complex conjugation. Polarimetric target decomposition has been studied by many researchers [13–15]. Model-based decomposition aims to decompose the radar received backscattered energy into

several components according to scattering models. Three-component decomposition [13] can be written as follows:

$$\mathbf{C} = f_s [\mathbf{C}_s] + f_d [\mathbf{C}_d] + f_v [\mathbf{C}_v], \quad (3)$$

where f_s , f_d , and f_v are decomposed parameters to be determined corresponding to the surface, double-bounce, and volume scattering models, respectively. These three scattering models are given by

$$\begin{aligned} [\mathbf{C}_s] &= \begin{bmatrix} |\beta|^2 & 0 & \beta \\ 0 & 0 & 0 \\ \beta^* & 0 & 1 \end{bmatrix}, \\ [\mathbf{C}_d] &= \begin{bmatrix} |\alpha|^2 & 0 & \alpha \\ 0 & 0 & 0 \\ \alpha^* & 0 & 1 \end{bmatrix}, \\ [\mathbf{C}_v] &= \begin{bmatrix} 1 & 0 & b \\ 0 & 1-b & 0 \\ b & 0 & 1 \end{bmatrix}, \quad b \in [0, 1), \end{aligned} \quad (4)$$

where β and α are model parameters with $\arg(\beta) \approx 0$ and $\arg(\alpha) \approx \pm\pi$. Different three-component decomposition methods are generally developed by modifying the volume scattering model $[\mathbf{C}_v]$. $[\mathbf{C}_v]$ presented in (4) is a general volume scattering model exhibiting scattering azimuthal symmetry. In Freeman and Durden's 3-component decomposition [13, 15], b is set to 1/3. Effects of the parameter b on scattering powers and on the compact reconstruction model will be discussed in the next section. If we let $b = 0$, by relating (3) and (4) to (2), the backscattered energy span can be expanded into scattering powers as shown in the following:

$$\begin{aligned} P_s &= f_s (1 + |\beta|^2), \\ P_d &= f_d (1 + |\alpha|^2), \\ P_v &= 3f_v = 6 \langle |S_{HV}|^2 \rangle, \\ \text{span} &= \langle |S_{HH}|^2 \rangle + 2 \langle |S_{HV}|^2 \rangle + \langle |S_{VV}|^2 \rangle \\ &= P_s + P_d + P_v, \end{aligned} \quad (5)$$

where P_s , P_d , and P_v are the decomposed powers. Since this decomposition has 5 unknowns with 4 equations, the sign of $\text{Re}(\langle S_{HH}S_{VV}^* \rangle)$ is usually used to determine whether surface reflection or double-bounce reflection is dominant [13]. Specifically, if $\text{Re}(\langle S_{HH}S_{VV}^* \rangle) > 0$, then let $\alpha = -1$ (indicating a dominant surface reflection); if $\text{Re}(\langle S_{HH}S_{VV}^* \rangle) < 0$, then let $\beta = 1$ (indicating a dominant double-bounce reflection), where $\text{Re}(\dots)$ indicates the real part of a complex number.

3.2. Compact Polarimetry and the Proposed Model-Based Reconstruction Model

3.2.1. Linear $\pi/4$ Compact Data. The compact system measures a projection of the complex scattering matrix \mathbf{S} onto a transmitted electromagnetic field \vec{E}_i . When transmitting a slant-linear polarization oriented at 45° , the received electromagnetic wave is given by

$$\begin{aligned} \vec{E}_r &= \vec{S}\vec{E}_i = \frac{1}{\sqrt{2}} \begin{bmatrix} S_{HH} & S_{HV} \\ S_{HV} & S_{VV} \end{bmatrix} \begin{bmatrix} 1 \\ 1 \end{bmatrix} \\ &= \frac{1}{\sqrt{2}} \begin{bmatrix} S_{HH} + S_{HV} \\ S_{VV} + S_{HV} \end{bmatrix}. \end{aligned} \quad (6)$$

\vec{E}_r is called the Jones vector of the scattered wave. Equation (6) gives the scattering vector for the $\pi/4$ compact mode. We usually use the wave covariance matrix, defined in (7), to analyze the target average scattering property. From (7), it is seen that for the $\pi/4$ mode, the covariance matrix $\mathbf{C}_{\pi/4}$ can be written as a sum of three parts, that is, a copolarized information part, a cross-polarization part, and the residue part:

$$\begin{aligned} \mathbf{C}_{\pi/4} &= \langle \vec{E}_r \vec{E}_r^H \rangle = \begin{bmatrix} C_{11} & C_{12} \\ C_{21} & C_{22} \end{bmatrix} \\ &= \frac{1}{2} \left\{ \begin{bmatrix} \langle |S_{HH}|^2 \rangle & \langle S_{HH}S_{VV}^* \rangle \\ \langle S_{VV}S_{HH}^* \rangle & \langle |S_{VV}|^2 \rangle \end{bmatrix} + \langle |S_{HV}|^2 \rangle \begin{bmatrix} 1 & 1 \\ 1 & 1 \end{bmatrix} \right. \\ &\quad \left. + \begin{bmatrix} 2\text{Re}(\langle S_{HH}S_{HV}^* \rangle) & \langle S_{HH}S_{HV}^* \rangle + \langle S_{HV}S_{VV}^* \rangle \\ \langle S_{HV}S_{HH}^* \rangle + \langle S_{VV}S_{HV}^* \rangle & 2\text{Re}(\langle S_{VV}S_{HV}^* \rangle) \end{bmatrix} \right\}. \end{aligned} \quad (7)$$

By assuming reflection symmetry, the last submatrix in (7) is usually omitted; that is, the terms involving products of copolarized and cross-polarized terms are ignored. For most terrain types, the omitted part is much smaller than the others. Reflection symmetry is also valid for the ocean surface. By this means, there are only 4 parameters left in $\mathbf{C}_{\pi/4}$, that is, $\langle |S_{HH}|^2 \rangle$, $\langle |S_{VV}|^2 \rangle$, $\langle S_{HH}S_{VV}^* \rangle$, and $\langle |S_{HV}|^2 \rangle$. In the reconstruction of pseudo-quad-pol information, these parameters need to be estimated. There are 4 unknowns, but only 3 equations can be obtained from (7), so an extra reconstruction model is needed to relate these parameters. In the literature, there exist four main reconstruction modes [5–8] which have the following general form:

$$\frac{\langle |S_{HV}|^2 \rangle}{\langle |S_{HH}|^2 \rangle + \langle |S_{VV}|^2 \rangle} = \frac{1 - |\rho|}{N}, \quad (8)$$

where ρ is the copolarization correlation coefficient, defined by $\rho = \langle S_{HH}S_{VV}^* \rangle / \sqrt{\langle |S_{HH}|^2 \rangle \langle |S_{VV}|^2 \rangle}$ and N is the model parameter which is different for different reconstruction algorithms. Souyris et al. first proposed the reconstruction model using $N = 4$. We calculate both $\langle |S_{HV}|^2 \rangle / (\langle |S_{HH}|^2 \rangle + \langle |S_{VV}|^2 \rangle)$ and ρ for the scattering models in (4), as shown

in (9). We could observe that Souyris's model satisfies all these scattering behaviours when the scattering models are considered separately:

$$\begin{aligned} \mathbf{C}_s: \quad & \frac{\langle |S_{HV}|^2 \rangle}{(\langle |S_{HH}|^2 \rangle + \langle |S_{VV}|^2 \rangle)} = 0, \quad \rho = 1, \\ \mathbf{C}_d: \quad & \frac{\langle |S_{HV}|^2 \rangle}{(\langle |S_{HH}|^2 \rangle + \langle |S_{VV}|^2 \rangle)} = 0, \quad \rho = -1, \\ \mathbf{C}_v: \quad & \frac{\langle |S_{HV}|^2 \rangle}{(\langle |S_{HH}|^2 \rangle + \langle |S_{VV}|^2 \rangle)} = \frac{1-b}{4}, \quad \rho = b. \end{aligned} \quad (9)$$

We review Souyris's model from a new perspective. A scattering process is actually a mixture of scattering processes of elemental scatterers in a resolution cell. Backscatter is affected by all the elemental scatterers. If we assume a three-component decomposition and that each component contributes to the backscattered features in the scale of its power proportion, then Souyris's model can be taken as a power-weighted model as long as the phase of ρ is not considered; that is, $|\rho|$ is used in the reconstruction model. Souyris's model does not distinguish the difference of the copolarized correlation coefficients of the surface and double-bounce reflections. The typical single-bounce reflection has a value of ρ equal to 1, while the typical double-bounce reflection has a value of ρ equal to -1 . By taking into consideration that the copolarized correlation coefficient ρ can be either positive or negative, we propose a new reconstruction model based on three-component decomposition, given in the next section.

3.2.2. The Proposed Reconstruction Model. From (9), we can establish a model-based power-weighted reconstruction model. By assuming that the backscattered energy is a sum of the surface scattering power P_s , double-bounce scattering power P_d , and volume scattering power P_v , the following relationship can be obtained:

$$\begin{aligned} & \mathbf{C}_s + \mathbf{C}_d + \mathbf{C}_v \\ \Rightarrow & \left\{ \begin{aligned} \frac{\langle |S_{HV}|^2 \rangle}{\langle |S_{HH}|^2 \rangle + \langle |S_{VV}|^2 \rangle} &= \frac{1-b}{4} \frac{P_v}{\text{span}} \\ \frac{1-\rho}{4} &= \frac{2P_d + (1-b)P_v}{4\text{span}}. \end{aligned} \right. \quad (10) \end{aligned}$$

For natural distributed targets, ρ is a complex number, so $|\rho|$ is still used in the reconstruction [5]. However, in order to preserve the positive or negative correlation property (i.e., the copolarized phase difference is either closer to 0 or closer to π) of the surface or double-bounce scattering, $\text{Re}(\langle S_{HH}S_{VV}^* \rangle)$ is incorporated in the modified model as follows:

$$\begin{aligned} & \frac{\langle |S_{HV}|^2 \rangle}{\langle |S_{HH}|^2 \rangle + \langle |S_{VV}|^2 \rangle} \\ &= \frac{1 - \text{sgn}(\text{Re}(\langle S_{HH}S_{VV}^* \rangle)) |\rho|}{4} \frac{(1-b)P_v}{2P_d + (1-b)P_v}, \end{aligned} \quad (11)$$

where $\text{sgn}(\dots)$ is a signum function. In order to find a suitable parameter b for the reconstruction, we test the equality of the two sides of (11). When b varies in the interval $[0 \ 1]$, the proportion of scattering powers decomposed from (3) varies accordingly. Using the test data for illustration, the polynomial curves fitting to the two sides of (11) is shown in Figure 2(a), from which it is observed that the fitted curve with $b = 0$ is much closer to the diagonal line than the other fitted lines. It should be noted that b should not be larger than $(\text{span} - 6\langle |S_{HV}|^2 \rangle) / (\text{span} - 2\langle |S_{HV}|^2 \rangle)$; otherwise there will occur with negative decomposed powers. Further, when b increases from 0, the number of the pixels falling in the plane of Figure 2(a) decreases. This variation is shown in Figure 2(b), which means that the number of effective pixels decreases with b increasing. Thus in order to make sure that (11) is valid and effective for most pixels and ensures the equality, b is set to 0.

Then the proposed reconstruction model is then obtained as

$$\frac{\langle |S_{HV}|^2 \rangle}{\langle |S_{HH}|^2 \rangle + \langle |S_{VV}|^2 \rangle} = \frac{1 - \text{sg} \cdot |\rho|}{4} \frac{P_v}{2P_d + P_v}, \quad (12)$$

where $\text{sg} = \text{sgn}(\text{Re}(\langle S_{HH}S_{VV}^* \rangle))$. Using the test data, Figure 3 compares the present reconstruction model with Souyris's model. It is observed that the developed model is more consistent with the real polarimetric SAR data; that is, the points are scattered much closer to the diagonal line with the proposed model.

Next we need to consider how to approximate $\text{sgn}(\text{Re}(\langle S_{HH}S_{VV}^* \rangle))$, P_d , and P_v in the linear $\pi/4$ compact polarimetric mode. From the coherency matrix shown in (7), we notice that when assuming reflection symmetry, the sign of $\text{Re}(\langle S_{HH}S_{VV}^* \rangle)$ is only affected by $\langle |S_{HV}|^2 \rangle$. For the ocean surface, the high copolarized correlation is always expected to make the copolarized terms larger than the cross-polarized term [12]. Hence, we use $\text{Re}(C_{12})$ to determine whether the backscatter process is dominated by surface or by double-bounce scattering. We use the whole data of ALPSRP031440190, which contains 18432×1088 pixels, to test the consistency between areas determined by $\text{Re}(C_{12}) > 0$ and $\text{Re}(\langle S_{HH}S_{VV}^* \rangle) > 0$. The overall agreement is 96.7%. Thus, this principle is valid and reasonable to determine which scattering mechanism dominates the backscatter of the CP mode, at least for the L-band PALSAR data.

From the covariance scattering models in (4), the corresponding compact scattering models can then be synthesized as shown in (13), where the parameter b in \mathbf{C}_v is set to 0:

$$\begin{aligned} [\mathbf{C}_s]_{\text{CP}} &= \begin{bmatrix} |\beta|^2 & \beta \\ \beta^* & 1 \end{bmatrix}; \\ [\mathbf{C}_d]_{\text{CP}} &= \begin{bmatrix} |\alpha|^2 & \alpha \\ \alpha^* & 1 \end{bmatrix}; \\ [\mathbf{C}_v]_{\text{CP}} &= \begin{bmatrix} 1.5 & 0.5 \\ 0.5 & 1.5 \end{bmatrix}. \end{aligned} \quad (13)$$

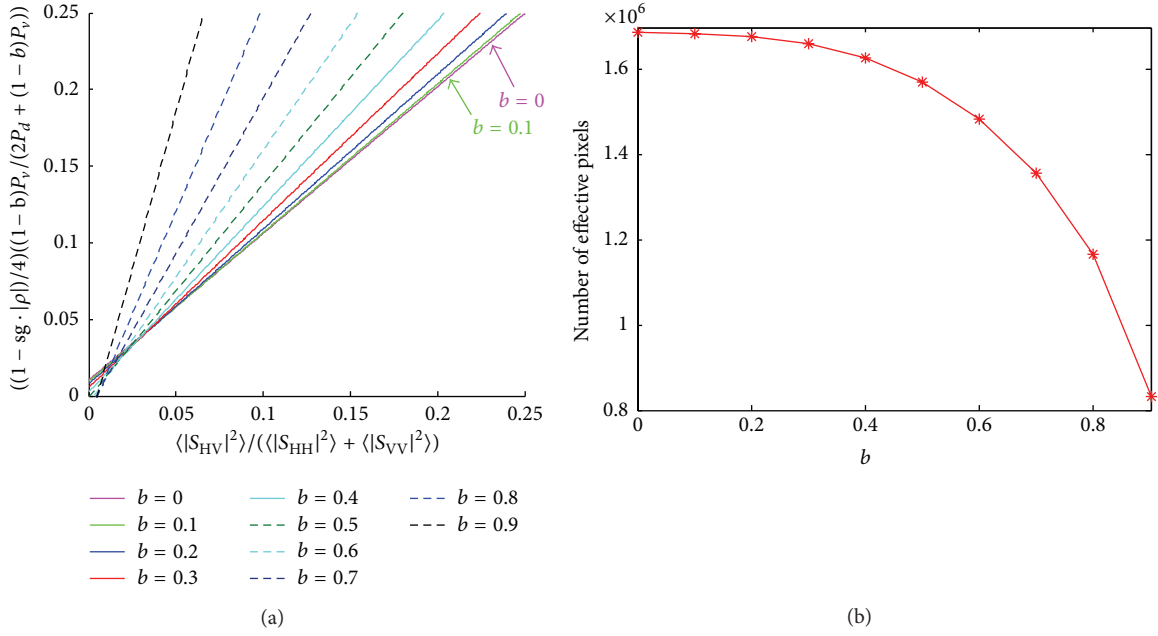


FIGURE 2: (a) First order polynomial curve fittings of the left side (shown on the abscissa) and the right side (shown on the ordinate) of (11) by varying the parameter b by using the test data. (b) Variation of b versus the number of the pixels falling in the plane in (a).

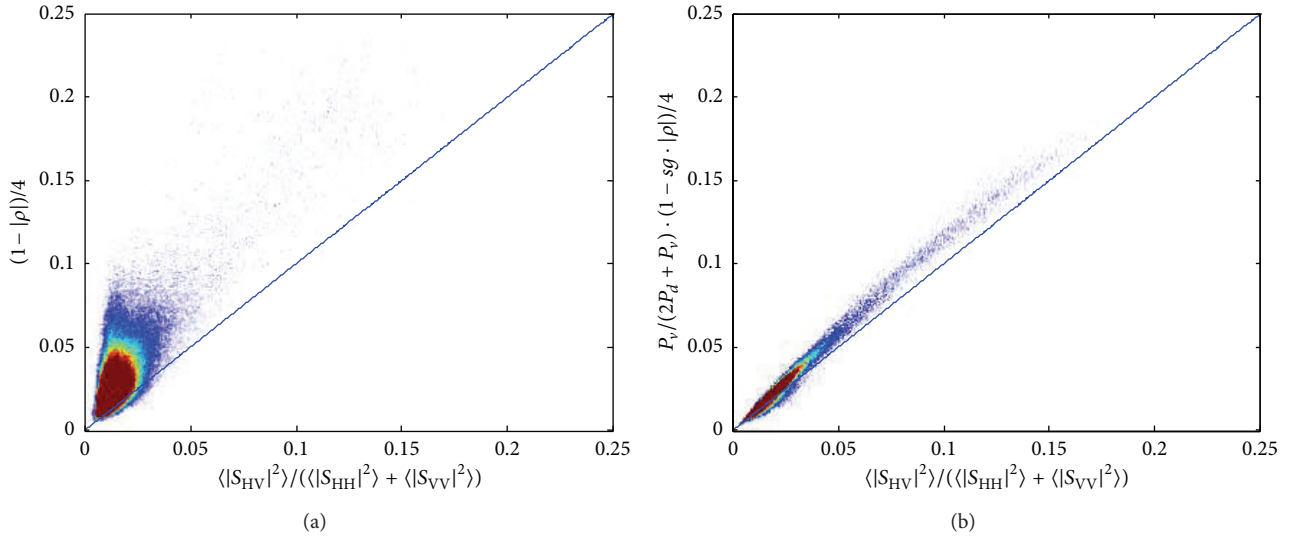


FIGURE 3: Comparison of reconstruction models. (a) Souyris's model. (b) The proposed model.

$[C_s]_{CP}$, $[C_d]_{CP}$, and $[C_v]_{CP}$ are the compact covariance matrices of surface, double-bounce, and volume scattering, respectively. Then the compact covariance matrix can be expanded as

$$C_{\pi/4} = f_{sc} [C_s]_{CP} + f_{dc} [C_d]_{CP} + f_{vc} [C_v]_{CP}, \quad (14)$$

where f_{sc} , f_{dc} , and f_{vc} are the expansion coefficients. From (14), we have 3 equations with 5 unknowns. It is noted from (5) that, for the fully polarimetric case, we have $f_v =$

$2\langle |S_{HV}|^2 \rangle$. The backscattered energy in full polarimetry is double that of compact polarimetry. Hence, the decomposed coefficient f_{vc} is expected to be proportionally reduced. Let $f_{vc} = \langle |S_{HV}|^2 \rangle \cdot \langle |S_{HV}|^2 \rangle$ is a parameter needed to be estimated in the reconstruction. If $\langle |S_{HV}|^2 \rangle$ is retained to be determined later, then (14) can be solved in a similar way as that of three-component decomposition. When $\text{Re}(C_{12})$ is positive, we decide that surface scattering is dominant and let $\alpha = -1$. When $\text{Re}(C_{12})$ is negative, we decide that double-bounce

scattering is dominant and let $\beta = 1$. Finally, the surface scattering power P_{sc} and the double-bounce scattering power P_{dc} can be obtained as follows:

$$\begin{aligned} X &= C_{11} - 1.5f_{vc}; \\ Y &= C_{22} - 1.5f_{vc}; \\ Z &= C_{12} - 0.5f_{vc}; \\ P_{dc} &= 2 \frac{XY - |Z|^2}{X + Y + 2\text{Re}(Z)}, \quad \text{if } \text{Re}(C_{12}) > 0, \alpha = -1 \\ \text{or } P_{sc} &= 2 \frac{XY - |Z|^2}{X + Y - 2\text{Re}(Z)}, \quad \text{if } \text{Re}(C_{12}) < 0, \beta = 1. \end{aligned} \quad (15)$$

After P_{dc} or P_{sc} is obtained, for the above two cases, P_{sc} in the case $\text{Re}(C_{12}) > 0$ and P_{dc} in the case $\text{Re}(C_{12}) < 0$ can be directly obtained from $P_{sc} = \text{span}_c - P_{dc} - P_{vc}$ and $P_{dc} = \text{span}_c - P_{sc} - P_{vc}$, respectively, where $\text{span}_c = C_{11} + C_{22}$ is the total backscattered power. The volume scattering power $P_{vc} = 3f_{vc} = 3\langle |S_{HV}|^2 \rangle$ will be estimated during the iteration introduced in the next section. Note that this three-component decomposition only serves for the purpose of pseudo-quad-pol data reconstruction. It is quite different from other compact target decompositions [4, 11].

3.3. Reconstruction Algorithm. The iteration approach is employed to solve the nonlinear system [5–9]. The iteration procedure is detailed as follows.

Step 0. Initialization. Consider

$$\begin{aligned} N_{(0)} &= 4, \\ \rho_{(0)} &= \frac{C_{12}}{\sqrt{C_{11}C_{22}}}, \\ f_{vc(0)} &= (C_{11} + C_{22}) \frac{1 - \text{sg} \cdot |\rho_{(0)}|}{N_{(0)}/2 + 1 - \text{sg} \cdot |\rho_{(0)}|}. \end{aligned} \quad (16)$$

Step 1. Iteration. Consider

$$\begin{aligned} X &= C_{11} - 1.5f_{vc(i)}; \\ Y &= C_{22} - 1.5f_{vc(i)}; \\ Z &= C_{12} - 0.5f_{vc(i)}; \\ P_{dc(i)} &= 2 \frac{XY - |Z|^2}{X + Y + 2\text{Re}(Z)} \\ N_{(i+1)} &= 4 \frac{2P_{dc(i)} + 3f_{vc(i)}}{3f_{vc(i)}} \\ &\quad \text{if } \text{Re}(C_{12}) > 0 \end{aligned}$$

$$\text{or } P_{sc(i)} = 2 \frac{XY - |Z|^2}{X + Y - 2\text{Re}(Z)}$$

$$N_{(i+1)} = 4 \frac{2\text{span}_c - 2P_{sc(i)} - 3f_{vc(i)}}{3f_{vc(i)}}$$

if $\text{Re}(C_{12}) < 0$

$$\rho_{(i+1)} = \frac{C_{12} - f_{vc(i)}/2}{\sqrt{(C_{11} - f_{vc(i)}/2)(C_{22} - f_{vc(i)}/2)}}$$

$$f_{vc(i+1)} = (C_{11} + C_{22}) \frac{1 - \text{sg} \cdot |\rho_{(i+1)}|}{N_{(i+1)}/2 + 1 - \text{sg} \cdot |\rho_{(i+1)}|}, \quad (17)$$

where $\text{sg} = \text{sgn}(\text{Re}(C_{12}))$ and $i = 0, 1, 2, \dots$ is the iterations number. Given a converged value for f_{vc} , where $\langle |S_{HV}|^2 \rangle = f_{vc}$, the pseudo-quad-pol covariance matrix is estimated as

$$\begin{aligned} \mathbf{C}_{\text{pseudo-quad}} &= \begin{bmatrix} 2C_{11} - \langle |S_{HV}|^2 \rangle & 0 & 2C_{12} - \langle |S_{HV}|^2 \rangle \\ 0 & 2\langle |S_{HV}|^2 \rangle & 0 \\ 2C_{12}^* - \langle |S_{HV}|^2 \rangle & 0 & 2C_{22} - \langle |S_{HV}|^2 \rangle \end{bmatrix}. \end{aligned} \quad (18)$$

4. Experiments

In experiments, by comparing with the method proposed by Souyris et al., we validate the proposed model-based method in the following aspects: firstly, the reconstructed covariance matrix is evaluated in terms of the co- and cross-polarized elements; and secondly, several typical oil-slick indicators derived in full polarimetry are used to assess the performance of the proposed method. Souyris's method is selected for comparison mainly due to the reason that Souyris's method can also be seen as a power-weighted pseudo-quad-pol information reconstruction method. The only difference with the proposed method is that the negative or positive copolarized correlation property is considered in this study to discriminate between the surface and double-bounce scattering. Thus, the comparison results would clearly display the significance of the phase information in the improvement of reconstruction accuracy. The included fully polarimetric oil-spill indicators [1] are summarized in Table 1. Reconstruction results are shown in Table 2. From Table 2, it can be observed that the proposed method improves the reconstruction stably. In addition, this reconstruction method does not need prior fully polarimetric data to train the model parameter N .

5. Conclusion

In this study, we proposed a model-based reconstruction method for the linear $\pi/4$ compact polarimetry. By taking the negative and positive copolarized correlation properties (negative for the double-bounce dominated case and positive for the surface dominated case) into consideration,

TABLE 1: Oil-spill indicators of fully polarimetric SAR images.

Copolarized correlation coefficient	$ \rho = \left \frac{\langle S_{HH} S_{VV}^* \rangle}{\sqrt{\langle S_{HH} ^2 \rangle \langle S_{VV} ^2 \rangle}} \right $
Copolarized phase difference	$\text{CPD} = \text{angle}(\langle S_{HH} S_{VV}^* \rangle)$
Conformity coefficient	$u = \frac{2(\text{Re}(\langle S_{HH} S_{VV}^* \rangle) - \langle S_{HV} ^2 \rangle)}{\text{span}}$
Circular polarization correlation	$\text{CPC} = \left \frac{\langle S_{RR} S_{LL}^* \rangle}{\sqrt{\langle S_{RR} ^2 \rangle \langle S_{LL} ^2 \rangle}} \right , \text{ where } \begin{cases} S_{RR} = \frac{(S_{HH} - S_{VV} + 2jS_{HV})}{2} \\ S_{LL} = \frac{(S_{HH} - S_{VV} - 2jS_{HV})}{2} \end{cases}$
H, α, A	Cloude-Pottier's decomposition

TABLE 2: Mean (m.) and standard deviation (Std.) of the pseudo-quad-pol reconstruction errors for the covariance elements and the polarimetric parameters listed in Table 1. $N = 4$ indicates the results of Souyris's model.

	$\langle S_{HH} ^2 \rangle$		$\langle S_{VV} ^2 \rangle$		$\langle S_{HV} ^2 \rangle$		$ \rho $		CPD (°)	
	m.	Std.	m.	Std.	m.	Std.	m.	Std.	m.	Std.
$N = 4$	0.023	0.018	0.027	0.021	0.029	0.019	0.011	0.0175	0.861	6.544
Proposed model	0.022	0.017	0.026	0.020	0.027	0.017	0.010	0.016	0.760	5.693
	u		CPC		H		α (°)		A	
	m.	Std.	m.	Std.	m.	Std.	m.	Std.	m.	Std.
$N = 4$	0.040	0.033	0.316	0.128	0.070	0.040	0.303	1.034	0.324	0.124
Proposed model	0.360	0.028	0.290	0.122	0.065	0.036	1.190	0.857	0.330	0.124

the proposed model is generally consistent with the real polarimetric SAR data. By employing a model-based compact target decomposition scheme, the reconstruction can be implemented via an iteration approach. In experiments, reconstruction performance is evaluated in terms of both co- and cross-polarized elements and several typical polarimetric oil-spill indicators. Results showed that, by comparison with the Souyris method, the proposed method has a stable superior performance. In addition, this study investigated the capability of L -band satellite polarimetric SAR data for oil-spill observation in compact mode, which has rarely appeared in the literature. In the future, detailed works will be carried out and the extension of this method to the circular compact mode will also be fully evaluated.

Conflict of Interests

The authors declare that there is no conflict of interests regarding the publication of this paper.

Acknowledgments

This work is partly supported by NSFC under Grant no. 41171317 and by the Research Foundation of Tsinghua University under Grant no. 20111080968. The first author, Junjun Yin, is supported while carrying on her research at the University of Manitoba by the NSERC Discovery Grant no. 7400 awarded to Wooil Moon.

References

- [1] A. H. S. Solberg, "Remote sensing of ocean oil-spill pollution," *IEEE Proceedings*, vol. 100, no. 10, pp. 2931–2945, 2012.
- [2] D.-J. Kim, W. M. Moon, and Y.-S. Kim, "Application of TerraSAR-X data for emergent oil-spill monitoring," *IEEE Transactions on Geoscience and Remote Sensing*, vol. 48, no. 2, pp. 852–863, 2010.
- [3] D. L. Schuler and J.-S. Lee, "Mapping ocean surface features using biogenic slick-fields and SAR polarimetric decomposition techniques," *IEE Proceedings: Radar, Sonar and Navigation*, vol. 153, no. 3, pp. 260–270, 2006.
- [4] F. J. Charbonneau, B. Brisco, R. K. Raney et al., "Compact polarimetry overview and applications assessment," *Canadian Journal of Remote Sensing*, vol. 36, no. 2, pp. S298–S315, 2010.
- [5] J.-C. Souyris, P. Imbo, R. Fjørtoft, S. Mingot, and J.-S. Lee, "Compact polarimetry based on symmetry properties of geophysical media: the $\pi/4$ mode," *IEEE Transactions on Geoscience and Remote Sensing*, vol. 43, no. 3, pp. 634–645, 2005.
- [6] M. E. Nord, T. L. Ainsworth, J.-S. Lee, and N. J. S. Stacy, "Comparison of compact polarimetric synthetic aperture radar modes," *IEEE Transactions on Geoscience and Remote Sensing*, vol. 47, no. 1, pp. 174–188, 2009.
- [7] M. J. Collins, M. Denbina, and G. Atteia, "On the reconstruction of quad-pol sar data from compact polarimetry data for ocean target detection," *IEEE Transactions on Geoscience and Remote Sensing*, vol. 51, no. 1, pp. 591–600, 2013.
- [8] Y. Li, Y. Zhang, J. Chen, and H. Zhang, "Improved compact polarimetric SAR Quad-pol reconstruction algorithm for oil

- spill detection,” *IEEE Geoscience and Remote Sensing Letters*, vol. 11, no. 6, pp. 1139–1142, 2014.
- [9] J. Yin and J. Yang, “Multi-polarization reconstruction from compact polarimetry based on modified four-component scattering decomposition,” *Journal of Systems Engineering and Electronics*, vol. 25, no. 3, Article ID 6850218, pp. 399–410, 2014.
- [10] J. Yin, J. Yang, Z.-S. Zhou, and J. Song, “The extended bragg scattering model-based method for ship and oil-spill observation using compact polarimetric SAR,” *IEEE Journal of Selected Topics in Applied Earth Observations and Remote Sensing*, 2014.
- [11] S. R. Cloude, D. G. Goodenough, and H. Chen, “Compact decomposition theory,” *IEEE Geoscience and Remote Sensing Letters*, vol. 9, no. 1, pp. 28–32, 2012.
- [12] M. Migliaccio, A. Gambardella, F. Nunziata, M. Shimada, and O. Isoguchi, “The PALSAR polarimetric mode for sea oil slick observation,” *IEEE Transactions on Geoscience and Remote Sensing*, vol. 47, no. 12, pp. 4032–4041, 2009.
- [13] J. S. Lee and E. Pottier, *Polarimetric Radar Imaging: From Basics to Applications*, vol. 143 of *Optical Science and Engineering Series*, chapter 6, CRS Press, 2008.
- [14] E. Pottier and S. R. Cloude, “Application of the H/A/ α polarimetric decomposition theorem for land classification,” in *Wide-band Interferometric Sensing and Imaging Polarimetry*, vol. 3120 of *Proceedings of SPIE*, pp. 132–143, San Diego, Calif, USA, July 1997.
- [15] A. Freeman, “Fitting a two-component scattering model to polarimetric SAR data from forests,” *IEEE Transactions on Geoscience and Remote Sensing*, vol. 45, no. 8, pp. 2583–2592, 2007.

Research Article

Monitoring of Damage in Sunflower and Maize Parcels Using Radar and Optical Time Series Data

György Surek and Gizella Nádor

Institute of Geodesy, Cartography and Remote Sensing, Bosnyák tér 5, Budapest 1149, Hungary

Correspondence should be addressed to Gizella Nádor; nador.gizella@fomi.hu

Received 26 December 2014; Accepted 24 April 2015

Academic Editor: Jian Yang

Copyright © 2015 G. Surek and G. Nádor. This is an open access article distributed under the Creative Commons Attribution License, which permits unrestricted use, distribution, and reproduction in any medium, provided the original work is properly cited.

The objective of this paper is to monitor the temporal behaviour of geometrical structural change of cropland affected by four different types of damage: weed infection, Western Corn Rootworm (WCR), storm damage, and drought by time series of different type of optical and quad-pol RADARSAT2 data. Based on our results it is established that ragweed infection in sunflower can be well identified by evaluation of radar (mid-June) and optical (mid-August) satellite images. Effect of drought in sunflower is well recognizable by spectral indices derived from optical as well as “ I ”-component of Shannon entropy (SE_I) from radar satellite images acquired during the first decade of July. Evaluation of radar and optical satellite images acquired between the last decade of July and mid-August proven to be the most efficient for detecting damages in maize fields caused by either by WCR or storm. Components of Shannon entropy are proven to have significant role in identification. Our project demonstrates the potential in integrated usage of polarimetric radar and optical satellite images for monitoring several types of agricultural damage.

1. Introduction

Polarimetric characteristics of various crop types have been studied by a number of authors [1–3]. According to them these features depend on numerous properties of the reflecting surface element (e.g., surface reflectivity, water content, and roughness) particularly on the geometric structure of plants. Consequently, the polarimetric features can be applied for assessment of crop condition, identification of crop types, and phenological phases of crops [4–7]. This paper presents how damage may modify a plant’s response to polarimetric radar beam. The objective is to determine whether optical and SAR time series can detect damage-induced spatial and temporal changes in crop structure.

Damage induces changes in spectral and geometric features of croplands. Therefore, the most efficient way of identification of this damage can be to coevaluate optical and polarimetric radar satellite images. Previous results of our survey on this subject have already been presented on several publications [8–10].

The objective of our investigation (presented in this paper) was to monitor the temporal structural changes of cropland affected by weed infection, WCR, and storm damage as well as drought in some study areas in Hungary by the integrated use of time series of optical and radar data. The temporal behaviour of 4 different types of damage has been surveyed, carried out on 3 distinct sample areas (Csongrád, Békés, and Baranya).

Effects of weed infection in sunflower had been examined over Baranya site. Weed infection generates discontinuities in regular geometry of row-sown crop cultivars. Figure 1 presents the difference between geometric structure of weed-infected and healthy sunflower parcels.

For Csongrád site drought-caused geometric changes in sunflower parcels had been examined and set against healthy sunflower fields. Figure 2 illustrates the differences in geometric structure of these two states in sunflower parcels.

As for Békés site, we examined two different types of damage occurring in corn fields, assessed in 2 different dates. Larvae of Western Corn Rootworm (WCR) attack the root

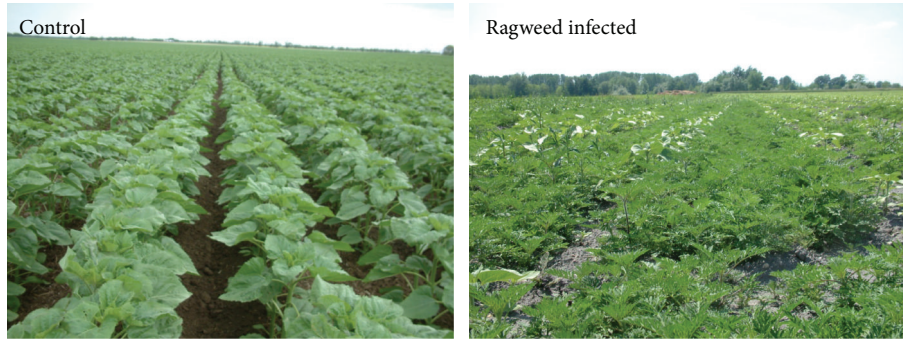


FIGURE 1: Demonstration of the difference between the geometric structure of ragweed infected and control (weed-free) sunflower fields.



FIGURE 2: Demonstration of the difference between geometric structure of control and drought stressed sunflower fields.



FIGURE 3: Geometric structure of WCR/storm damaged corn fields compared to the healthy ones (control) corn fields.

of the plant, which engender individual corn stems tumble; hence the parcel shows a rather bruised scenery. Figure 3 illustrates the scenic difference between the geometric structure of the damaged corn field and control one. Heavy storms may have similar effects on corn, although in that case stems lean according to wind direction. In both cases, geometric structure of corn field suffers appreciable changes, showing considerable differences compared to control parcels on which corn stems standing up orderly.

This paper presents the results of coevaluation of multitemporal RADARSAT-2 (standard quad-pol) and optical satellite images regarding to the abovementioned damage.

2. Materials and Methods

This paragraph presents the study areas selected, the data used (satellite and reference data), and methodology applied.

2.1. Study Areas. Our survey was applied to three distinct study areas: Csongrád, Baranya, and Békés sites (Figure 4).

Csongrád site, located between the river Tisza and the Danube, can be characterized by small-size parcels (its average parcel size is 1–5 hectares), sandy soils with poor water holding capacity; therefore the area is extremely sensitive to drought.

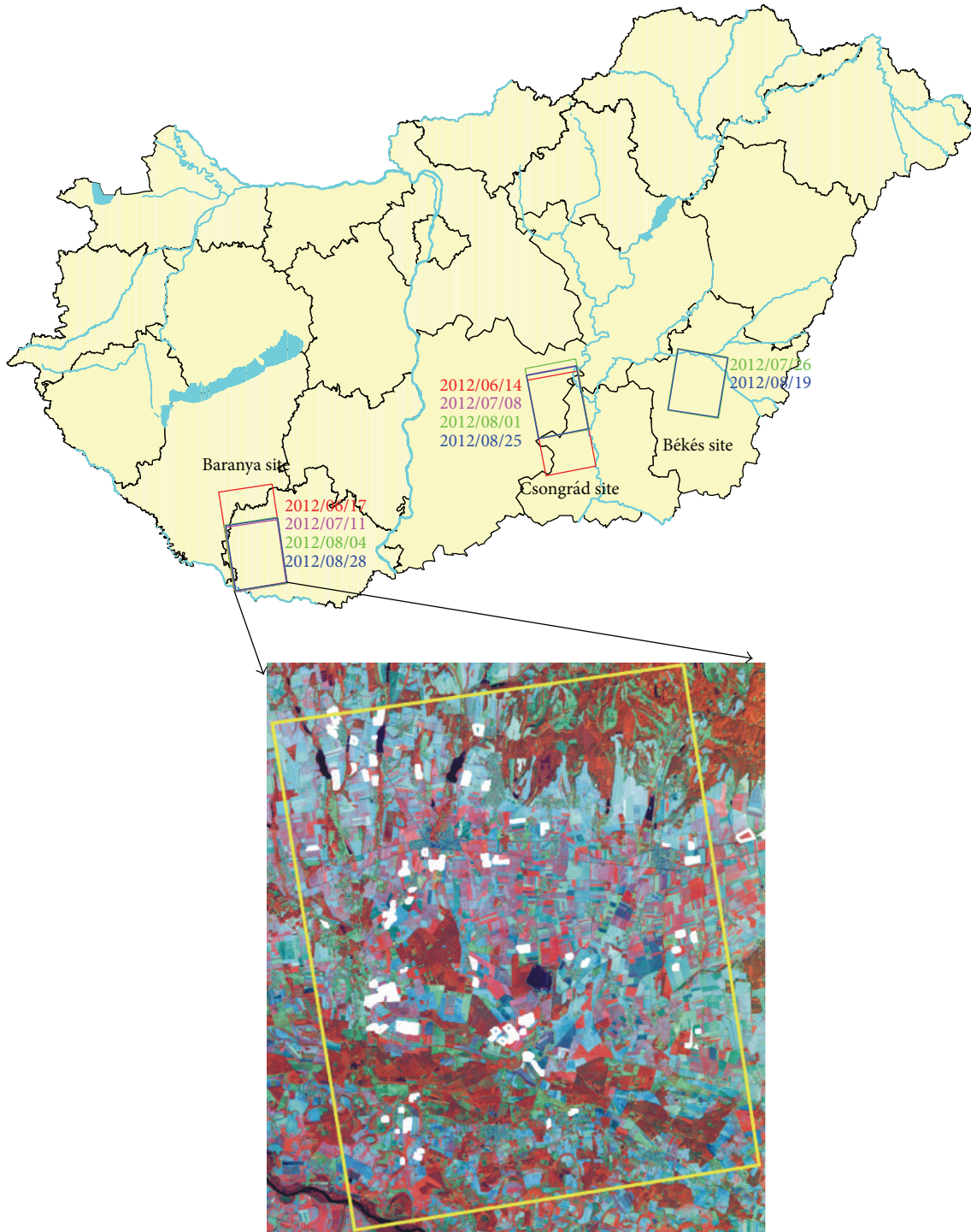


FIGURE 4: The location of the study areas and coverage of radar satellite images and location of reference parcels for Baranya site on SPOT5 (20/08/2012, R: NIR, G: SWIR, B: Red) satellite image composite.

Baranya site, located on the southern part of Transdanubia, has medium-size parcels (20–30 hectares). The area, sunflower in particular, is extremely infected by ragweed and numerous other types of weeds.

Békés site is located in the south-eastern part of the Hungarian Great Plain. Its average parcel-size takes 40–50 hectares. As being one of the most important corn-producing

areas with maize monoculture, it opens the door to the spreading of WCR. The area was hit by serious storms several times in 2012. We analyzed the effects of storm which occurred on July 7, 2012.

2.2. *Data Used.* Coverage of satellite images and position of sample areas are presented on Figure 4.

TABLE 1: Data applied for Csongrád site.

Acquisition date RADARSAT2	Date of field survey	Optical satellite images and acquisition date
14/6/2012	14-15/06/2012	Landsat TM7 18/06/2012
8/7/2012	3-5/07/2012	Landsat TM7 04/07/2012, Geoeye: 30/06/2012, IRS-R2 AWiFS: 03/07/2012
1/8/2012	—	Landsat TM7 20/07/2012, SPOT5 29/07/2012, Landsat TM7 05/08/2012
25/8/2012	26/09/2012	SPOT5 19/08/2012, Landsat TM7 21/08/2012

TABLE 2: Data applied for Baranya site.

Acquisition date of RADARSAT2	Date of field survey	Optical satellite images and acquisition date
17/6/2012	17/6/2012	IRS-R2 LISS III 1/5/2012 Landsat TM7 31/5/2012 Landsat TM7 16/6/2012
11/7/2012	3-4/7/2012	IRS-P6 LISS III: 30/6/2012, Landsat TM7 02/7/2012, Landsat TM7 11/7/2012
4/8/2012	—	SPOT4: 28/7/2012, Landsat TM7 3/8/2012, IRS-R2 LISS III 5/8/2012
28/8/2012	24-26/9/2012	Landsat TM7 19/08/2012, SPOT5 20/08/2012, Landsat TM7 28/08/2012, IRS-P6 LISS III 10/09/2012

TABLE 3: Data applied for Békés site.

Acquisition date of RADARSAT2	Date of field survey	Optical satellite images and acquisition data
26/7/2012	6-8/8/2012	Landsat TM7 13/7/2012, Landsat TM7 20/7/2012, SPOT4 29/7/2012, IRS-P6 LISS III 8/8/2012
19/8/2012	—	Landsat TM7 14/8/2012, SPOT5 19/8/2012, Landsat TM7 30/8/2012

Features of the applied optical and radar satellite images (acquisition data, date of ground reference data collection, and other characteristics) are shown in Tables 1–3. Tables 4–9 contain the characterisation of the optical radar satellite images applied for the examinations. Each of the radar satellite images is coupled with optical satellite images acquired nearly at the same time. Although we tried our best, we did not always succeed in collecting ground reference data at the same time.

Reference data was collected from weed-infected sunflower parcels, WCR and storm damaged maize parcels, and sunflower parcels hit by drought. Control data was collected from correspondent healthy parcels as well. Results of reference data collecting are given in Tables 10–12.

TABLE 4: Characterisation of optical satellite images applied for Csongrád site.

Acquisition date	Satellite	Spatial resolution (m)	Spectral resolution
29/04/2012	IRS-P6 LISS III	20	Green, red, NIR, SWIR
01/05/2012	Landsat TM7	30	Blue, green, red, NIR, SWIR1, SWIR2
11/05/2012	IRS-R2 AWiFS	50	Green, red, NIR, SWIR
18/06/2012	Landsat TM7	30	Blue, green, red, NIR, SWIR1, SWIR2
30/06/2012	GEOEYE	0.5	Blue, green, red, NIR
01/07/2012	IRS-P6 AWiFS	50	Green, red, NIR, SWIR
03/07/2012	IRS-R2 AWiFS	50	Green, red, NIR, SWIR
04/07/2012	Landsat TM7	30	Blue, green, red, NIR, SWIR1, SWIR2
20/07/2012	Landsat TM7	30	Blue, green, red, NIR, SWIR1, SWIR2
29/07/2012	SPOT5	10	Green, red, NIR, SWIR
05/08/2012	Landsat TM7	30	Blue, green, red, NIR, SWIR1, SWIR2
05/08/2012	IRS-R2 AWiFS	50	Blue, green, red, NIR, SWIR1, SWIR2
19/08/2012	SPOT5	10	Green, red, NIR, SWIR
21/08/2012	Landsat TM7	30	Blue, green, red, NIR, SWIR1, SWIR2
06/10/2012	IRS-R2 AWiFS	50	Green, red, NIR, SWIR

2.3. Presentation of the Damages Examined. This paragraph describes the main effects of the various damage impacts. On Figures 5–7 we used special band combinations for colour composite to emphasize the difference between damaged and control areas.

2.3.1. Sunflower Hit by Drought. Figure 5 represents a typical sunflower parcel hit by drought (delineated by brown) contrarily to a healthy one (delineated by green) visualized on optical satellite image composite (Geoeye 30/6/2012, R: NIR, G: red, B: blue) and on radar data composite (RADARSAT2 8/7/2012, R: SE, G: SE_i, B: I3) as well.

Difference between the sunflower parcels can be well discernible on photos taken on the spot. As sunflowers hit by drought have sagging leaves, they cannot cover the soil completely, whilst leaves of healthy sunflower are horizontal and cover the entire soil surface.

Difference can be well identified on both optical and radar satellite composites. Healthy sunflower parcel appears orange on optical images, unlike those hit by drought showing bluish tinge which is typical to bare soil.

TABLE 5: Characterisation of radar satellite images applied for Csongr ad site.

Acquisition date	Satellite	Spatial resolution (m)	Polarisation	Wavelength (cm)	Incidence angle (�)	Beam	Pass
14/06/2012	RADARSAT2	20	Quad-pol	5.6	37.4–38.9	SQ18	Ascending
08/07/2012	RADARSAT2	20	Quad-pol	5.6	37.4–38.9	SQ18	Ascending
01/08/2012	RADARSAT2	20	Quad-pol	5.6	37.4–38.9	SQ18	Ascending
25/08/2012	RADARSAT2	20	Quad-pol	5.6	37.4–38.9	SQ18	Ascending

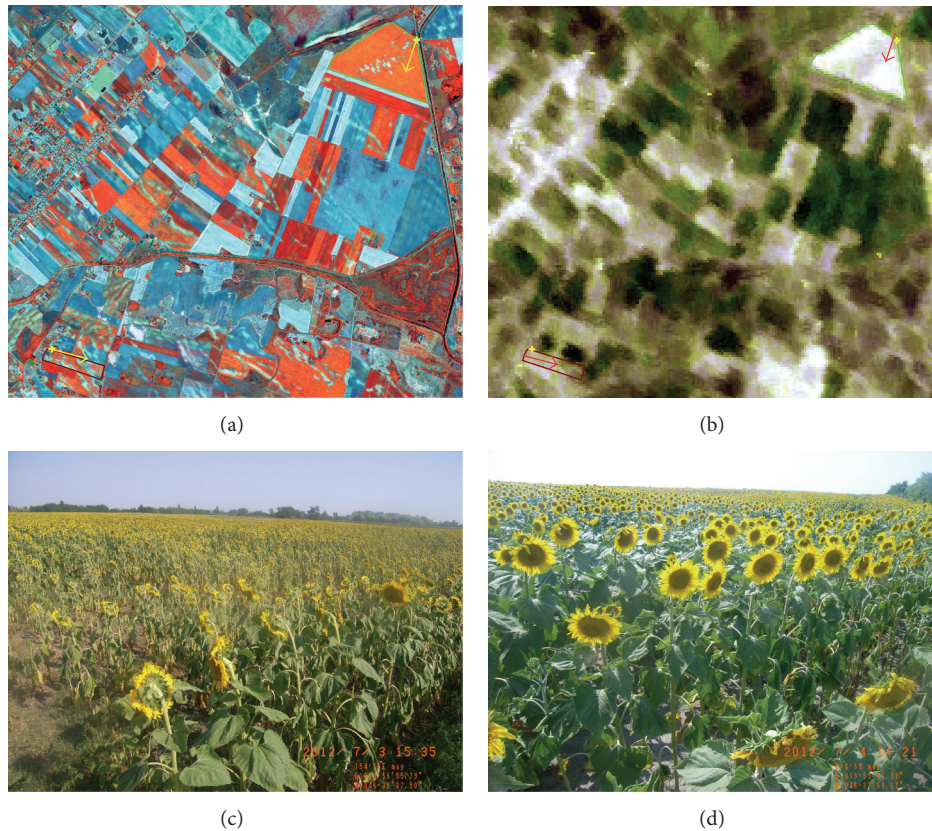


FIGURE 5: Sunflower hit by drought (marked by brown polygon) and control (marked by green polygon) sunflower fields on Geoeye (30/6/2012, R: NIR, G: red, B: blue) (a) and RADARSAT2 (8/7/2012, R: SE, G: SE₇, B: l3) satellite image composites (b) and photos taken on ground survey (3–5/07/2012) (c, d): sunflower hit by drought (c), control sunflower (d). Direction of the photos taken is shown by arrows.

On radar images appearance of healthy sunflower can be described with intense light colors, whilst damaged parcels are greenish-gray.

2.3.2. Appearance of Weed Infection in Sunflower Parcels. Figure 6 represents a typical sunflower parcel infected by weed (delineated by brown colour) contrarily to a control, weed-free one (delineated by green) visualized on optical satellite image composite (IRS-P6 LISS 30/6/2012, R: NIR, G: red, B: blue) and on radar data composite (RADARSAT2 17/06/2012, R: YAM_{odd}, G: SE, B: l2) as well, accompanied by photos taken on the spot on July 3 and 4, 2012.

Difference between these two sunflower parcels can be well discernible on photos. As weed-infected sunflower is less developed, weed and soil are usually revealed between

the rows of plants, while leaves of healthy sunflower stand horizontal, covering the soil surface fully, making it invisible from above.

Difference can be well identified on radar satellite composite (17/6/2012), while it cannot be observed on the optical scene acquired on June 30, 2012.

2.3.3. WCR and Storm Damage in Maize Parcels. A typical maize parcel attacked by Western Corn Rootworm (delineated by brown colour) and another damaged by storm (delineated by blue), contrarily to a healthy one (delineated by green) are visualized on optical satellite image composites (a; SPOT4 29/06/2012, R: NIR, G: SWIR, B: red) (b; SPOT5 19/08/2012, R: NIR, G: SWIR, B: red), on radar data composites RADARSAT2 (26/07/2012, 19/08/2012, R: SE_p, G: SE_t,

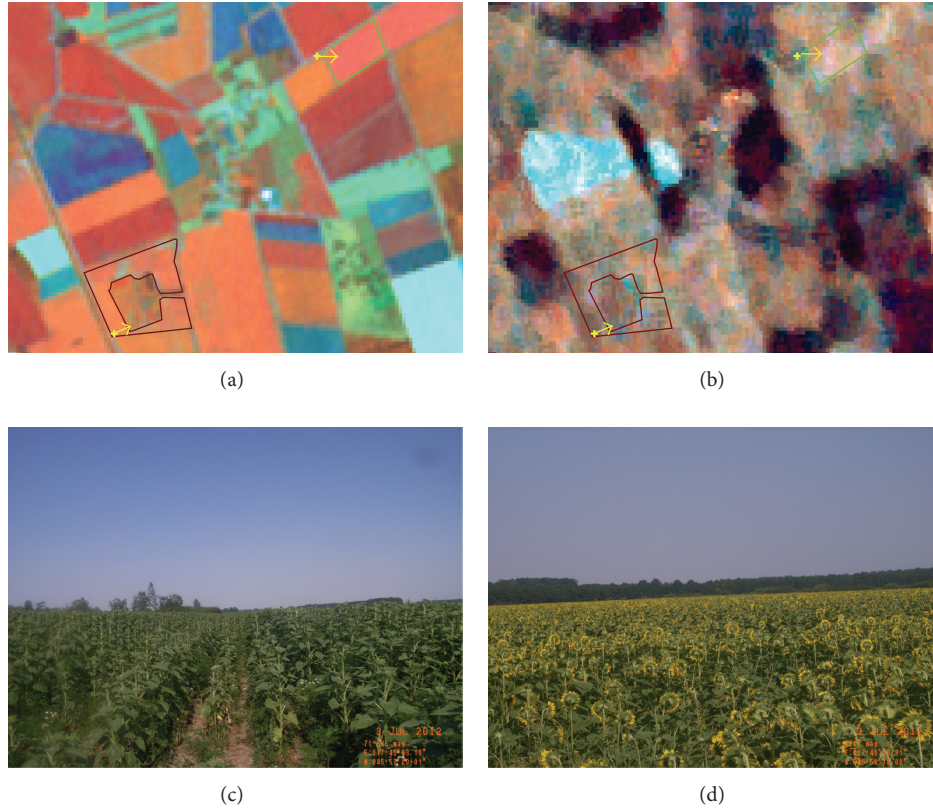


FIGURE 6: Weed-infected (brown polygon) and control (green polygon) sunflower fields on IRS-P6 LISS (30/06/2012, R: NIR, G: SWIR, B: red) (a) and RADARSAT2 (17/06/2012, R: YAM_{odd} , G: SE, B: I2) satellite image composites (b) and photos taken on ground survey (3-4/7/2012) (c, d): weed-infected sunflower (c), control sunflower (d). Direction of the photos taken is shown by arrows.

B: I1) and photos taken on the spot (06–08/08/2012) as well (Figure 7).

State of maize is obvious on the photos taken on the spot. WCR damaged maize parcel with its stems leaned to each other randomly shows a rather disordered scenery. Contrarily, all the stems on maize parcel damaged by storm leaned according to wind direction, whilst control maize parcel looks well structured.

Difference between the three parcels can be detected on optical satellite composites acquired on 29/07/2012 and 19/08/2012, particularly in case of parcels damaged by storm. Difference between the 3 parcels is similarly apparent on the radar composite 26/07/2012, while no significant distinction appears any more on the radar composite 19/08/20.

2.4. Methodology Applied. Steps of preprocessing of optical satellite images are as follows:

- (i) import,
- (ii) geometric correction,
- (iii) radiometric correction (ToA reflectance calculation),
- (iv) generation of spectral indices (NDVI, NSI),
- (v) intercalibration of spectral indices.

The spectral indices applied for our study were calculated from ToA reflectance instead of using surface reflectance; consequently these indices are not comparable between different years.

Reference fields' spectral index features Normalized Difference Vegetation Index (NDVI) and normalized special index (NSI) derived from optical images (SPOT4/5, Landsat TM7, IRS-P6/R2 LISS III, IRS-P6 AWiFS) are calculated from radiometric calibrated ToA reflectance values.

Definition of these indices is shown by

$$NDVI = 100 * \frac{NIR - RED}{NIR + RED}, \quad (1)$$

$$NSI = 100 * \frac{SWIR - NIR}{NIR - RED},$$

where NIR is the ToA reflectance in near infrared band, RED is the ToA reflectance in red band, and SWIR is the ToA reflectance in short wave infrared band.

The vegetation index, NDVI, describes the state and growth of vegetation, while NSI, based on our survey, serves characterization of spectral changes occurring in damaged fields. The different types of satellite images were intercalibrated, illustrated by Figure 8.

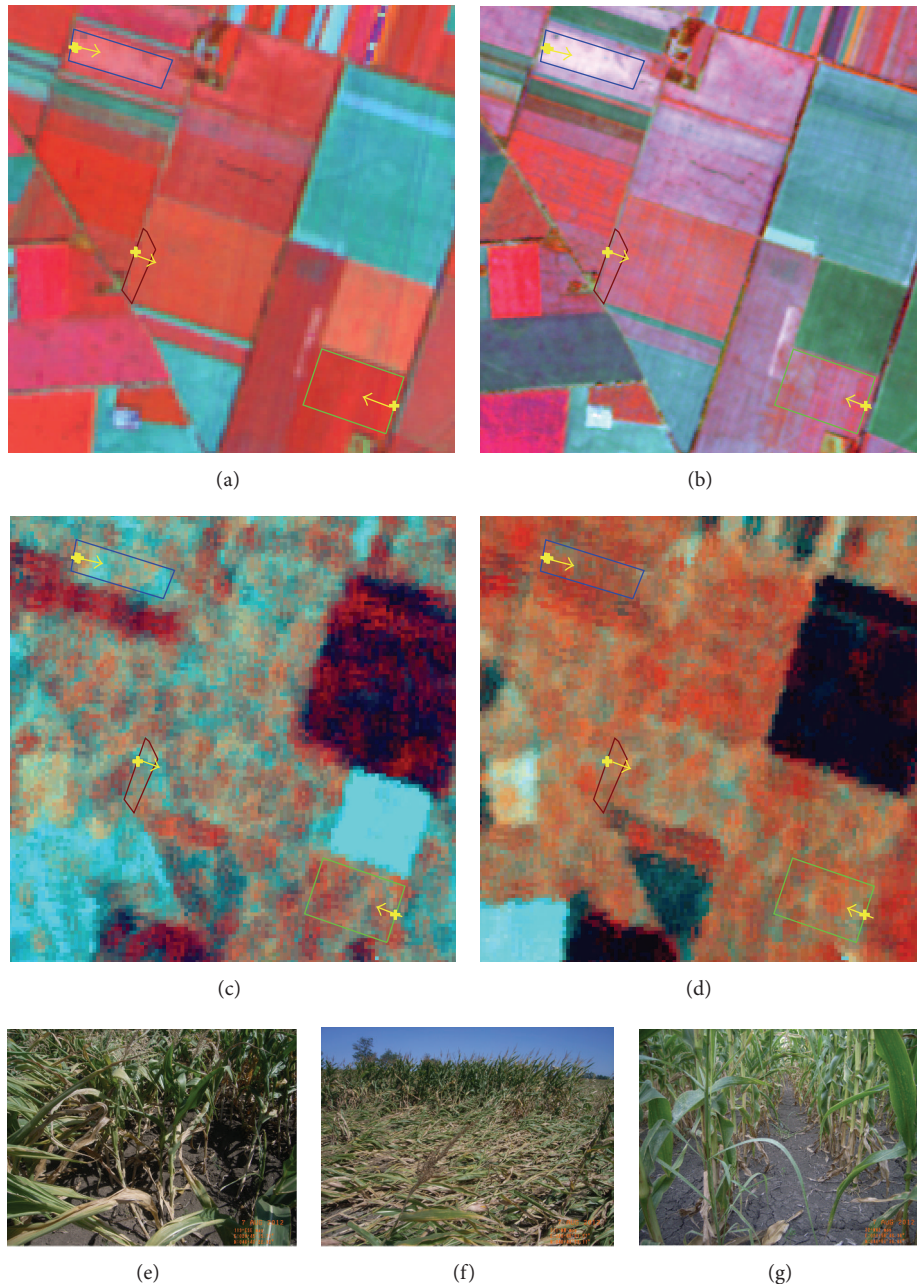


FIGURE 7: WCR-infected (brown polygon), storm (blue polygon) damaged, and control (green quadrangle) maize fields on SPOT4 (29/07/2012, R: NIR, G: SWIR, B: red) (a), SPOT5 (19/08/2012, R: NIR, G: SWIR, B: red) (b) optical and RADARSAT2 (26/07/2012, 19/08/2012, R: SE_p , G: SE_i , B: ll) (c, d) radar satellite image composites and photos taken on ground survey (6–8/08/2012) (e, f, g): WCR-infected (e), storm damaged (f), and control parcels (g). Direction of the photos taken is shown by arrows.

The well-known Landsat TM7 discontinuity (striping) errors were managed by intercalibrated spectral index derived from IRS P6/R2 AWiFS images having nearly similar acquisition date.

Preprocessing steps of RADARSAT2 data and radar features (assigned by light yellow) applied for our study are shown on Figure 9.

Calibrated backscattering coefficients (Σ_0) of standard quad-pol RADARSAT2 data were calculated by using

NEST software. Polarimetric descriptors of these data were calculated by using PolSpro software. Their definitions are described at [11]. Each of these types of software was developed by ESA. Two different types of decompositions (H/A/Alpha and Yamaguchi) and polarimetric features derived from those have been applied in our survey.

In our study the so called Shannon entropy based on H/A/Alpha decomposition of the coherency matrix [12] is one of the most important polarimetric descriptors. Natural

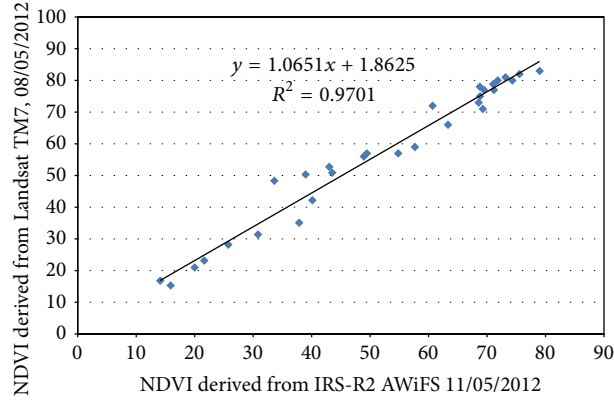


FIGURE 8: Intercalibration of NDVI values derived from IRS-R2 AWiFS and Landsat TM7.

TABLE 6: Characterisation of optical satellite images applied for Baranya site.

Acquisition date	Satellite	Spatial resolution (m)	Spectral resolution
01/05/2012	IRS-R2 LISS III	20	Green, red, NIR, SWIR
11/05/2012	IRS-R2 AWiFS	50	Green, red, NIR, SWIR
31/05/2012	Landsat TM7	30	Blue, green, red, NIR, SWIR1, SWIR2
16/06/2012	Landsat TM7	30	Blue, green, red, NIR, SWIR1, SWIR2
30/06/2012	IRS-P6 LISS III	20	Green, red, NIR, SWIR
02/07/2012	Landsat TM7	30	Blue, green, red, NIR, SWIR1, SWIR2
03/07/2012	IRS-R2 AWiFS	50	Green, red, NIR, SWIR
11/07/2012	Landsat TM7	30	Blue, green, red, NIR, SWIR1, SWIR2
28/07/2012	SPOT4	20	Green, red, NIR, SWIR
03/08/2012	Landsat TM7	30	Blue, green, red, NIR, SWIR1, SWIR2
05/08/2012	IRS-R2 LISS III	20	Green, red, NIR, SWIR
19/08/2012	Landsat TM7	30	Blue, green, red, NIR, SWIR1, SWIR2
20/08/2012	SPOT5	10	Green, red, NIR, SWIR
28/08/2012	Landsat TM7	30	Blue, green, red, NIR, SWIR1, SWIR2
10/09/2012	IRS-P6 LISS III	20	Green, red, NIR, SWIR

or agricultural damage often causes physical and visible disorders within the parcels. They can be characterized as follows:

the polarization status of the transmitted and received pulses is known. The degree of polarization is influenced by the target. The so-called Shannon entropy (SE) can describe the ratio of “polarization scattering” above. Shannon entropy [13, 14] consists of two components:

$$SE = SE_i + SE_p, \quad (2)$$

where SE is intrinsic degrees of coherence and SE_p is degrees of polarization.

Further important descriptors involved in our study are the components of Yamaguchi decomposition of the coherency matrix [15–17]. This type of decomposition technique can be applied for identification of scattering targets. It can account for the strength of different scattering mechanisms. Their components applied in this study are as follows: YAM_{odd} for single scattering, YAM_{dbl} for double bounce scattering, and YAM_{vol} for volume scattering.

Efficiency and accuracy of these features were evaluated by statistical comparative analysis of reference crop fields. Based on the damaged (weed-infected, drought, WCR, or storm) and the healthy reference fields we analyzed the separability (significance) of the polarimetric descriptors of radar images mentioned above. Polarimetric descriptors of the reference fields are supposed to show normal distribution, so we derived the significance, t value calculated by the Welch test [18], and ranked the descriptors according to that. The Welch test is applicable here. The null hypothesis is the averaged values characterizing that damaged and control areas are equal.

Figure 10 shows the methodology applied. It is important to note that time series of radar and optical data have an equally significant role in identification of damage. Polarimetric descriptors derived from radar data contain a wide range of information. However they require adequate interpretation for each case. Therefore, we have to identify the crop type by the time series of optical satellite data. Interpretation of radar data should be implemented only for the mask generated based on the selected crop types. After

TABLE 7: Characterisation of radar satellite images applied for Baranya site.

Acquisition date	Satellite	Spatial resolution (m)	Polarisation	Wavelength (cm)	Incidence angle (°)	Beam	Pass
17/06/2012	RADARSAT2	20	Quad-pol	5.6	41.0–42.4	SQ22	Ascending
11/07/2012	RADARSAT2	20	Quad-pol	5.6	41.0–42.4	SQ22	Ascending
04/08/2012	RADARSAT2	20	Quad-pol	5.6	41.0–42.4	SQ22	Ascending
28/08/2012	RADARSAT2	20	Quad-pol	5.6	41.0–42.4	SQ22	Ascending

TABLE 8: Characterisation of optical satellite images applied for Békés site.

Acquisition date	Satellite	Spatial resolution (m)	Spectral resolution
03/07/2012	IRS-P6 LISS III	20	Green, red, NIR, SWIR
13/07/2012	Landsat TM7	30	Blue, green, red, NIR, SWIR1, SWIR2
29/07/2012	SPOT4	20	Green, red, NIR, SWIR
29/07/2012	Landsat TM7	30	Blue, green, red, NIR, SWIR1, SWIR2
08/08/2012	IRS-P6 LISS III	20	Green, red, NIR, SWIR
14/08/2012	Landsat TM7	30	Blue, green, red, NIR, SWIR1, SWIR2
19/08/2012	SPOT5	10	Green, red, NIR, SWIR

that, only one question has to be answered: whether the plant given is damaged or not.

3. Results and Discussion

3.1. Drought in Sunflower Fields, Csongrád Site. Figure 11 shows temporal progress of sunflower's average crop development curve derived from time series of optical satellite data, referred to as control parcels and parcels hit by drought. Horizontal lines stand for indicating standard deviation referring to each of the acquisition dates. The most significant difference takes place in the first decade of July. Difference decreases gradually by the first decade of August and then disappears. Therefore, it can be established that from the beginning of August, healthy and arid sunflower parcels are no longer separable by optical satellite images.

The temporal behaviour of NSI values (Figure 12) is reverse of NDVI.

Figure 13 shows the temporal development of sigma0 values of different polarization bands. In all bands the sigma0 values are lower in case of hit by drought. The higher difference between control and hit by drought areas is at the beginning of July in all bands particularly in HV one.

Figure 14 represents the separation of ellipses featured by control and hit-drought areas in two-dimensional space of sigma0 bands. We can see well the distinguishing is highest at

the beginning of July like in Figure 11. The ellipses of controls are significantly upper-right at all dates. We can see similar distinguishing in H-Alpha space (Figure 15).

Figure 16 shows the result of separability analysis of polarimetric descriptors derived from RADARSAT2 satellite images acquired at different dates regarding reference sunflower parcels hit by drought and control ones. The one acquired on 8/7/2012 proved to be the most efficient in distinction. Although in case of each of the four acquisitions there exist such polarimetric descriptors which can distinguish these two states significantly.

It can be seen as well that not the same polarimetric descriptors show the highest efficiency at the dates given. Table 13 shows the ranking of polarimetric descriptors based on efficiency of separability or level of significance. It can be established that during the period of June to August components of Yamaguchi decomposition (mainly YAM_{vol} and YAM_{odd}) have notable role in distinguishing between sunflower parcels hit by drought and the control ones.

It is worth mentioning that component of “vol” is the one showing the most significant deviation (P value < 0.001) between July 8 and August 1, while the “odd” one has that in mid-June and end of August. It means that distinguishing these two states is dominated by volumetric scattering during the middle of the growing season (July-August), while single scattering has more important role at the beginning and end of the growing season (mid-June and August).

By evaluating both the optical and radar satellite time series data it can be established that the first decade of July is the most suitable date for distinguishing the sunflower parcels hit by drought from the control ones. According to Figure 17 those pixels of sunflower were identified as hit by drought, whose NDVI was less than 52 and $l3$ was less than 0.035.

The drought map was derived from Landsat TM7 (4/7/2012), from RADARSAT2 (8/7/2012) and from using both of them (Figure 18). The accuracy of these maps validated by reference data was almost the same (Figure 19).

3.2. Weed Infection in Sunflower Fields, Baranya Site. Figure 20 shows temporal progress of sunflower's average NDVI curve derived from time series of optical satellite data, referred to as the control (weed-free) parcels and parcels infected by weed. Horizontal lines indicate standard deviation referred to as each of the acquisition dates. In July deviation decreases appreciable while in August it starts to increase again. The largest deviation takes place in 2nd half

TABLE 9: Characterisation of radar satellite images applied for Békés site.

Acquisition date	Satellite	Spatial resolution (m)	Polarisation	Wavelength (cm)	Incidence angle (°)	Beam	Pass
26/07/2012	RADARSAT2	20	quad-pol	5.6	35.4–37.0	SQ16	Descending
19/08/2012	RADARSAT2	20	quad-pol	5.6	35.4–37.0	SQ16	Descending

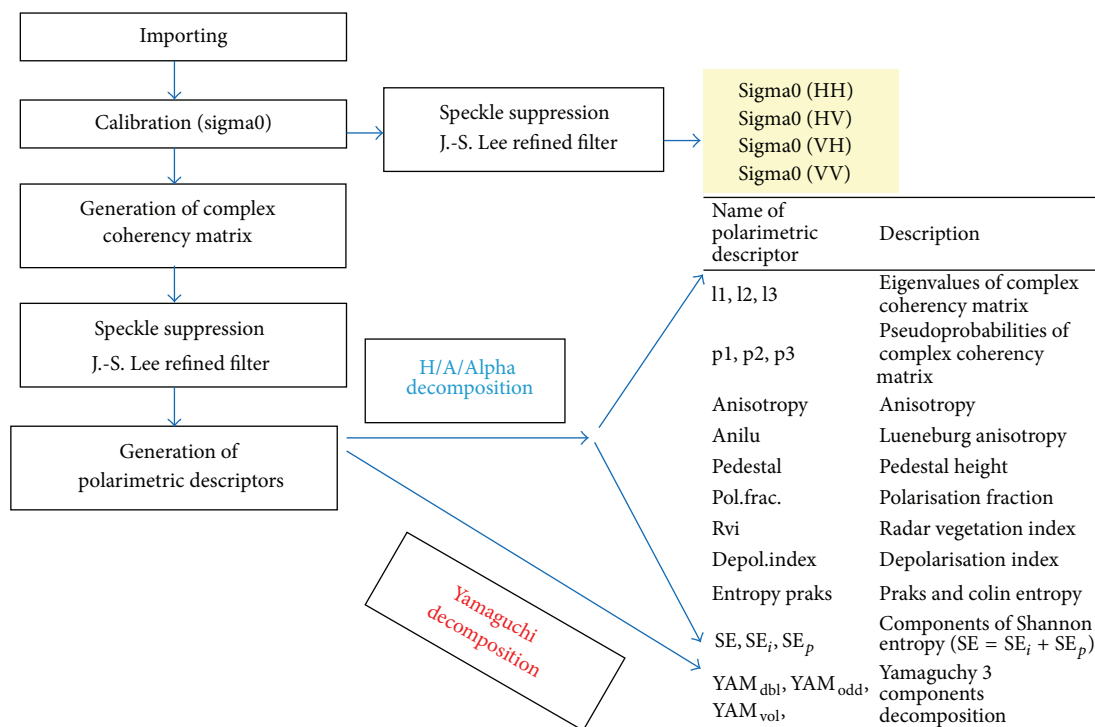


FIGURE 9: Preprocessing of RADARSAT2 satellite data and radar features applied for our study.

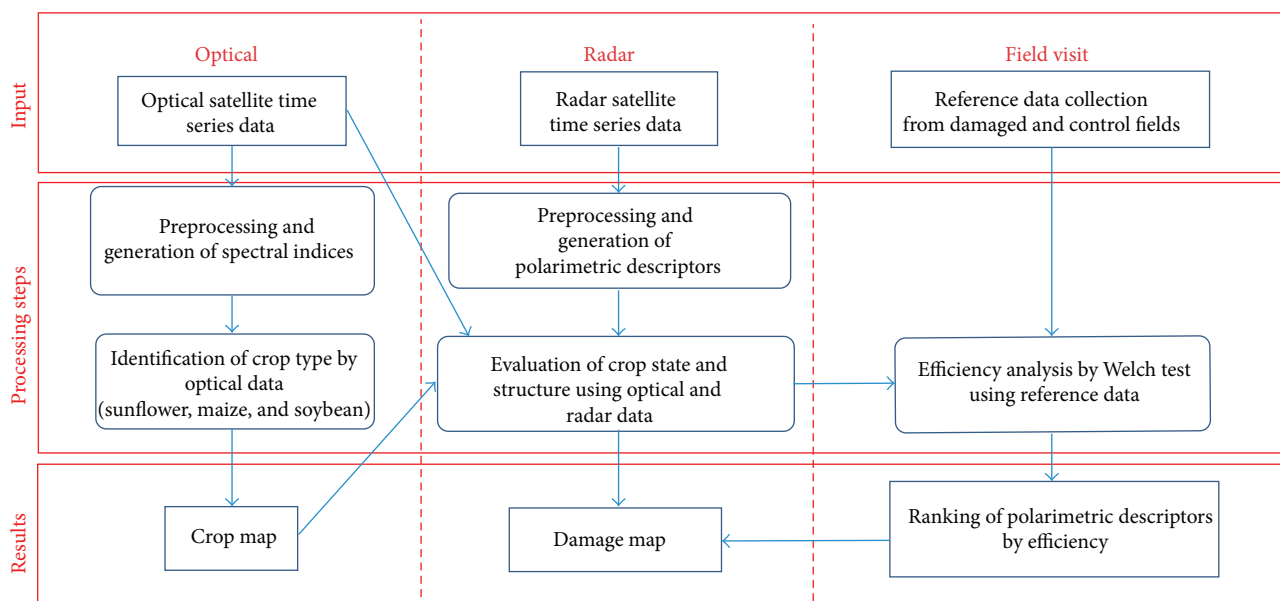


FIGURE 10: Sketch of methodology applied.

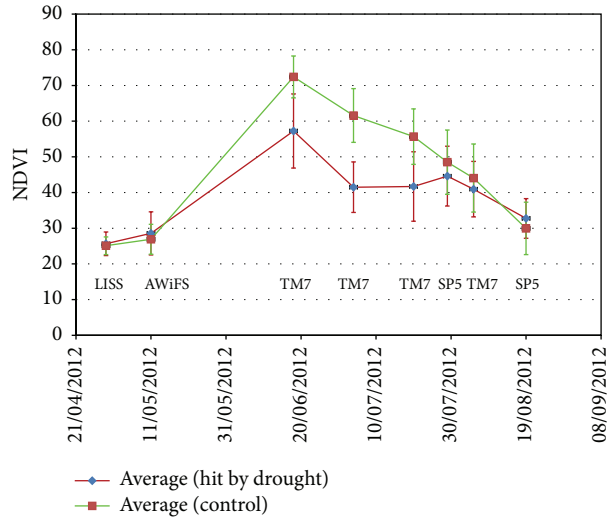


FIGURE 11: Average crop development curve based on NDVI values derived from time series of optical satellite data for sunflower hit by drought and control fields, Csongrád site. Vertical lines represent single standard deviation.

TABLE 10: Characterization of reference sunflower fields, Csongrád site.

Time period	Control		Hit by drought		Total	
	#field	Area (ha)	#field	Area (ha)	#field	Area (ha)
14-15/6/2012	5	79			5	79
3-5/7/2012	34	103	8	31.4	42	134
26/9/2012	5	11.8			5	12
Total	44	194	8	31	52	225

TABLE 11: Characterization of reference sunflower fields, Baranya site.

Time period	Weed-free		Weed-infected		Total	
	#field	Area (ha)	#field	Area (ha)	#field	Area (ha)
17/6/2012	2	18			2	18
3-7/7/2012	17	204	10	80	27	284
24-26/9/2012	11	67	13	51	24	118
Total	30	289	23	131	53	420

of August. Therefore, it can be established that optical images acquired during that period are the most suitable for sorting out infected sunflower parcels from the control ones.

From Figures 20 and 21 we can see the NSI values have reverse behaviour as NDVI similar to the case above. The difference between weed-infected and weed-free areas is highest at end of August.

Figure 22 shows the temporal variation of sigma0 in different polarization cases weed-infected and weed-free areas. The graphs are similar in all polarization bands. The backscattered intensity of weed-infected and weed-free areas is changing at beginning of August. The weed-free is higher earlier and the weed-infected increased later. The highest difference between weed-free and weed-infected areas is at

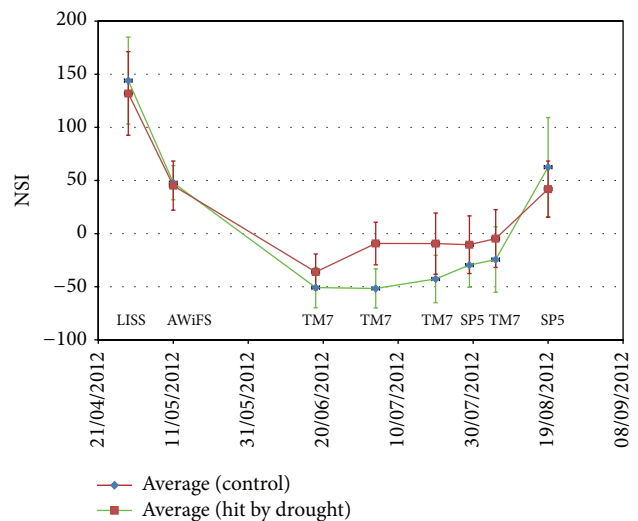


FIGURE 12: Average crop development curve based on NSI values derived from time series of optical satellite data for sunflower hit by drought and control fields, Csongrád site. Vertical lines represent single standard deviation.

mid-June in particularly co-pol. bands. The trend of Shannon entropy (SE) is very similar (Figure 23).

The separability is well seen in the two-dimensional space of sigma0 co-pol. bands and H-Alpha bands too (Figures 24 and 25).

We have very interesting results from analysis above. We can find the weed-infected sunflower areas at mid-June by radar features. While we can distinguish the weed-infected areas by optical images only two months later, at the end of August.

Figure 26 represents the result of separability analysis of polarimetric descriptors derived from multitemporal radar

TABLE 12: Characterization of reference maize fields, Békés site.

Time period	Control		WCR damaged		Storm damaged		Total	
	#field	Area (ha)	#field	Area (ha)	#field	Area (ha)	#field	Area (ha)
6–8/8/2012	35	370	14	96	11	146	60	612
Total	35	370	14	96	11	146	60	612

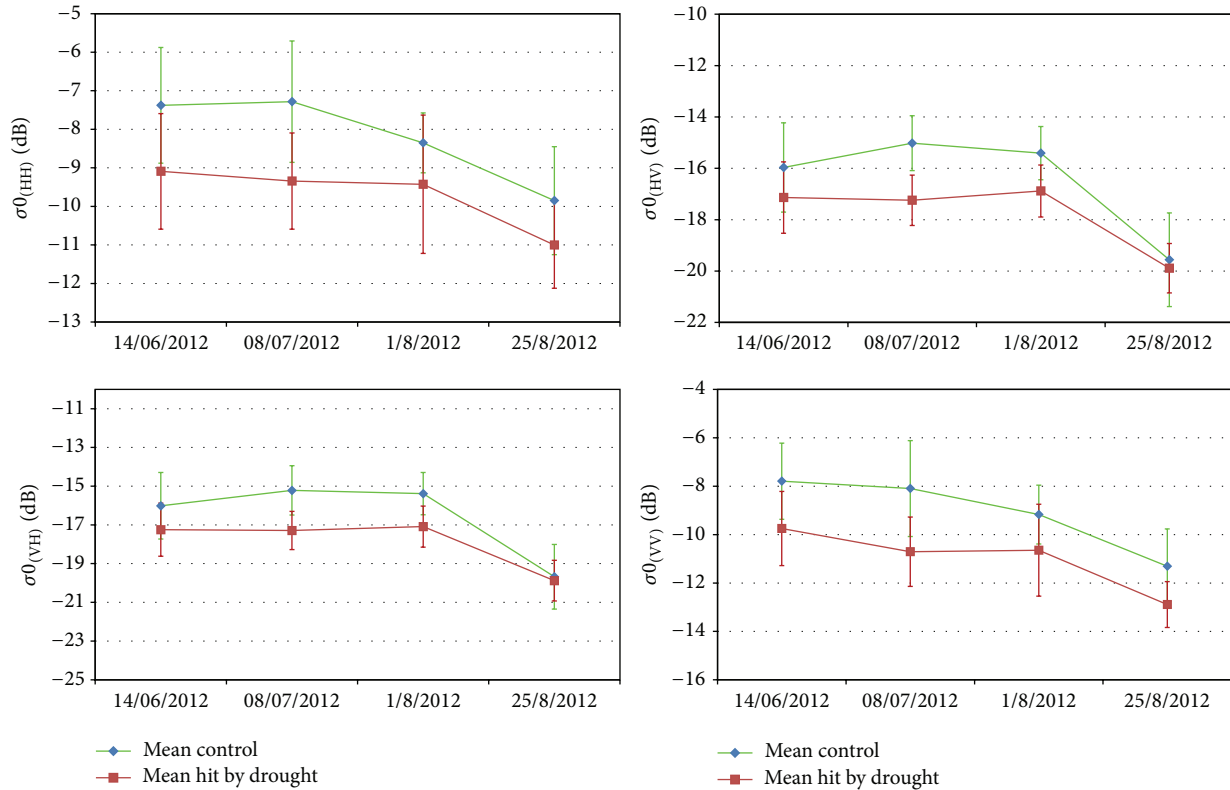


FIGURE 13: The temporal behavior of sigma0 bands of backscattered beam from sunflower (control and hit by drought area).

satellite data referred to as weed-free and weed-infected sunflower parcels. According to the graph, it is evidence that radar data acquired on 17/6/2012 is the most efficient in discrimination, while these two different statuses cannot be distinguished by analyzing radar data with other dates of acquisition about the area.

Hierarchy of polarimetric descriptors by their discrimination efficiency and level of significance is represented by Table 14. It is shown that components of Shannon entropy (SE , SE_i) ($P < 0.001$), odd and vol components of Yamaguchi decomposition ($0.001 < P < 0.01$), and eigenvalues of coherence matrix, l_2 in particular (on level $P < 0.001$), have significant role in discrimination of the two distinct statuses for mid-June. However we could not find such polarimetric descriptors applicable in order to distinguish parcels of these two statuses in mid-July and late August. In case of radar satellite scene acquired in early August anisotropy and p_2 descriptors ($0.01 < P < 0.05$) seemed to be significant in discrimination.

Based on evaluation of time series of both optical and radar satellite images it is evidence that weed infection in

sunflower can be detected most efficiently by synergistic evaluation of optical data acquired in middle of August and radar data acquired in mid-June. According to Figure 27 sunflower parcels having value of $NDVI > 35$ in middle of August and Shannon entropy < -1 in mid-June are expected to be infected.

We made weed maps in many different ways shown in Table 15. The overall accuracy of these maps is shown in the last column of Table 15. Figure 28 shows the map detailed in bold row of Table 15, and the accuracy of the map is almost 90%.

The accuracy of the processes was validated with reference data collection by field visit. The overall accuracy (%) and the Kappa value (%) [19] of different weed-infection maps are shown by Figure 29.

The accuracy of identification of weed-infected and weed-free areas was studied by averages of Hellden and Short measures [20], Figure 30.

3.3. WCR and Storm Damage in Maize Fields, Békés Site. The average temporal change of NDVI time series of healthy

TABLE 13: Ranking of polarimetric descriptors based on significance (t) calculated by Welch test, referred to as sunflower hit by drought and control fields, Csongrád site.

Sign. (t) and P value	Date of polarimetric descriptors			
	14/06/2012	08/07/2012	01/08/2012	25/08/2012
>3.8 <0.001	—	l3, l1, YAM _{vol} , SE, l2, SE _i	YAM _{vol}	YAM _{odd} , l1
2.9–3.8 0.001–0.01	—	YAM _{odd}	l2, l3	—
2.1–2.9 0.01–0.05	YAM _{odd} , l1, SE _i , ped, p3, rvi, polfrac, SE, SE _p , p1, l2, anilu	—	SE	SE, p1 anilu, SE _p

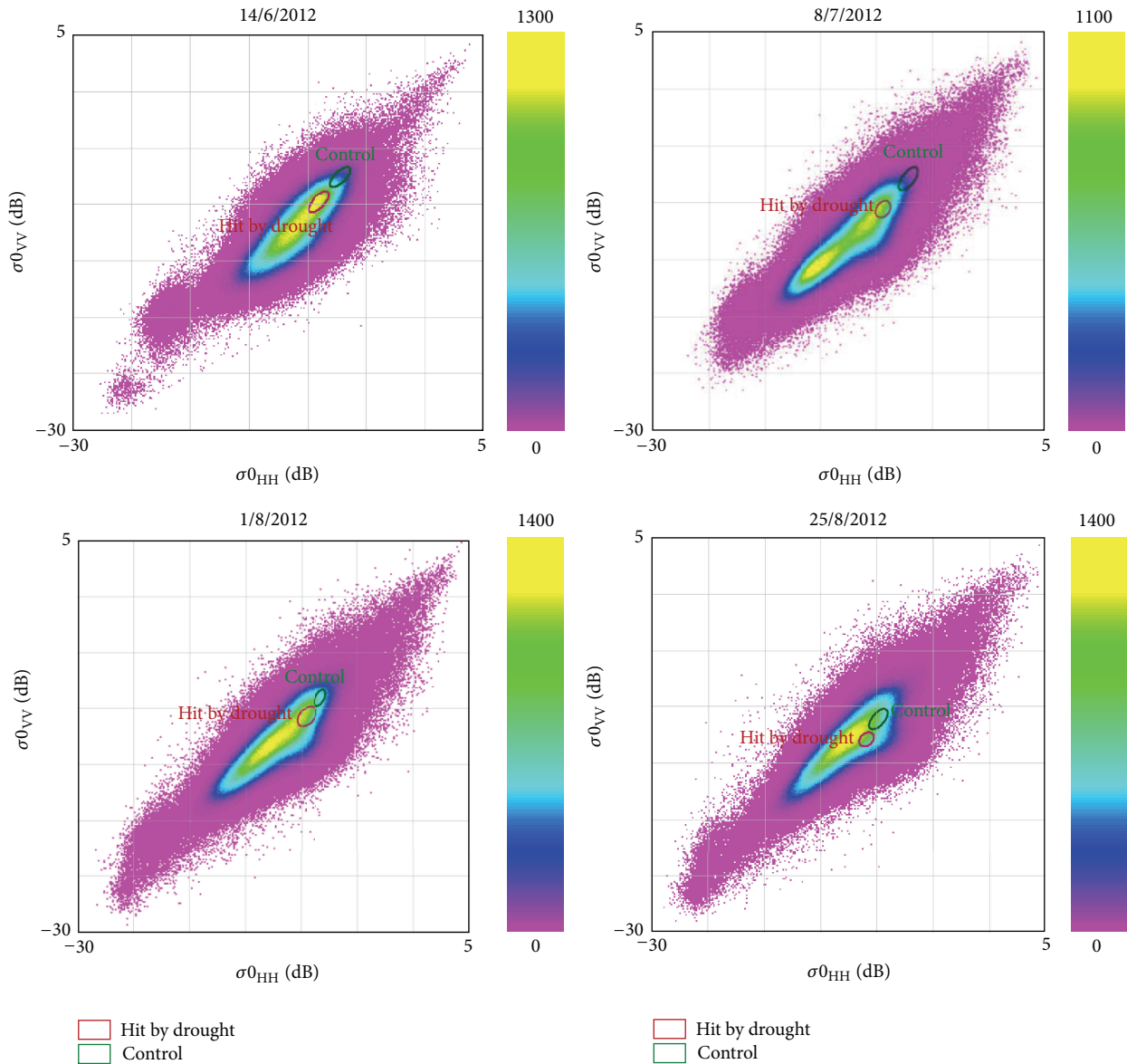


FIGURE 14: Separability of hit-drought and control areas in two-dimensional space of sigma0 co-pol. bands at different dates.

reference maize parcels to the ones damaged by Western Corn Rootworm and the storm which occurred on July 7 can be seen in Figure 31. Vertical lines represent standard deviation relevant to definite data. Figure 31 shows that no remarkable deviation among the three diverse states can be detected.

Deviation from the control parcels increases gradually during the period between July 10 and mid-August, particularly after the storm occurred. Therefore, maize parcels damaged by storm and Western Corn Rootworm can be separated from the control ones most efficiently by evaluation of optical

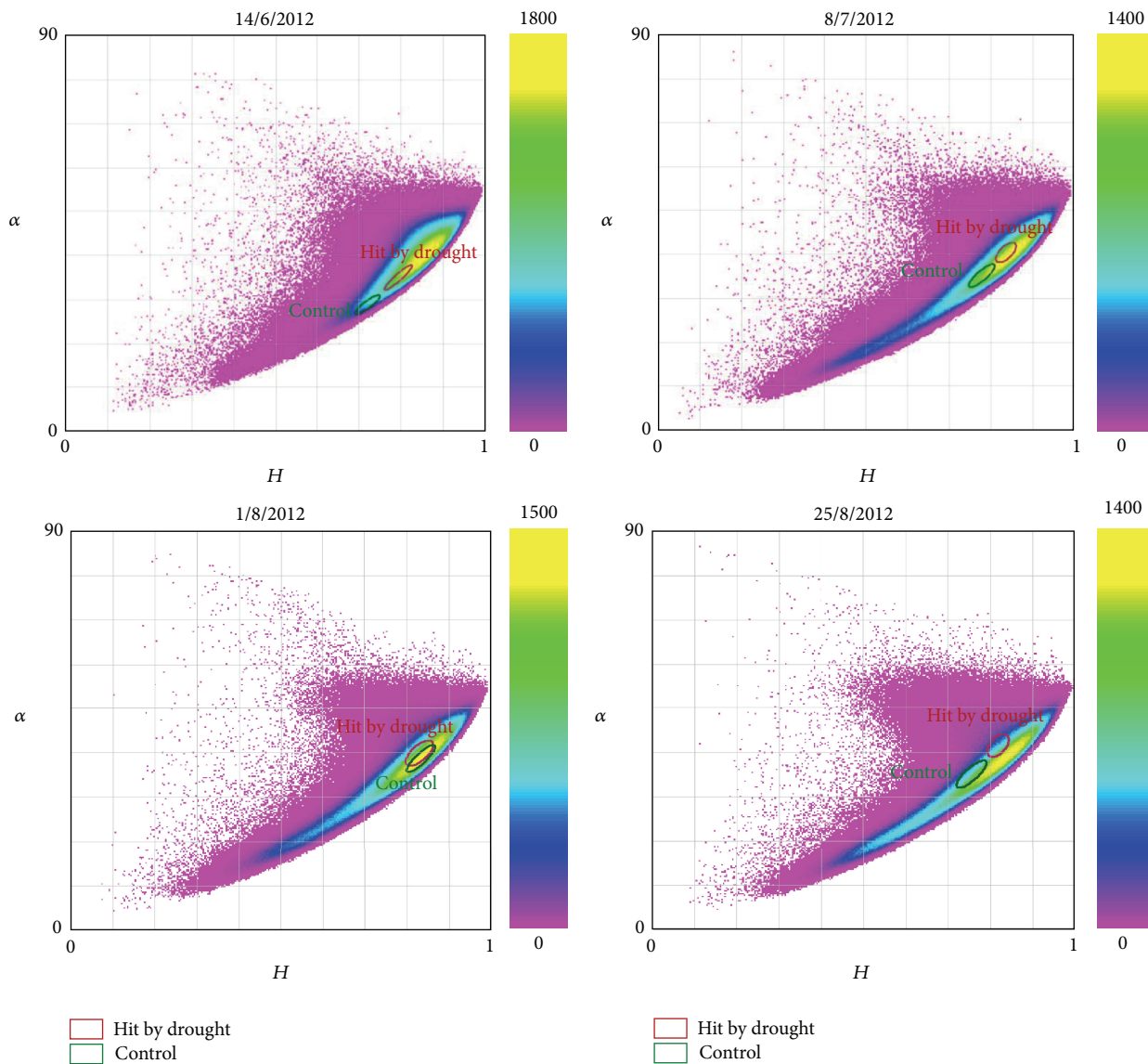


FIGURE 15: Separability of hit-drought and control areas in two-dimensional space of H-Alpha polarimetric descriptors at different dates.

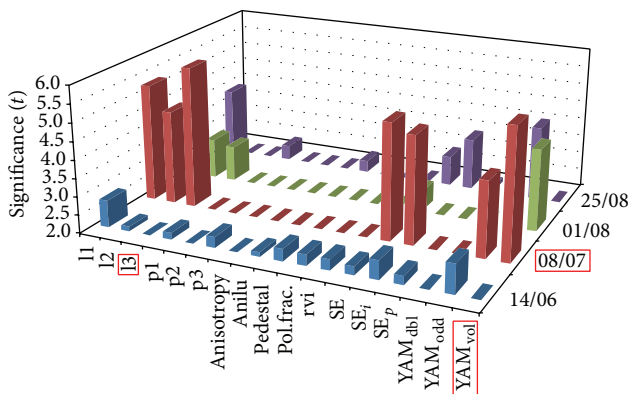


FIGURE 16: Result of separability analysis of sunflower hit by drought and control fields, Csongrád site.

TABLE 14: Ranking of polarimetric descriptors based on significance calculated by Welch test, weed-infected and weed-free sunflower fields, Baranya site.

Sign. and P value	17/06/2012	11/07/2012	04/08/2012	28/08/2012
>3.8	SE, l2 SE _i	—	—	—
<0.001	—	—	—	—
2.9–3.8	YAM _{vol} , YAM _{odd} l3, l1	—	—	—
0.001–0.01	—	—	—	—
2.1–2.9	SE _p	—	Anisotropy, p2	—
0.01–0.05	—	—	—	—

satellite data acquired between the end of July and mid-August.

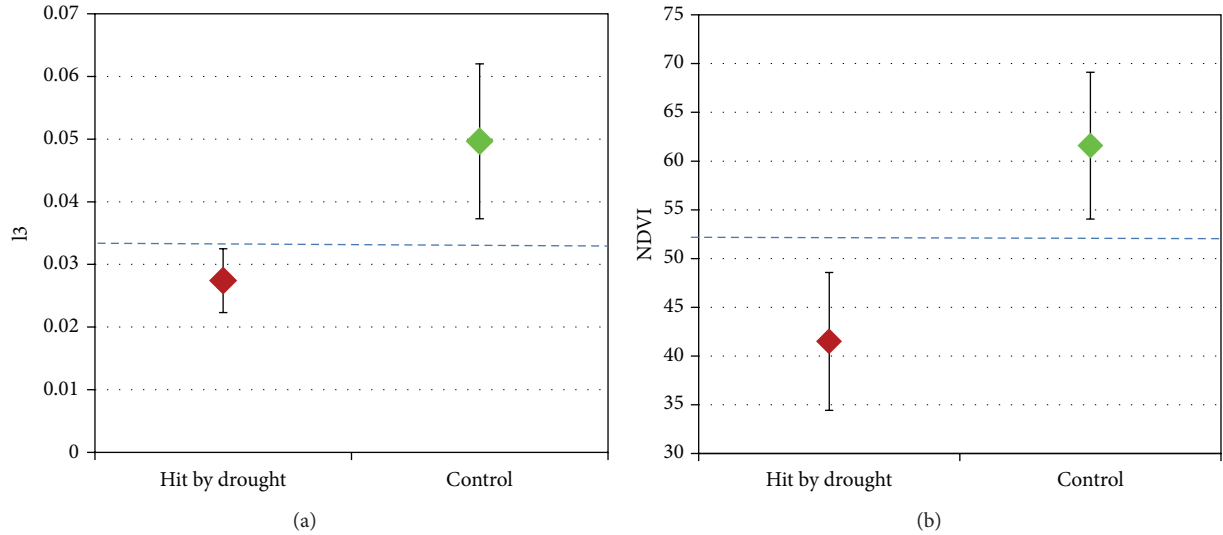


FIGURE 17: Average deviation of damaged (hit by drought) and healthy (control) reference parcels based on I3 derived from RADARSAT2 (08/07/2012), $P < 0.001$ (a). Average deviation of damaged (hit by drought) and healthy (control) reference sunflower fields based on NDVI derived from Landsat TM7 (04/07/2012), $P < 0.001$ (b). Vertical lines represent single standard deviation.

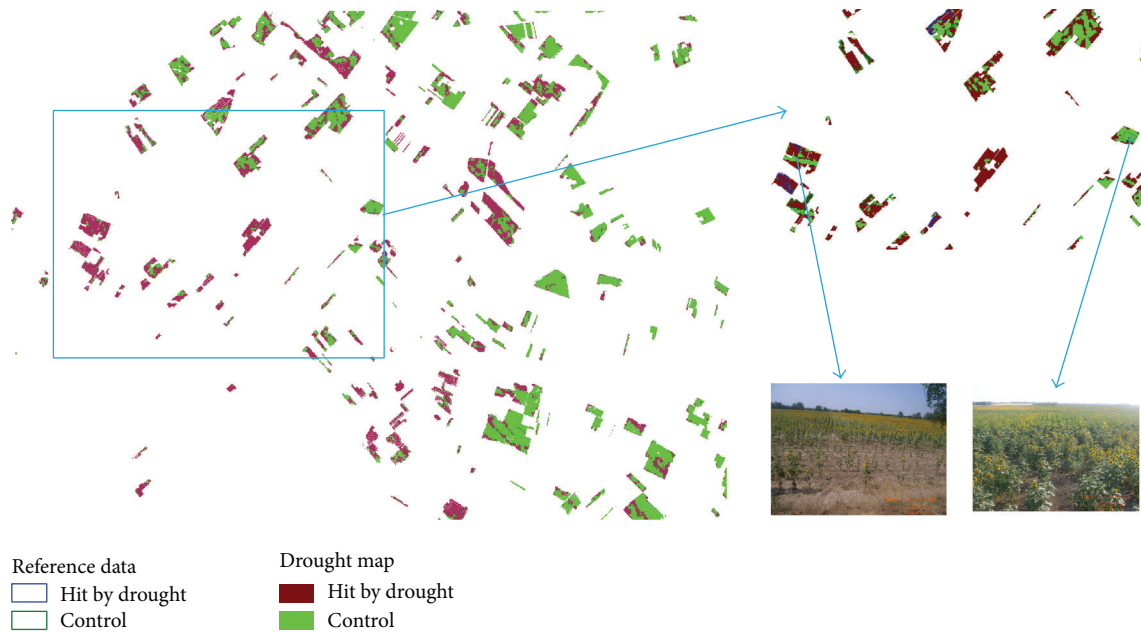


FIGURE 18: Drought map of sunflower parcels derived from integrated evaluation of Landsat TM7 (4/7/2012) and RADARSAT2 (8/7/2012) and the reference sunflower parcels.

Analogue can be observed in Figure 32 on which identification of the three different states can be followed by the help of NSI index derived from optical satellite data. Based on that the most efficient feature is the one derived from optical satellite image acquired in mid-August.

The mentioned three states of the maize parcels are represented in the two-dimensional space of co-pol bands of sigma0 (Figure 33).

Figure 34 represents result of separability analysis of polarimetric descriptors derived from multitemporal radar

satellite data referred to as maize parcels damaged by larvae of Western Corn Rootworm. According to Figure 34, radar data acquired on July 26, 2012 is proved to be more efficient in discrimination to the one acquired on August 19, 2012. Table 16 shows ranking of polarimetric descriptors based on discriminating efficiency of level of significance. It reveals that odd component of Yamaguchi decomposition and p component of Shannon entropy (SE_p) have the most important role in it (on significance level $0.001 < P < 0.01$). Although, in case of mid-August radar data there are

TABLE 15: Characterization of weed maps derived from radar and optical satellite data for sunflower parcels.

Basis of weed map	Type	#dates	Last date	Conditions for identification of weed infection	Overall (%)
RS2, 17/6/2012	Radar	1	17/6/2012	SE < -1	61.1
SPOT4, 28/7/2012	Optical	1	28/7/2012	NDVI > 60	72.8
LISS, 5/8/2012	Optical	1	5/8/2012	NDVI > 50	78.4
SPOT5, 20/8/2012	Optical	1	20/8/2012	NDVI > 35	83.0
SPOT4, 28/7/2012 + LISS, 5/8/2012	Optical	2	5/8/2012	NDVII > 60 and NDVI2 > 50	78.8
RS2_17/6/2012 + RS2_11/7/2012	Radar	2	11/7/2012	SE1 < -1 and SE2 < -1	78.9
RS2_17/6/2012 + RS2_11/7/2012 + SPOT4, 28/7/2012 + LISS, 5/8/2012	Radar + optical	2-2	5/8/2012	SE1 < -1 and SE2 < -1 and NDVII > 60 and NDVI2 > 50	89.7
RS2_17/6/2012 + SPOT4_28/7/2012	Radar + optical	1-1	28/7/2012	SE < -1 and NDVI > 60	83.9
RS2_17/6/2012 + LISS_5/8/2012	Radar + optical	1-1	5/8/2012	SE < -1 and NDVI > 50	86.7
RS2_17/6/2012 + SPOT5_20/8/2012	Radar + optical	1-1	20/8/2012	SE < -1 and NDVI > 35	91.3

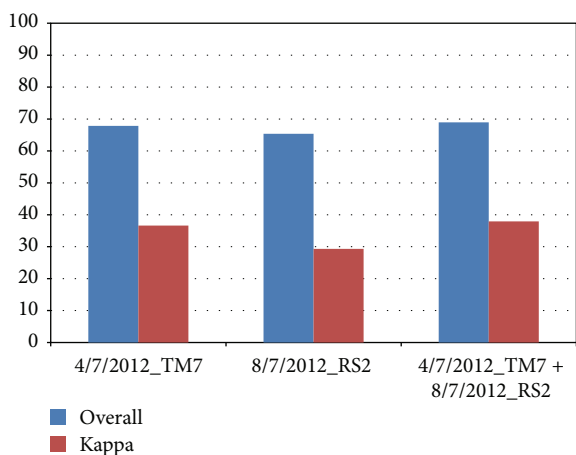


FIGURE 19: Result of accuracy assessment of sunflower's drought map.

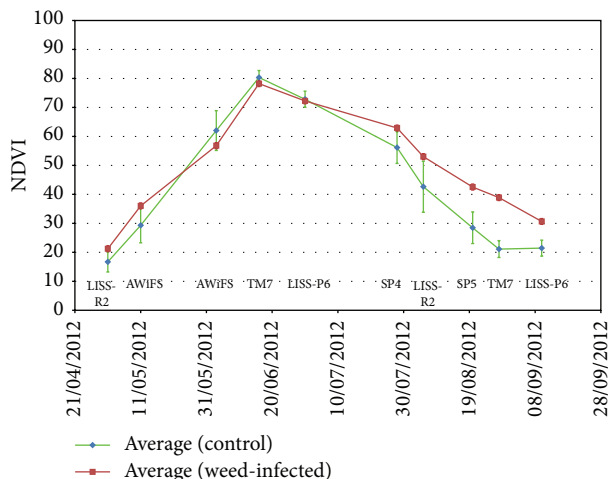


FIGURE 20: NDVI derived from optical satellite data for weed-infected and control sunflower fields, Baranya site. Vertical lines represent single standard deviation. LISS-R2: IRS-R2 LISS III, AWiFS: IRS-R2 AWiFS, TM7: Landsat TM7, LISS-P6: IRS-P6 LISS III, SP4: SPOT4, and SP5: SPOT5.

TABLE 16: Ranking of polarimetric descriptors based on significance calculated by Welch test, WCR damaged and control maize fields, Békés site.

Sign. and P value	Date of polarimetric descriptors	
	26/07/2012	19/08/2012
3-3.9 0.001-0.01	YAM _{odd} , SE _p	—
2.1-3 0.01-0.05	entropy praks, l1, depol.index, p1, SE _i , pedestal, anilu, SE	YAM _{dbl} , pol.frac., rvi, p3

TABLE 17: Ranking of polarimetric descriptors based on significance calculated by Welch test, storm damaged and control maize fields, Békés site.

Sign. and P value	Date of polarimetric descriptors	
	26/07/2012	19/08/2012
>3.9 <0.001	l1, SE _i	—
2.8-3.9 0.001-0.01	YAM _{odd} , SE, l2, SE _p	YAM _{dbl} , l2, SE, SE _i
2.1-2.8 0.01-0.05	Entropy praks, depol.index, p1, anilu, pedestal, pol.frac., rvi, p3	l3, l1

such polarimetric descriptors (YAM_{dbl}, pol.frac., rvi, and p3), suitable to separate different states significantly. However, this application is confined to significance level 0.01 < P < 0.05.

Figure 35 represents result of separability analysis of polarimetric descriptors derived from multitemporal radar satellite data referred to as maize parcels damaged by storm and control parcels. According to the figure, radar data acquired on July 26, 2012 is proved to be more efficient in discrimination compared to the one acquired on August 19, 2012. Table 17 shows ranking of polarimetric descriptors based on discriminating efficiency of level of significance. The table reveals that the first eigenvalue of coherence matrix (l1) and i component of Shannon entropy (SE_i) have the most

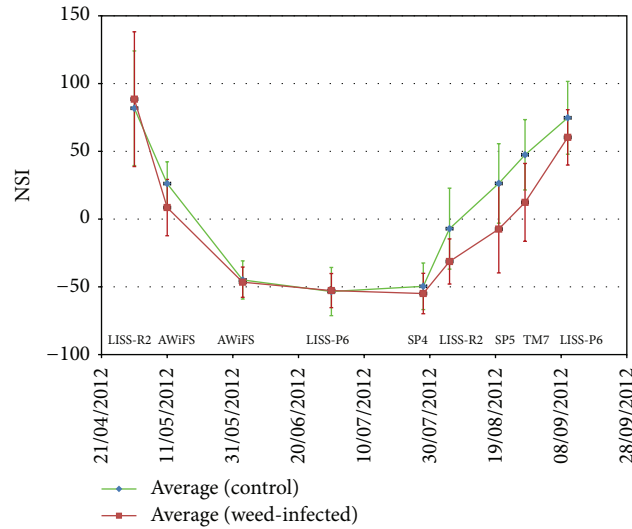


FIGURE 21: NSI derived from optical satellite data regarded to weed-infected and control sunflower fields, Baranya site. Vertical lines represent single standard deviation. LISS-R2: IRS-R2 LISS III, AWiFS: IRS-R2 AWiFS, TM7: Landsat TM7, LISS-P6: IRS-P6 LISS III, SP4: SPOT4, and SP5: SPOT5.

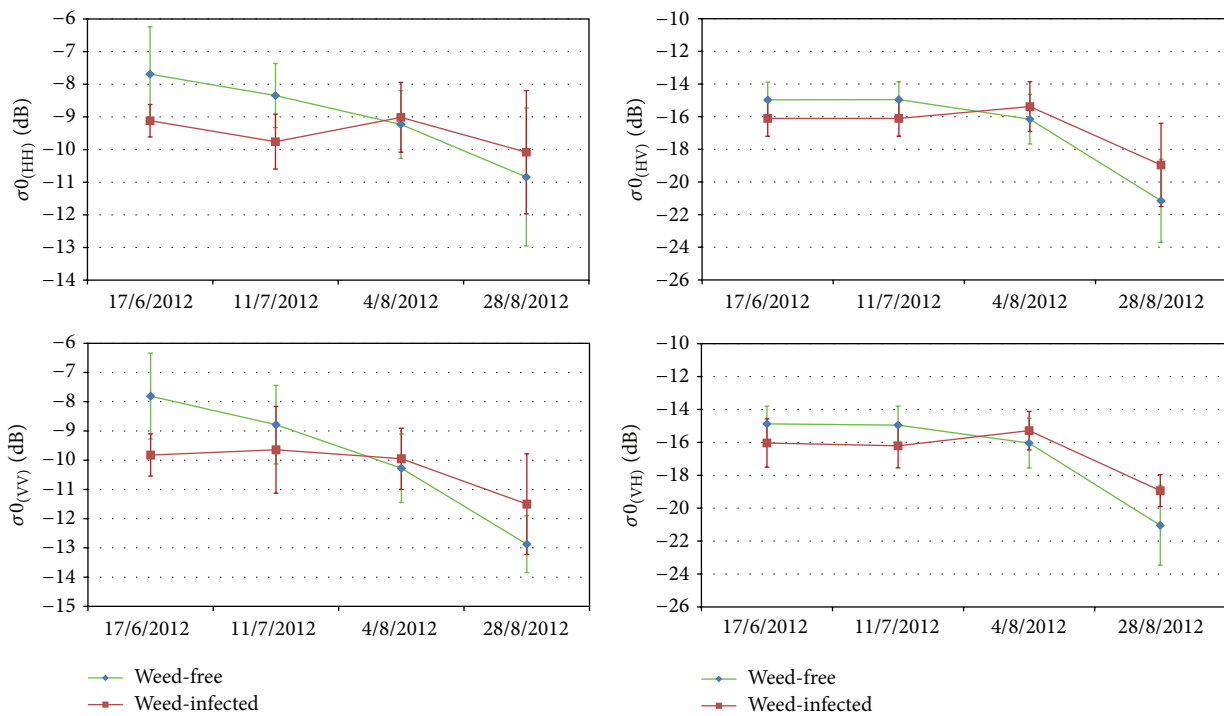


FIGURE 22: Temporal development of sigma0 values in different polarization bands, Baranya site.

important role (on $P < 0.001$ significance level). Although in case of radar data acquired in mid-August there are such polarimetric descriptors (YAM_{dbl} , $l2$, SE , and SE_i), suitable to separate these two different states significantly; however their application is confined to significance level $0.001 < P < 0.01$.

Figure 36 represents result of separability analysis of polarimetric descriptors derived from multitemporal radar satellite data referred to as maize parcels damaged by storm parallel to those damaged by larvae of Western Corn

Rootworm. According to the figure it is obvious that based on radar data acquired on July 26, 2012 these two different cases cannot be separated significantly. We were able to find a few polarimetric descriptors which were able to separate these cases from each other, although only restricted to significance level $0.01 < P < 0.005$. Table 18 shows ranking of polarimetric descriptors based on discriminating efficiency level of significance referred to as certain dates of acquisition. The table reveals that there exist such polarimetric descriptors

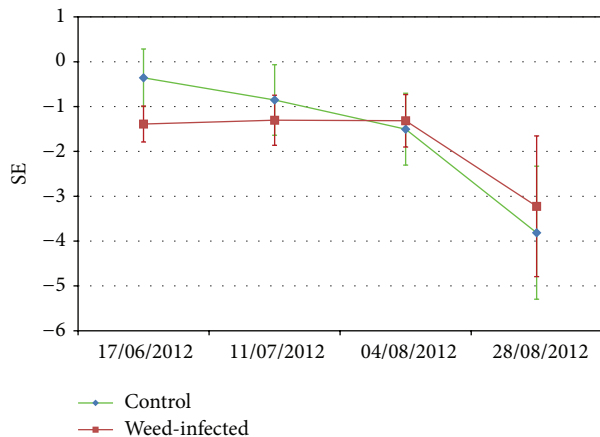


FIGURE 23: Temporal development of SE polarimetric descriptor, Baranya site.

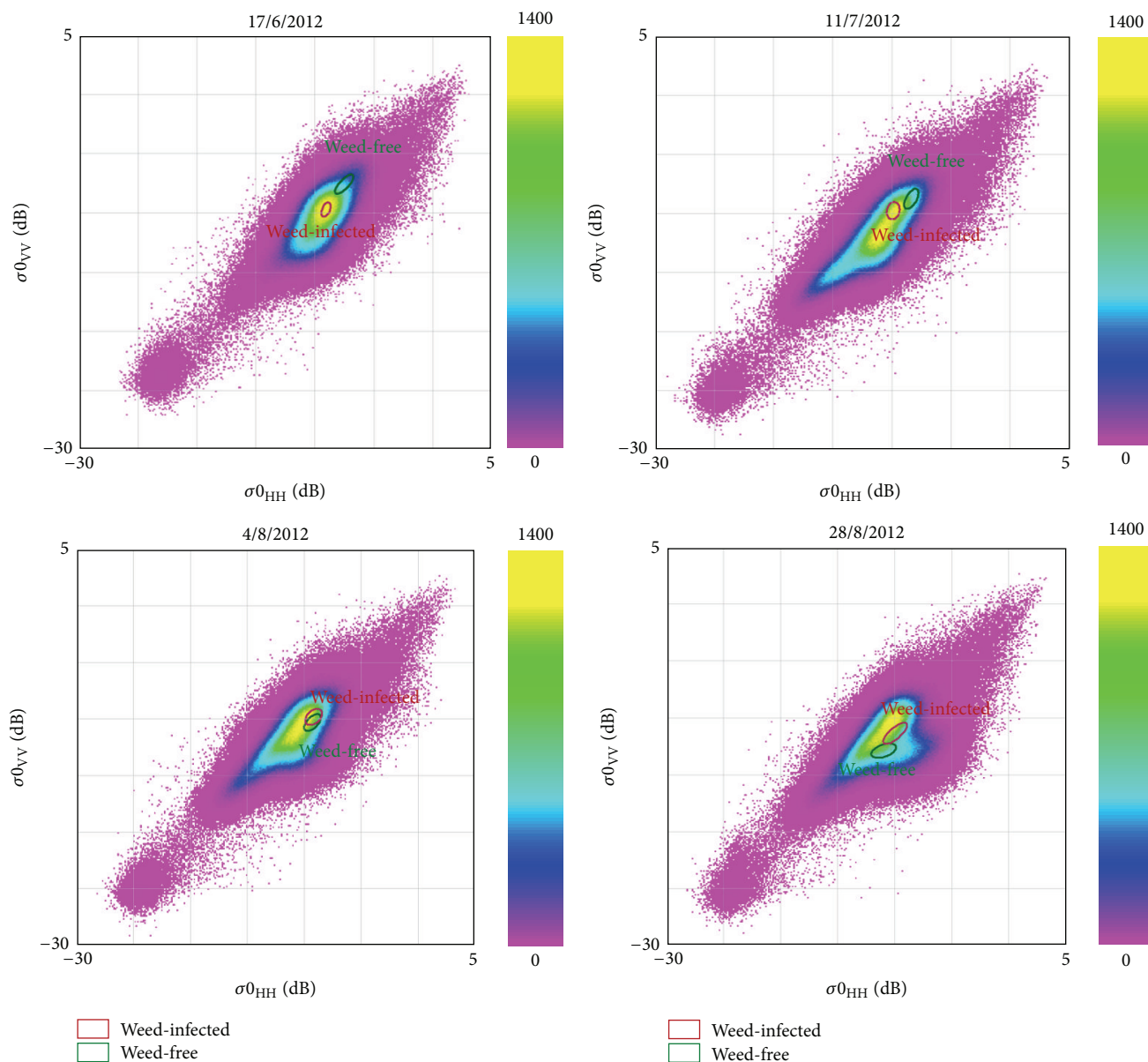


FIGURE 24: Separability of weed-infected and weed-free areas in two-dimensional space of sigma0 co-pol. bands at different dates, Baranya site.

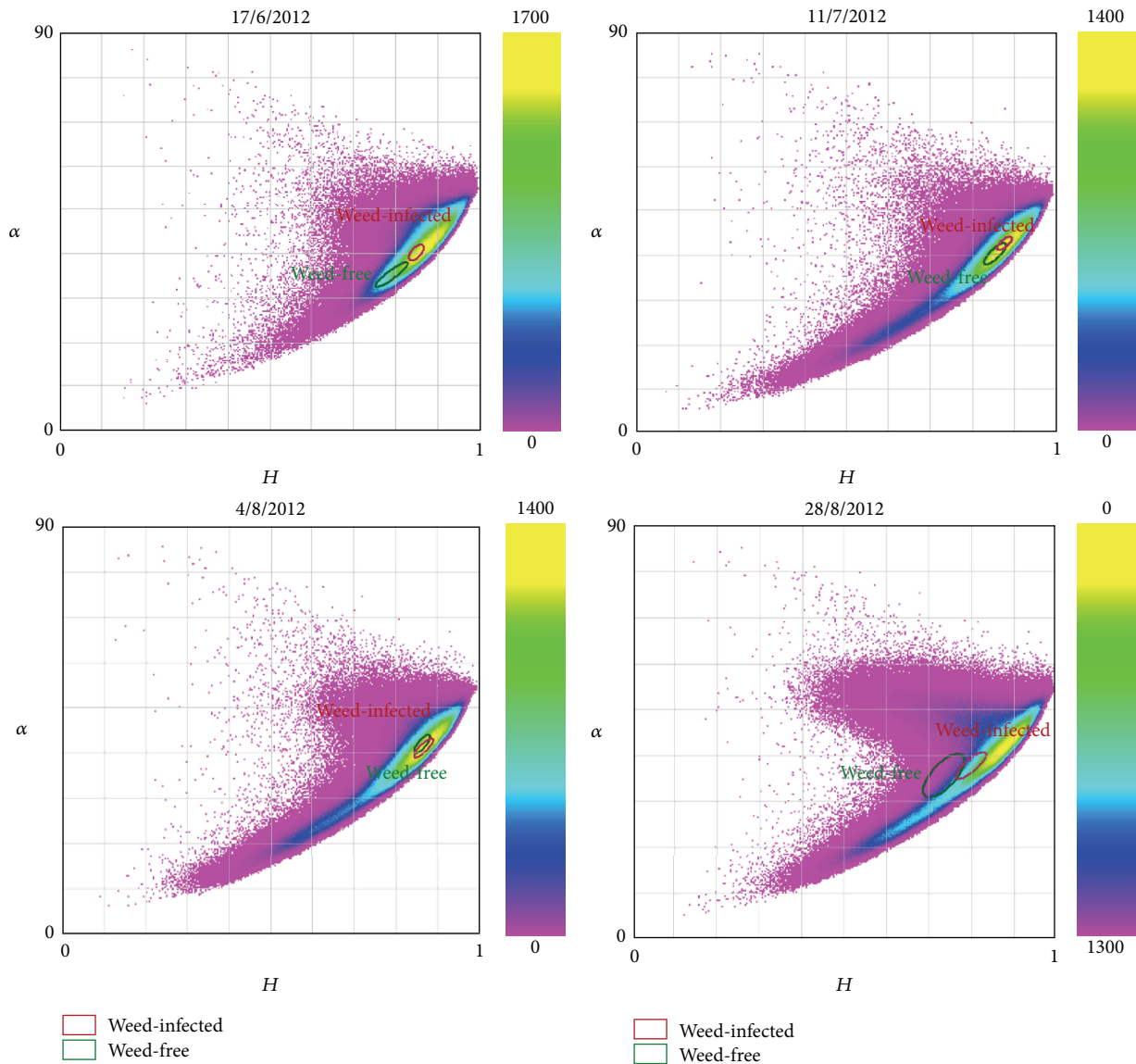


FIGURE 25: Separability of weed-infected and weed-free areas in two-dimensional space of H-Alpha polarimetric descriptors at different dates, Baranya site.

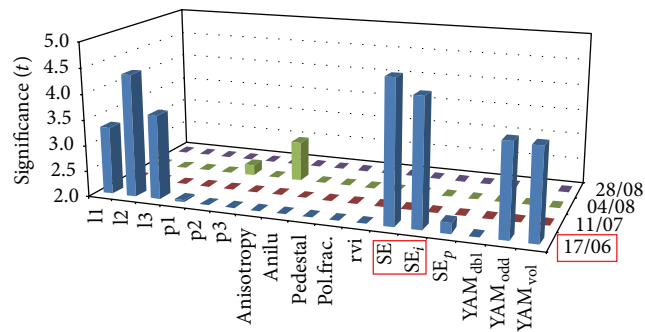


FIGURE 26: Result of separability analysis of discriminating weed-infected and weed-free sunflower fields, Baranya site.

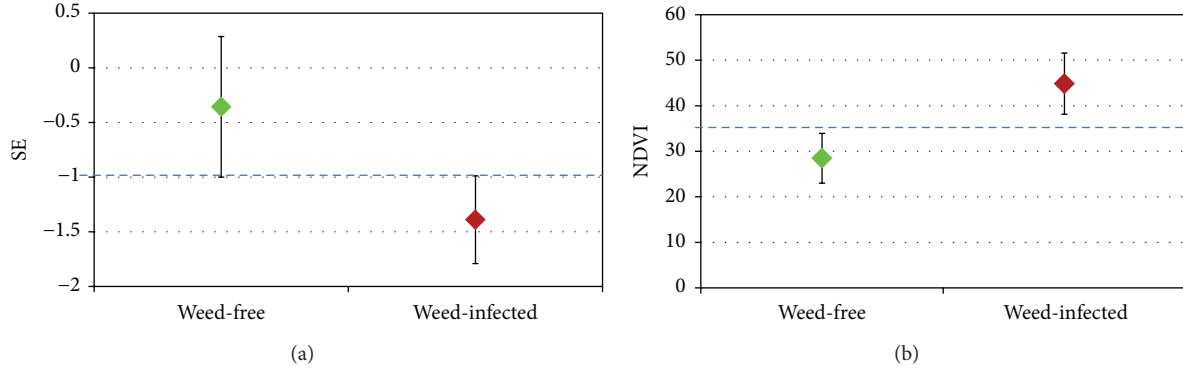


FIGURE 27: Average discrimination of weed-infected and weed-free reference sunflower fields based on SE derived from RADARSAT2 (17/06/2012), $P < 0.001$ (a). Average discrimination of weed-infected and weed-free reference sunflower fields based on NDVI derived from SPOT5 (20/08/2012), $P < 0.001$ (b). Vertical lines represent single standard deviation.

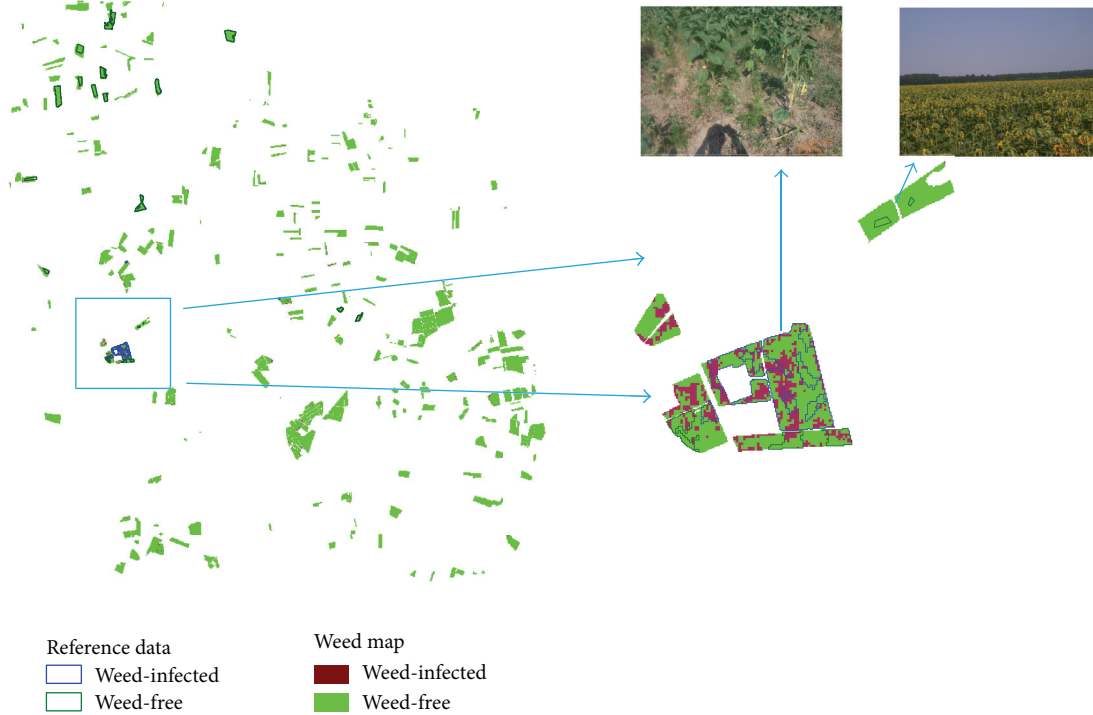


FIGURE 28: Weed infection map of sunflower parcels, created from optical and radar images.

(l3, l2, SE, and YAM_{vol}), eligible to separate significantly these two kinds of conditions, although these can be applicable only restricted to significance level $0.01 < P < 0.05$. However, in case of radar satellite data acquired during the last decade of July, none of the polarimetric descriptors were able to separate these cases at least by significance level $P = 0.05$.

Based on evaluation of time series of optical and radar satellite data alike, it can be established that identification of maize damaged by larvae of Western Corn Rootworm can be the most efficient by synergistic evaluation of those optical and radar satellite data acquired around the end of July. Taking Figures 37(a) and 38(a) into consideration those maize parcels are likely to be damaged where $NDVI < 53$ derived

TABLE 18: Ranking of polarimetric descriptors based on significance calculated by Welch test, WCR and storm damaged maize fields, Békés site.

Sign. and P value	Date of polarimetric descriptors	
	26/07/2012	19/08/2012
2.1–2.8 0.01–0.05	—	l3, l2, SE, YAM_{vol}

from IRS-P6 LISS III (08/08/2012) and $YAM_{odd} > -7.7$ derived from RADARSAT2 (26/07/2012). Similarly, maize parcels damaged by storm to healthy control parcels can be

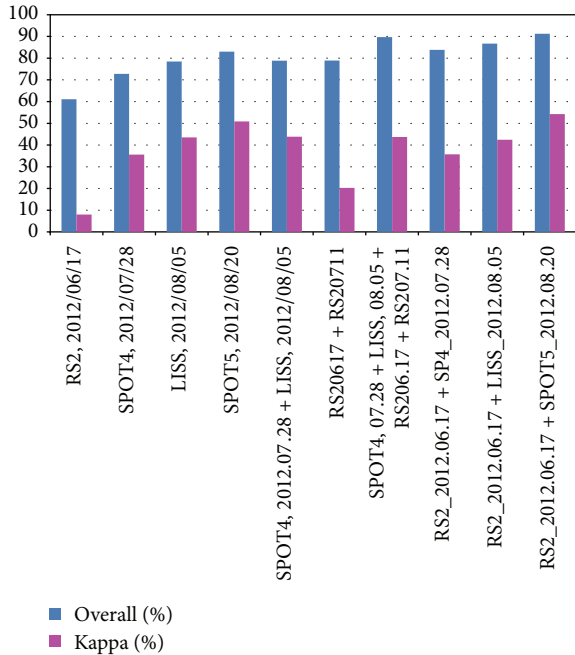


FIGURE 29: Result of general accuracy assessment of weed maps of sunflower parcels.

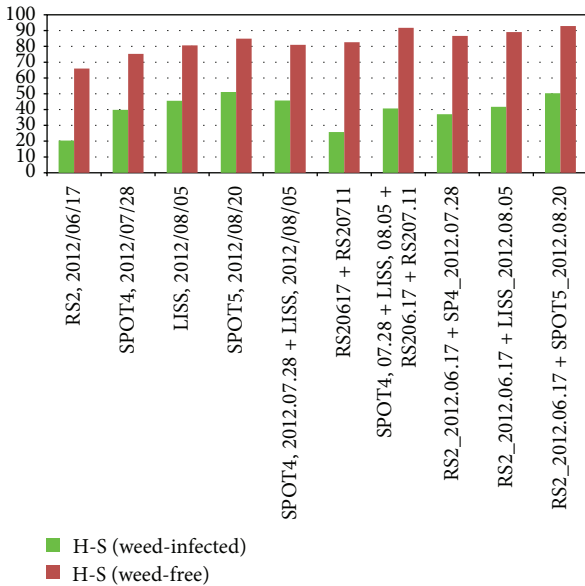


FIGURE 30: Result of accuracy assessment of the categories of weed maps indicated by average of measures defined by Hellden and Short.

separated most efficiently based on synergistic evaluation of optical and radar satellite data acquired between the end of July and mid-August. Based on Figures 37(b) and 38(b) those maize parcels are the most likely to be damaged by storm where $NSI < -3$ derived from SPOT5 (19/08/2012) and $l1 > 0.24$ derived from RADARSAT2 (26/07/2012).

Based on Figures 37(c) and 38(b) differently damaged corn fields can be separated by NSI index derived from

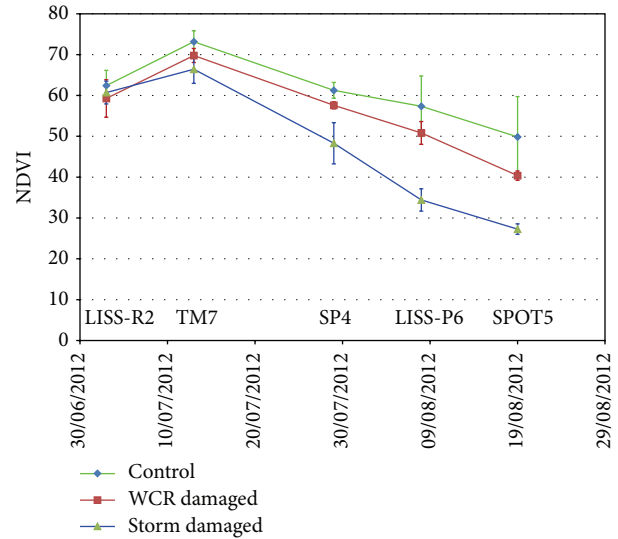


FIGURE 31: NDVI derived from optical satellite data for WCR and storm damaged and control maize fields, Békés site. Vertical lines represent single standard deviation. LISS-R2: IRS-R2LISS III, TM7: Landsat TM7, LISS-P6: IRS-P6 LISS III, SP4: SPOT4, and SP5: SPOT5.

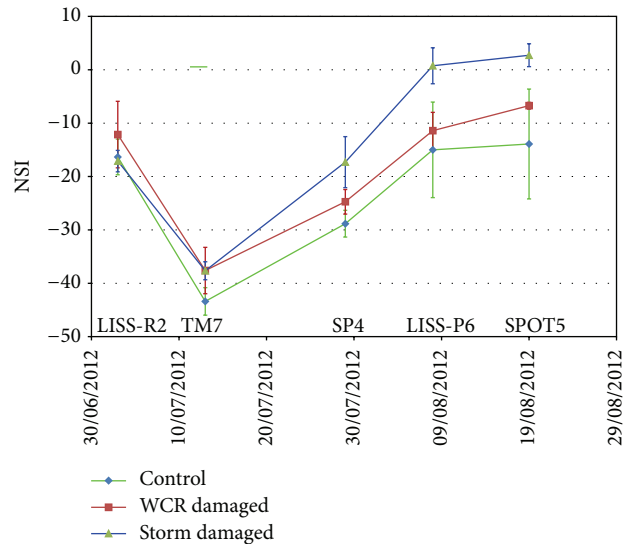


FIGURE 32: NSI derived from optical satellite data for WCR and storm damaged and control maize fields, Békés site. Vertical lines represent single standard deviation. LISS-R2: IRS-R2LISS III, TM7: Landsat TM7, LISS-P6: IRS-P6 LISS III, SP4: SPOT4, and SP5: SPOT5.

SPOT5 (19/08/2012) and $l3$ value derived from RADARSAT2 (19/08/2012) data. In case $NSI > -3$ and $l3 < 0.022$, damage by storm is more likely, while in $NSI < -3$ or $l3 > 0.022$ maize field is damaged by Western Corn Rootworm otherwise.

The identification of damaged maize parcels was carried out by coevaluating the odd component of Yamaguchi decomposition derived from the RADARSAT2 (26/7/2012) and the NDVI calculated from the IRS-P6 LISS III (8/8/2012). The separation of the two damaged states was made by

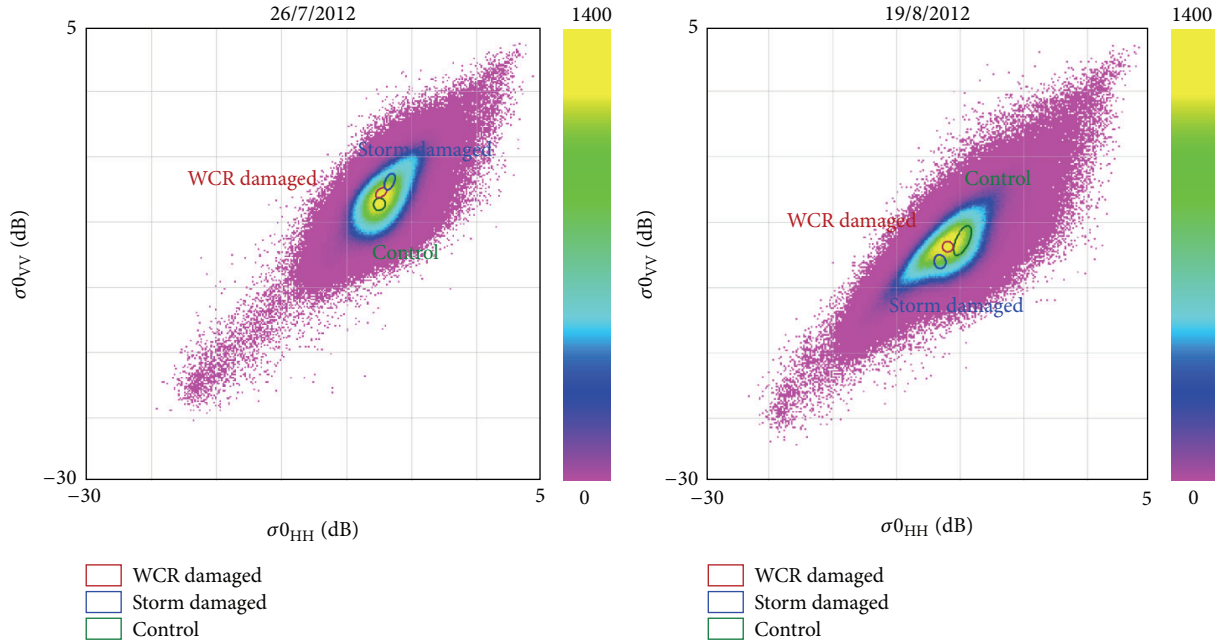


FIGURE 33: The ellipse positions of three states of the maize parcels in the co-pol. bands sigma0 space at different date.

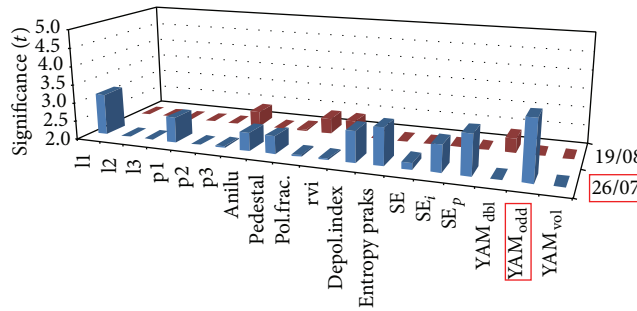


FIGURE 34: Result of separability analysis of WCR damaged and control fields, Békés site.

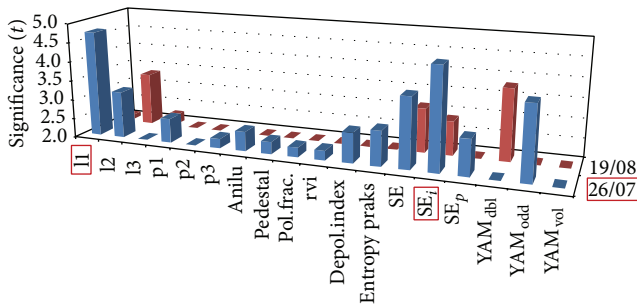


FIGURE 35: Result of separability analysis of discriminating storm damaged and control maize fields, Békés site.

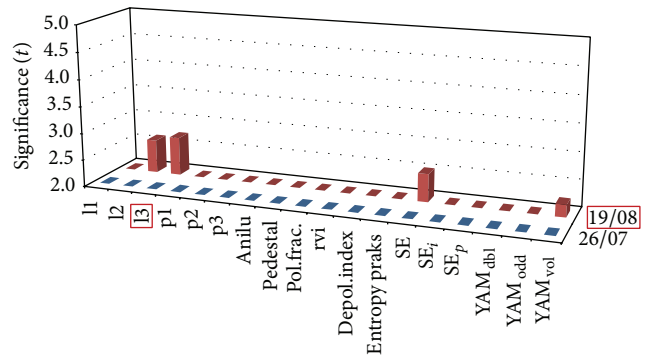


FIGURE 36: Result of separability analysis of storm and WCR damaged maize fields, Békés site.

the coevaluation of l3 derived from RADARSAT2 (19/8/2012) and NSI derived from SPOT5 (19/8/2012). The created damaged map is shown in Figure 39.

The damage map was compared to the reference data from field visit; we found the overall accuracy is about 75%.

4. Conclusions

In most cases, damage in croplands does not induce any notable spectral changes; therefore, they cannot be traceable

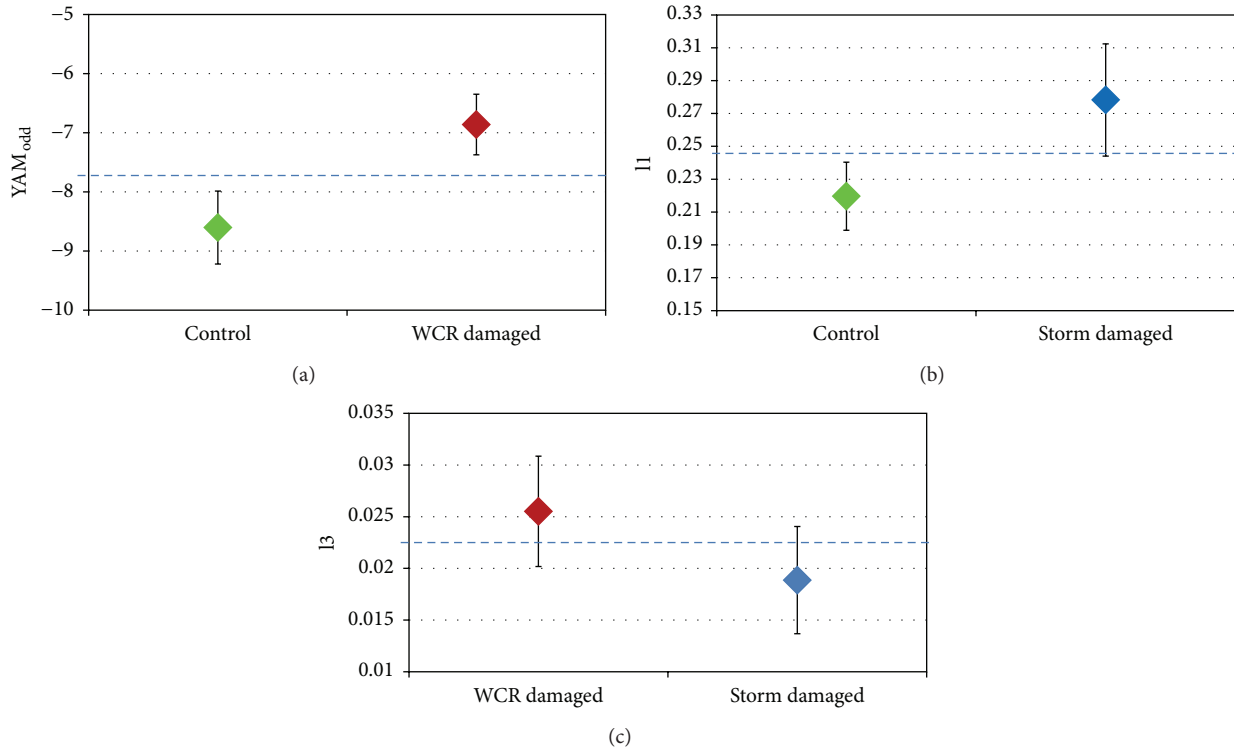


FIGURE 37: Average discrimination of WCR damaged and control reference maize fields based on YAM_{odd} derived from RADARSAT2 (26/07/2012), $P < 0.001$ (a). Average discrimination of storm damaged and control reference maize fields based on $I1$ derived from RADARSAT2 (26/07/2012), $P < 0.001$ (b). Average discrimination of WCR and storm damaged reference maize fields based on $I3$ derived from RADARSAT2 (19/08/2012), $0.01 < P < 0.05$ (c). Vertical lines represent single standard deviation.

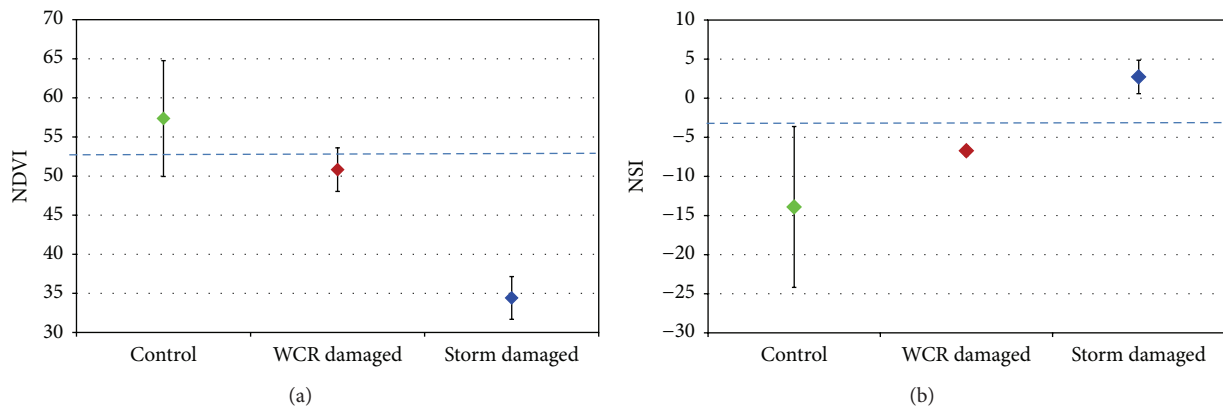


FIGURE 38: Average discrimination of WCR, storm damaged and control reference maize fields based on NDVI derived from IRS-P6 LISS III (08/08/2012), $P < 0.001$ (a). Average discrimination of WCR, storm damaged and control reference maize fields based on NSI derived from SPOT5 (19/08/2012), $P < 0.001$ (b). Vertical lines represent single standard deviation.

in optical range. However, polarimetric radar observation is applicable to identify changes in case they are accompanied by structural alterations. It is detectable that, in case of WCR and storm damage in corn, drought or weed infection in sunflower can be identified by polarimetric radar satellite images. We determined the most suitable polarimetric descriptors for characterising the abovementioned types of damage and their optimal time periods.

Synergistic application of radar and optical satellite data brings significant improvement in accuracy of identification of detecting damage accompanied by geometrical structure changes of vegetation. The most important output of our study is to emphasize the importance and to select those polarimetric descriptors which fit most of all the task given. For this express purpose a statistical method has already been developed. Importance of the method lies in the numbers of

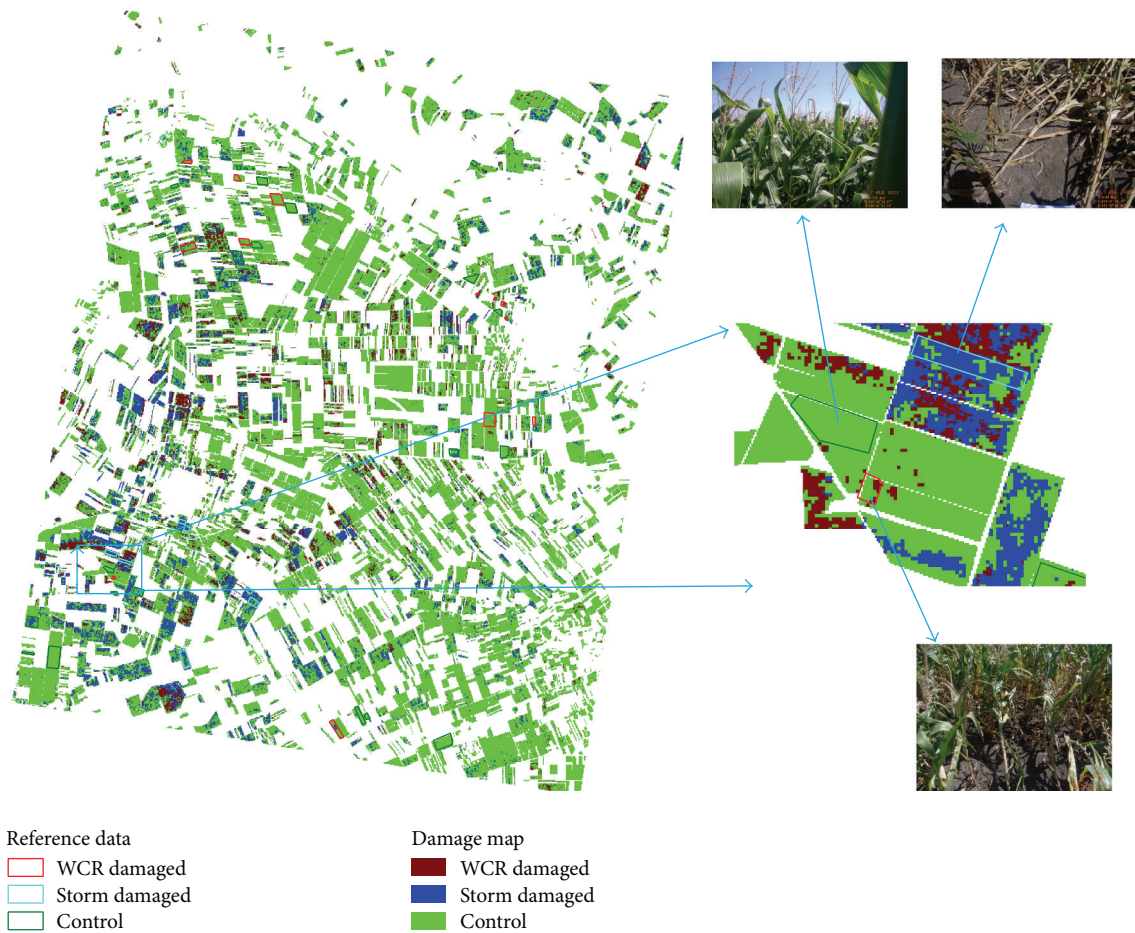


FIGURE 39: Damage map of maize parcels derived from integrated evaluation of radar and optical images.

polarimetric descriptors; it is difficult to find the most suitable one for the situation. An additional considerable output is that temporal development of changes both spectrally and geometrically differs. Therefore, better result requires usage of time series of radar and optical images as well.

Conflict of Interests

The authors declare that there is no conflict of interests regarding the publication of this paper.

Acknowledgments

Satellite image acquisition was carried out within the frame of our accepted SOAR-EU (called by ESA) proposal (EU-6741) entitled “Identification of structural changes in agriculture by radar polarimetry.” The study was sponsored by Research, Technology and Innovation Foundation of Hungarian Development Agency in the frame of URKUT_10-1-2011-0038 project entitled “Methodology development for synergistic usage of optical and radar satellite images focusing on agricultural damages.”

References

- [1] J. W. Cable, J. M. Kovacs, X. Jiao, and J. Shang, “Agricultural monitoring in Northeastern Ontario, Canada, using multi-temporal polarimetric RADARSAT-2 Data,” *Remote Sensing*, vol. 6, no. 3, pp. 2343–2371, 2014.
- [2] H. McNairn, J. J. van der Sanden, R. J. Brown, and J. Ellis, “The potential of RADARSAT-2 for crop mapping and assessing crop condition,” in *Proceedings of the 2nd International Conference on Geospatial Information in Agriculture and Forestry*, Lake Buena Vista, Fla, USA, January 2000.
- [3] C. Titin-Schnaider, “ONERA-Palaiseau (2000): radar polarimetry for vegetation observation,” in *Proceedings of the CEOS SAR Workshop*, ESA SP-450, Toulouse, France, October 1999.
- [4] P. Ferrazzoli, L. Guerriero, and G. Schiavon, “Experimental and model investigation on radar classification capability,” *IEEE Transactions on Geoscience and Remote Sensing*, vol. 37, no. 2, pp. 960–968, 1999.
- [5] S. R. Cloude and E. Pottier, “An entropy based classification scheme for land applications of polarimetric SAR,” *IEEE Transactions on Geoscience and Remote Sensing*, vol. 35, no. 1, pp. 68–78, 1997.
- [6] J. M. Lopez-Sanchez, F. Vicente, J. D. Ballester-Berman, and S. R. Cloude, “Polarimetric response of rice fields at C-band: analysis and applications,” in *Proceedings of the 6th International*

Workshop on Science and Applications of SAR Polarimetry and Polarimetric Interferometry (POLinSAR '13), vol. SP-71, ESA, Frascati, Italy, January-February 2013.

- [7] Z. Qi, A. G. Yeh, X. Li, and Z. Lin, "Land use and land cover classification using RADARSAT-2 polarimetric SAR image," in *Proceedings of the 7th ISPRS TC Symposium—100 Years ISPRS*, W. Wagner and B. Székely, Eds., vol. 38, part 7A, IAPRS, Vienna, Austria, July 2010.
- [8] G. Nádor, G. Surek, D. Fényes et al., "Identification of structural changes caused by weed infection in agriculture by optical and radar data," in *Proceedings of the 5th ESA-ESRIN*, Frascati, Italy, January 2011.
- [9] G. Surek, G. Nádor, D. Fényes, and L. Vasas, "Monitoring of western corn rootworm damage in maize fields by using integrated radar (ALOS PALSAR) and optical (IRS LISS, AWiFS) satellite data," *Geocarto International*, vol. 28, no. 1, pp. 63–79, 2013.
- [10] G. Surek, G. Nádor, D. Á. Gera, I. Hubik, R. K. Anikó, and C. Török, "Identification of geometrical structural changes in agriculture by optical and radar data, poster presentation," in *Proceedings of the 6th International Workshop on Science and Applications of SAR Polarimetry and Polarimetric Interferometry (POLinSAR '13)*, Frascati, Italy, January-February 2013.
- [11] C. López-Martínez, L. Ferro-Famil, and E. Pottier, PolSARpro v4.0 Polarimetry Tutorial, 2005, <http://earth.eo.esa.int/polsarpro/tutorial.html>.
- [12] J.-S. Lee and E. Pottier, *Polarimetric Radar Imaging from Basics to Applications*, CRC Press, Taylor & Francis Group, 2009.
- [13] P. Réfrégier and J. Morio, "Shannon entropy of partially polarized and partially coherent light with Gaussian fluctuations," *Journal of the Optical Society of America A: Optics and Image Science, and Vision*, vol. 23, no. 12, pp. 3036–3044, 2006.
- [14] Y. W. Goodman, "Coherence of optical waves," in *Statistical Optics*, pp. 157–236, Wiley, 1985.
- [15] Y. Yamaguchi, J. Nakamura, K. Aoyama, and H. Yamada, "Coherent decomposition of fully polarimetric radar data," in *Proceedings of the IEEE International Geoscience and Remote Sensing Symposium (IGARSS 2008)*, vol. 4, pp. 161–164, IEEE, Boston, Mass, USA, July 2008.
- [16] Y. Yamaguchi, A. Sato, W.-M. Boerner, R. Sato, and H. Yamada, "Four-component scattering power decomposition with rotation of coherency matrix," *IEEE Transactions on Geoscience and Remote Sensing*, vol. 49, no. 6, pp. 2251–2258, 2011.
- [17] Y. Yamaguchi, Y. Yajima, and H. Yamada, "A four-component decomposition of POLSAR images based on the coherency matrix," *IEEE Geoscience and Remote Sensing Letters*, vol. 3, no. 3, pp. 292–296, 2006.
- [18] B. L. Welch, "The generalization of 'Student's' problem when several different population variances are involved," *Biometrika*, vol. 34, no. 1-2, pp. 28–35, 1947.
- [19] R. G. Congalton and R. G. Oderwald, "Assessing landsat classification accuracy using discrete multivariate analysis statistical techniques," *Photogrammetric Engineering and Remote Sensing*, vol. 49, no. 12, pp. 1671–1678, 1983.
- [20] G. H. Rosenfield and K. Fitzpatrick-Lins, "A coefficient of agreement as a measure of thematic classification accuracy," *Photogrammetric Engineering & Remote Sensing*, vol. 52, no. 2, pp. 223–227, 1986.